ABSTRACT

Title of Dissertation:	SYNTHESIS AND POLYMER-MEDIATED REGIOSELECTIVE SELF-ASSEMBLY OF SHAPED PLASMONIC NANOPARTICLES
	Xiaoying Lin, Doctor of Philosophy, 2021
Dissertation directed by:	Professor John T. Fourkas, Department of Chemistry and Biochemistry Professor Zhihong Nie, Fudan University

Plasmonic nanoparticles with collective excitations of the conduction-band electrons have many potential applications in surface-enhanced spectroscopies, photocatalysis, photovoltaics, and biomedicine. The plasmonic properties are highly tunable via the size, shape, chemical composition, and surrounding media of individual nanoparticles, as well as by the interactions with other nanoparticles in close proximity. Fabricating plasmonic nanostructures with precisely controlled size, shape, and interparticle distance is critical for harnessing desirable properties. Although top-down lithographic techniques are widely used for fabricating shaped plasmonic nanoparticles and ensembles, the products are limited to 2D planar structures and the cost can be prohibitive. As low-cost and versatile alternatives, colloidal synthesis and self-assembly have been explored to fabricate complex plasmonic nanostructures.

In this dissertation, wet-chemistry synthetic and self-assembly approaches are explored for fabricating well-defined plasmonic nanostructures with high structural

complexity. Chapter 2 describes a facile synthetic method for circular and triangular gold nanorings with tunable diameters, ring thicknesses, surface roughness, and hence the plasmonic response. The gold nanorings with rough surface show 100-fold higher enhancement factor than solid gold nanoparticles as substrate for surface-enhanced Raman spectroscopy. In chapter 3, we demonstrate regioselective bonding between nanospheres and nanoplates originating from the steric hindrance of polymeric ligand brushes and the anisotropy of nanoparticles. The regioselectivity enables a self-assembly system with precise control over the relative orientation of Au nanospheres on Ag nanoplates and the stoichiometry of reactive groups of copolymeric ligands dictates the number of nanoparticles in one nanocluster. The yield of each assembly was ~70% without further purification. Optical study reveals that different bonding modes affect the plasmonic coupling of assembled structures. In chapter 4, the regioselective bonding is applied to fabricate complex plasmonic nanocluster, nanoflowers and nanobuds, with distinct bonding modes. Compared with nanobuds, nanoflowers with the same number of petals show stronger electric field enhancement and further localized surface plasmon resonance peak shifts.

The synthetic and self-assembly methods demonstrated in this dissertation have great potentials and versatility in designing not only plasmonic nanoclusters, but also other inorganic nanoparticle-based functional structures with high complexity.

SYNTHESIS AND POLYMER-MEDIATED REGIOSELECTIVE SELF-ASSEMBLY OF SHAPED PLASMONIC NANOPARTICLES

by

Xiaoying Lin

Dissertation submitted to the Faculty of the Graduate School of the
University of Maryland, College Park, in partial fulfillment
of the requirements for the degree of
Doctor of Philosophy
2021

Advisory Committee:
Professor John T. Fourkas, Chair
Professor Zhihong Nie (Fudan University)
Professor Sang Bok Lee
Professor Efrain Rodriguez
Professor Mohamad Al-Sheikhly, Dean's Representative

Acknowledgements

I would like to thank my advisors, Dr. John T. Fourkas and Dr. Zhihong Nie, for their outstanding guidance throughout my PhD study. Thank you to Dr. Nie for leading me into and guiding me through my PhD research with interesting projects and brilliant ideas. It has been such good experience that past years just seem too short. Thank you to Dr. Fourkas for mentoring me with patience and kindness, especially during my preparation for this dissertation. It would be hard for me to finish without his constructive suggestions and efficient revisions.

I am grateful to my dissertation committee members, Dr. Sang Bok Lee, Dr. Efrain Rodriguez, and Dr. Mohamad Al-Sheikhly for your valuable time and suggestions. In my first semester as a graduate student, I had a short interview with Dr. Sang Bok Lee where he shared some helpful tips that I still benefit from in my everyday research. I took Advanced Inorganic Chemistry with Dr. Rodriguez and Polymer Physics with Dr. Al-Sheikhly in the same semester, probably the busiest but happiest one. I learnt a lot from their great lectures and instructions, as well as their enthusiastic attitude towards science and research.

I am thankful to all my previous and current labmates. Dr. Yi Liu, Dr. Meihua Lin, Dr. Chuncai Kong, Dr. Shaoyi Zhang, and Dr. Chenglin Yi have helped me profoundly at the early stage of my research, without whom I cannot build up my projects easily. They are not just good mentors and collaborators, but also great friends in life. My biggest thanks go to my current labmates, Qian Zhang, Kyle Webb, and Chelsey Lamar. We have done great jobs to keep it going together, and we will all make it to the end. I

am thankful to all the Fourkas group members for sharing the wonderful atmosphere in research and daily conversations, as well as kind attention and interest to my research.

I appreciate the chance to work with and get help from great people here in the University of Maryland. I am thankful to Dr. Andrei Vedernikov for his help and guidance, as the program director and course instructor, in my first-year study. Thanks to Dr. YuHuang Wang for insightful advises and permission on using the UV-vis-NIR spectrometer in his lab. I am grateful to Dr. Sz-Chian Liou from Nanocenter for teaching and assisting me with electron microscopes through the past five years. I would like to thank Diane Canter for handling my questions and paperwork.

My special thanks go to the Department of Chemistry and Biochemistry for supporting my study and funding my research under special circumstances. The department chair, Dr. Janice Reutt-Robey, and the directors of chemistry graduate program, Dr. Efrain Rodriguez and Dr. Amy Mullin, are the guardian angels for graduate students. I feel secure and not on edge in our department with supportive environment despite of the pandemic era and uncertainties in policy for international students in the past year.

Finally, I would like to thank my former advisor and mentor in my undergraduate study, Dr. Hao Zhang and Dr. Xue Zhang, respectively. It is because of their excellent mentorship that I decided to pursue a PhD degree and a career in chemistry. I am not sure where my next step goes, but I will always remember where and how I started.

Table of Contents

List of Tables

List of Figures

List of Abbreviations

2D	Two dimensional
3D	Three dimensional
4-MBA	4-mercaptobenzoic acid
AA	Acrylic acid
AgNPs	Silver nanoplates
AIBN	Azobis(isobutyronitrile)
AuNCs	Gold nanocubes
AuNRs	Gold nanorings
AuNSs	Gold nanospheres
BCPs	Block copolymers
CPPA	4-cyano-4-(phenylcarbonothioylthio) pentanoic acid
CTAB	Hexadecyltrimethylammonium bromide
DEG	Diethyleneglycol
DMAEMA	N,N-dimethylaminoethyl methacrylate
DMF	N,N-Dimethylformamide
DMSO	Dimethyl sulfoxide
DNA	Deoxyribonucleic acid
EDX	Energy-dispersive X-ray spectroscopy
EF	Enhancemnet factor
FDTD	Finite-difference time-domain
FEG	Field emission gun
GPC	Gel Permeation Chromatography

$HAuCl_4$	Gold (III) chloride trihydrate
HyA	Hydrochloride hydroxylamine
LSPR	Localized surface plasmon resonance
NCs	Nanocubes
NIR	Near-infrared
NPs	Nanoparticles
NRs	Nanorings
NSs	Nanospheres
PEO	Poly(ethylene oxide)
PS	Polystyrene
PVP	Poly(vinylpyrrolidone)
RAFT	Reversible addition-fragmentation chain transfer
SAM	Self-assembled monolayer
SEM	Scanning electron microscope
SERS	Surface-enhanced Raman scattering
TEM	Transmission electron microscope
THF	Tetrahydrofuran
TGA	Thermogravimetric Analysis
TSC	Trisodium citrate
UV	Ultraviolet
vis	Visible

Chapter 1: Introduction

Overview: Plasmonic nanoparticles with collective excitations of the conduction-band electrons have many potential applications in surface-enhanced spectroscopies, photocatalysis, photovoltaics, and biomedicine. The plasmonic properties are highly tunable via the size, shape, chemical composition, and surrounding media of individual nanoparticles, and also by interactions with other nanoparticles in close proximity. This chapter briefly reviews how these factors determine or affect the optical properties of plasmonic nanoparticles and their ensembles, and then discusses applications for and current fabrication techniques of assemblies of plasmonic nanoparticles.

1.1 Plasmonic nanoparticles and localized surface plasmon resonance

Plasmonic nanoparticles are typically conductive nanoparticles that exhibit strong interactions with light at a particular frequency due to the collective excitations of the conduction-band electrons.[1-3] When a bulk metal is excited by light, the induced charges can propagate as an electromagnetic wave along the metal's surface. For nanoscale metal particles, however, the oscillating charges are strongly confined and so the electric field is enhanced on the surface of a nanoparticle, in a phenomenon known as localized surface plasmon resonance (LSPR). The LSPR of metallic nanoparticles can generate remarkably enhanced electric fields near the nanoparticles and leads to strong extinction at the resonant frequency. The wavelength and strength

of LSPR can be tuned by the size, shape, chemical composition, and surrounding medium of individual nanoparticles.[4-10]

1.1.1 Chemical composition

The LSPR frequency (ω_{LSPR}) of nanoparticles is highly dependent on the plasmon frequency (ω_p) of the corresponding bulk material, which is a function of the free electron density (n_e) of the material:[4,10]

$$\omega_{LSPR} \approx \sqrt{\frac{\frac{n_e e^2}{\epsilon_0 m}}{1+2\epsilon_m}} = \frac{\omega_p}{\sqrt{1+2\epsilon_m}}\ , \qquad (1.1)$$

where n_e is the number density of electrons, e is the electronic charge, m is the effective mass of the electron, and ϵ_0 and ϵ_m are the permittivity of free space and of the surrounding medium, respectively.

As the most common plasmonic metals, noble metals (gold, silver, and copper) have free-electron densities in the range of 10^{22} to 10^{23} cm^{-3}, with corresponding LSPRs in the visible region.[11] Plasmon resonances are not limited to metals, and occur in conducting metal oxides[12] as well as in semiconductors with appreciable free carrier densities.[13,14] For doped semiconductors, a typical value of n_e is in the range of 10^{16} to 10^{21} cm^{-3}, leading to plasmon wavelengths in the microwave and infrared regions.[14]

Ag has been widely considered as an optimal plasmonic material that has the lowest optical loss in the visible and NIR spectral ranges.[15] However, Ag nanomaterials suffer from easy oxidation and poor stability. Au is another popular plasmonic material, with excellent performance in the visible and NIR spectral ranges, and superior chemical stability under ambient conditions. As Ag and Au are relatively expensive,

Cu and Al have become alternative choices. However, Cu and Al both suffer from chemical instability, restricting their further applications under atmospheric environments. Alloyed metals have also been broadly considered for plasmonic applications. The alloying of different noble metals can be used to tune the LSPR frequency or wavelength of the resultant materials.[15,16] For example, $Au_xAg_{(1-x)}$ alloy nanoparticles with varying mole fractions show only one LSPR peak, and the LSPR band blueshifts linearly with increasing mole fractions of Ag.[16-18]

1.1.2 Size or particle volume

Mie theory[19] has been used to estimate variations in plasmonic response due to nanoparticle size, anisotropy, and other extrinsic parameters, independently from changes in the chemical composition. The dipolar plasmon response (oscillator strength) of the nanoparticle is often defined by its polarizability, which can be expressed by the electrostatic Clausius-Mossotti equation (also known as the Lorentz-Lorenz equation):[20]

$$\alpha = 4\pi\varepsilon_0 R^3 \left|\frac{\varepsilon - \varepsilon_m}{\varepsilon + 2\varepsilon_m}\right|, \tag{1.2}$$

where R is the radius of the nanoparticle, ε_0 and ε_m are the dielectric constants of vacuum and surrounding medium, respectively, and ε is the dielectric function of the material.

In the simplified case of a metal nanosphere with a radius R much smaller than the incident wavelength of light (the quasi-static approximation), the plasmon response is essentially dipolar in nature. The strength and frequency of this resonance are related to the total number of electrons in the oscillating dipole (defined by the particle volume,

which is proportional to R^3), the complex dielectric function, and the dielectric constant of the surrounding medium.[19,20]

In experimental observations, the extinction of plasmonic nanoparticles increases as the size of the particle increases.[7] Extinction includes both absorption and scattering components, which have different scaling relationships with the particle volume. The absorption cross section increases linearly with particle volume, whereas the scattering cross section is relatively smaller, but scales with the volume squared.[20]

1.1.3 Geometric morphology

Geometric morphology is another important factor determining the plasmonic properties of metallic nanoparticles as the dipolar plasmon resonance is highly sensitive to shape anisotropy.[8] Isolated spherical nanoparticles typically support a single resonance frequency, whereas anisotropic nanoparticles will exhibit at least one additional plasmon mode, as well as large redshifts in plasmon resonance.[8,15] **Figure 1.1** is a typical example showing the strong dependence of plasmonic properties on the morphologies of Ag nanoparticles of the same size. The extinction (black), absorption (red), and scattering (blue) spectra were calculated for Ag nanoparticles with different shapes (*i.e.,* sphere, cube, tetrahedron, and octahedron) and topologies (*i.e.,* solid, hollow, and core–shell).

The spectrum of an isotropic nanosphere (**Figure 1.1A**) exhibits a single resonance peak, whereas the spectra of anisotropic cubes (**Figure 1.1B**), tetrahedra (**Figure 1.1C**), and octahedra (**Figure 1.1D**) exhibit multiple, red-shifted resonance peaks. The resonance frequency of a nanosphere redshifts when it is made hollow (as a nanoshell of 10 nm thickness, **Figure 1.1E**), and redshifts further if the nanoshell is

made thinner (5 nm, **Figure 1.1F**). Surface polarization (*i.e.*, charge separation) is the most important factor in determining the frequency and intensity of plasmon resonance for a given metal, because it provides the main restoring force for electron oscillations.[21] Variations in particle size, shape, or dielectric environment will change the surface polarization and thus the resonance peak. The calculated spectra of a 40-nm cube (**Figure 1.1B**) exhibit more peaks than for a sphere because the cube has several distinct symmetries for dipole resonance, compared with only one for the sphere.[22] The most intense peak is red-shifted compared with that of the sphere, a common phenomenon observed for nanostructures with sharp corners.[23] Calculations of the near fields around nanostructures show that surface charges accumulate at sharp corners.[24] This segregation of charges into corners increases charge separation, and thereby reduces the restoring force for electron oscillation.[25] The weaker restoring force in turn manifests itself in a red-shift of the resonance peak.

Similar trends are observed for the tetrahedron (**Figure 1.1C**) and octahedron (**Figure 1.1D**) as well, although they have reduced scattering cross-sections because of their different symmetries and smaller particle volumes. The tetrahedron shows the most red-shifted resonance peaks among the three solid nanoparticles due to having the sharpest corners.

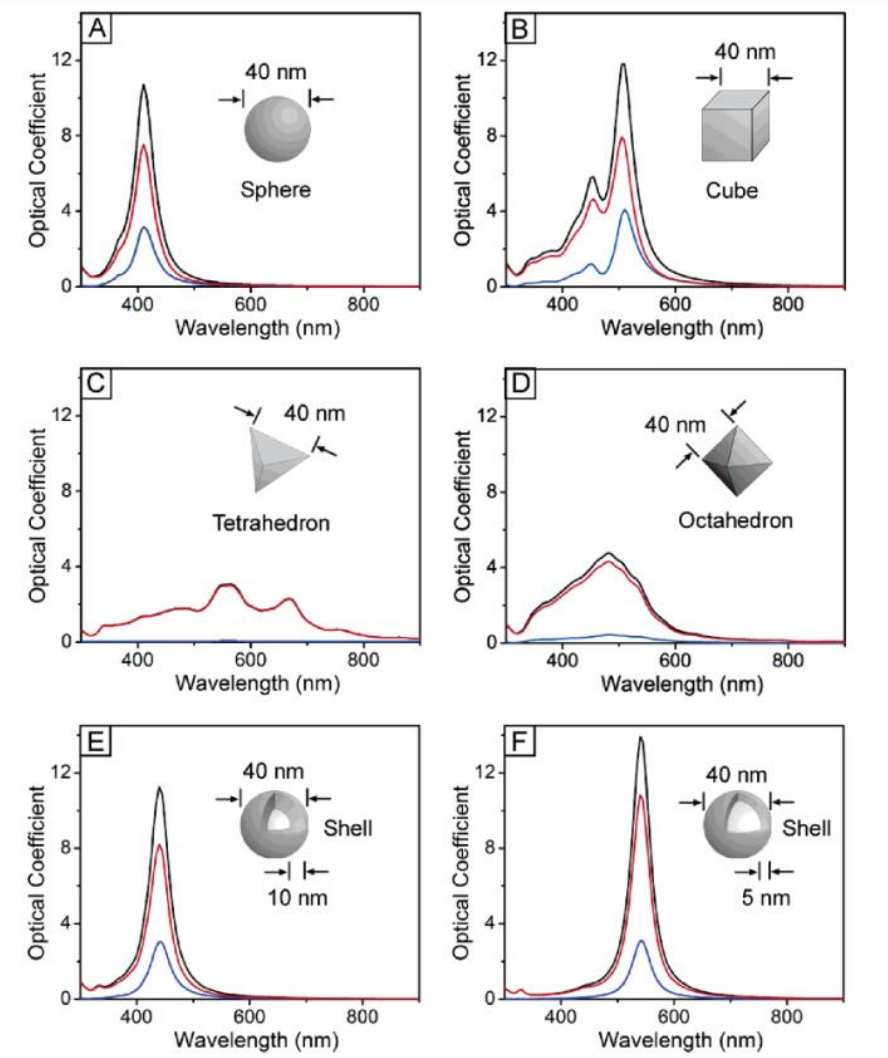

Figure 1.1 Calculated UV-vis extinction (black), absorption (red), and scattering (blue) spectra of silver nanostructures in shapes of (A) a sphere, (B) a cube, (C) a tetrahedron, (D) an octahedron, and (E, F) nanoshells with different shell thickness. Adapted from Ref. 8.

1.1.4 Surrounding medium

As indicated by **equations 1.1** and **1.2**, the surrounding medium also modulates the plasmonic properties of nanoparticles. In experimental observations, polymer-stabilized Au particles dispersed in organic solvents of varying refractive indices (n =

1.33-1.60) demonstrated a shift in absorption from red to purple (520 to 545 nm), accompanied by an increase in extinction intensity.[26] These observations are in excellent agreement with Mie theory, based on the changes in dielectric constant of the medium.

Surface ligands can also influence the optical properties of metal nanoparticles by changing the mobility of conduction-band electrons. Strongly adsorbing anions and surfactants, such as thiols, accelerate plasmon relaxation, resulting in peak broadening. This effect has been attributed to a reduction in conduction-band electron mobility, due to electronic coupling between the plasmon and charge-transfer bands formed by the metal-adsorbate complex.[27]

1.2 Plasmon Coupling in nanoensembles

An important property of plasmonic nanoparticles is the dependence on interparticle interactions,[28-33] which is the basis for engineering plasmonic nanostructures. When plasmonic nanoparticles are within a few nanometers of each other, plasmon coupling occurs because of the interacting resonances of the excited plasmons. This phenomenon enables the hybridization of the initial plasmon bands, leading to a peak shift and near-field enhancement. For example, the plasmon coupling between two identical nanospheres along the interparticle axis will create hybridized modes, and a new longitudinal LSPR appears in the longer wavelength region (redshifted), compared to the wavelengths of the single nanospheres. The LSPR redshifts further as the interaction between nanoparticles becomes stronger with a decreasing interparticle distance.[34-38] The strength of the plasmon coupling can be measured by the extent of the shifts, and is dependent on the interparticle gaps, filling

materials, as well as the plasmonic resonances supported by individual nanoparticles.[39-41] However, the interparticle gaps are not only defined by the interparticle distance between coupled nanoparticles. Other factors, including the gap area, gap facets, and gap curvature also define the nanogaps, and potentially influence the plasmon coupling, especially for ensembles of anisotropic nanoparticles.[42-48] Kim *et al.*[48] prepared nanogaps with subtle differences in nanogap morphology by attaching a gold nanosphere (AuNS) to the face, edge, or vertex of a gold nanocube (AuNC), as presented in **Figure 1.2a**. The experimental results (**Figure 1.2b**) and simulations (**Figure 1.2c**) indicate that plasmon coupling along the interparticle axis between AuNSs and AuNCs lowers in energy as the AuNS adsorbs on increasingly curved locations on the AuNC, with the highest energy on the face, followed by the edge, and the lowest energy at the vertex.

The effect of nanoparticle shape anisotropy and assembly orientation on plasmon coupling has also been studied in assemblies of Au nanorods.[49,50] Whereas the end-to-end assembly of Au nanorods results in a red shift of the longitudinal SPR band,[51] side-by-side assembly, in strong contrast, shows a blue shift of the longitudinal plasmon band.[49] The dependence of the plasmonic shift on assembly orientation has been explained by Jain *et al.*[49] on the basis of "selection rules" for plasmon coupling.

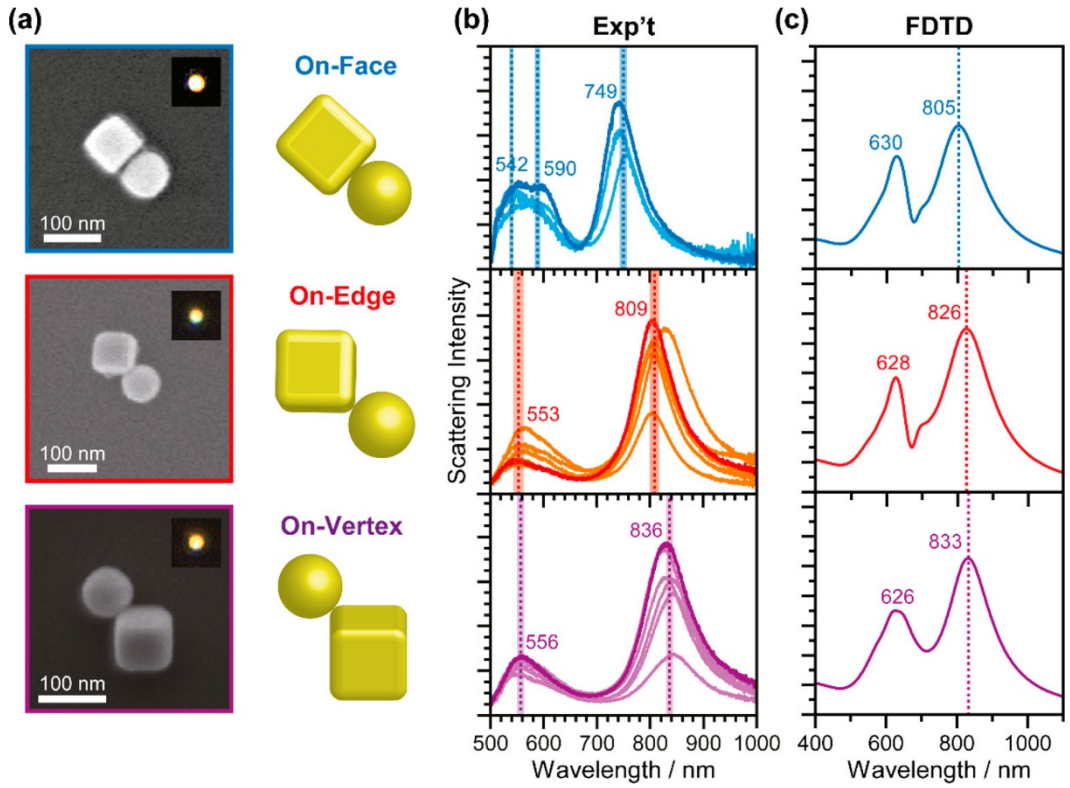

Figure 1.2 Plasmon coupling of AuNS−AuNC dimers according to their nanogap morphology. (a) Representative SEMs, (b) dark-field scattering spectra, and (c) calculated scattering spectra of AuNS−AuNC dimers with a AuNS adsorbed on the face, edge, or vertex of the AuNC. The bolder lines in (b) indicate the scattering spectra from the AuNS−AuNC dimers having the geometry shown in the SEM images in (a). Figure adapted from Ref. 48.

1.3 Applications of plasmonic nanoparticles and ensembles

Plasmonic nanostructures with high sensitivity to the surrounding medium and enhanced light absorption and scattering are good candidates for chemical sensing,[52-58] bioimaging,[59,60] and biomedical therapeutics.[61-65] The sensitivity of the SPR to the dielectric constant of the medium has been exploited for the optical detection of chemical and biological species. For practical applications, such as surface-enhanced

Raman scattering, strong enhancement of electric field is highly desired for single-molecule detection.[66-69] Strong local field enhancement can be readily found around the sharp corners, edges and conical tips of individual plasmonic nanoparticles. Appropriate spatial arrangements of plasmonic nanoparticles in ensembles can lead to even stronger enhancements.

Among all plasmonic materials, Au nanoparticles and assemblies with high biocompatibility have been extensively studied for biomedical applications such as cancer therapy and imaging.[70-73] The interaction of Au nanoparticles with light releases thermal energy, resulting in a localized temperature rise and generating acoustic waves. Thus, Au nanoparticles and assemblies are considered as a promising dual functional agent for photothermal therapy and photoacoustic imaging of cancer.[74-76]

In plasmonic ensembles, as discussed in Chapter 1.2, the extent of coupling-induced LSPR shift is dependent on the distance between the interacting nanoparticles. By characterizing the distance dependence of the plasmon coupling, Alivisatos *et al.*[77] demonstrated a strategy using the spectrum of a pair of coupled Au or Ag nanoparticles to report the interparticle distance as a "plasmon ruler" for measuring dynamic distances in biomolecular systems.[78,79]

1.4 Fabrication of plasmonic ensembles

Generally, there are two major strategies for fabricating plasmonic nanostructures with precise control: top-down lithographic techniques[80-82] and bottom-up self-assembly of nanoparticles.[83-85] Sometimes those two methods are combined to create desired ensembles,[85-87] as each has its own advantages and limitations.

1.4.1 Top-down lithographic techniques

Top-down lithography has been widely used to fabricate well-defined plasmonic arrays with precisely controlled NP shape, size, and interparticle distance.[88] With these methods, geometries as varied as split rings and coupled nanorods can be patterned with precise substrate positioning.[81,90] For example, Aizpurua *et al.*[81,82] prepared Au nanoring arrays on Si substrate by colloidal lithography with diameter of Au nanorings tuned by the size of polystyrene masks. Huang *et al.*[89] reported the fabrication of Au nanoring dimers and trimers by electron-beam lithography. Due to the high resolution of an electron beam, the spacing of trimers can be controlled precisely within several nanometers.

However, these lithographic techniques have fundamental limitations. First, the lithographic techniques suffer from either high cost or low resolution. For example, electron beam lithography and focused-ion-beam milling, which enable surface patterning with a resolution of nanometers,[91] are expensive and cannot be easily used to produce nanostructures over large areas. UV lithography suffers from both low resolution and time-consuming fabrication.[92] The reliance on clean rooms and specific instruments also increases the cost of fabrication. In addition, these techniques, although powerful for producing planar plasmonic arrays or films on 2D substrates, are generally not suitable for complex 3D fabrication. Hence, the products usually show limited plasmonic coupling within the same plane, limiting the opportunities to obtain strong coupling by vertically stacked plasmonic nanostructure, unless combined with other techniques (*e.g.,* in **Figure 1.3**).

1.4.2 Colloidal self-assembly

As a low-cost and versatile alternative, colloidal self-assembly has attracted increasing interest for fabricating plasmonic ensembles beyond 2D planes, with complex coupling modes and single particle resolution.[93] In the past decades, advances in the wet-chemical synthesis of nanoparticles have greatly boosted various approaches to bottom-up self-assembly. Generally, those assembly approaches can be classified as ligand-guided self-assembly,[94-96] interfacial self-assembly,[97,98] templated assembly,[99,100] and external-force-directed assembly.[101]

Ligand-guided self-assembly is arguably the most versatile and powerful approach to fabricate 3D plasmonic assemblies with easily tuned interparticle distance by the various surface ligands. Generally, small molecules,[102-104] biomolecules (*e.g.*, DNA and proteins),[105-109] and synthetic polymers[110-113] can serve as linkers to guide the assembly of nanoparticles by chemical, hydrophobic, or electrostatic interactions. Among surface ligands, DNA strands are extremely attractive for the precise organization of plasmonic nanoparticles, owing to their programmable base-pairing interactions. DNA strands grafted to the surface of nanoparticles guide their assembly into discrete nanoclusters or well-defined superlattices via DNA-recognition interactions.[105-107] Polymeric ligands are drawing increased interest in guiding the assembly of plasmonic nanoparticles, as the functionality can be readily tuned by the chemical composition (determining the interactions of tethered nanoparticles), persistence length (determining the interparticle distance), and conformation of polymer species. The scaling and segregation of the polymer can further enrich the assembly behavior by producing patchy particles.[114-118] Chen *et al.*[117] reported that the

coverage of polymer on NPs varied when hydrophilic ligands were mixed with hydrophobic ligands. The ligand segregation has been demonstrated on both isotropic gold nanospheres (AuNSs) and anisotropic gold nanorods to create patchy nanoparticles. More discussions and examples of ligand-guided self-assembly of plasmonic nanoparticles are presented in Chapter 3.1 and 4.1.

Interfacial self-assembly uses air/liquid or liquid/liquid interfaces as platforms for ordering nanoparticles into planar assemblies.[97,98] The organization of nanoparticles driven by the reduction in the interfacial energy:[119]

$$\Delta E = -\frac{\pi r^2}{\gamma_{A/B}} \cdot \left[\gamma_{A/B} - \left(\gamma_{P/B} - \gamma_{P/A}\right)\right]^2, \quad (1.3)$$

where r is the radius of the particle and $\gamma_{A/B}$, $\gamma_{P/B}$, and $\gamma_{P/A}$ are the interfacial tension between liquid A/liquid B, particle/liquid B and particle/liquid A, respectively. Liquid A or B can be change to air in the case of air-liquid interfaces. The fluidity of liquid interfaces provides favorable conditions for mass transport, chemical interactions/reaction in two dimensions.[120] These favorable properties of liquid interfaces have been exploited for the self-assembly of plasmonic nanoparticles into droplets in Pickering emulsions,[121] self-assembled monolayers (SAMs),[122] and hybrid films or superlattices[123-125] with tunable optical properties by altering the size of nanoparticles or the spacing between them. Controlled solvent evaporation is commonly used to modulate the concentration of nanoparticles and to confine the particles within the predetermined phase or area.[126] The method is a promising and direct alternative to lithography, although transferring the products onto other substrates can be challenging based on the mechanical properties of the assembled monolayers.

Templated assembly is an assembly process directed by a predesigned template, which can be physical confinement or a soft/chemical template. As a straightforward method, the geometry and patterning of templates dictate the spacing and spatial arrangement of plasmonic nanoparticles in their assemblies. This fabrication of physical confinements or traps to be used as templates can be done by top-down lithography. Flauraud *et al.*[90] reported the capillary assembly of Au nanorods into large-area ordered structures on substrates with predetermined surface patterns. The precise control over the organization of nanorods on the substrate was achieved by subtle design of the geometry of traps. The templated assembly can also be combined with different surface ligands to achieve better site selectivity and higher complexity of plasmonic ensembles. **Figure 1.3** shows a polymer-pore templated assembly of Au nanoparticles with various shapes modified by DNA strands into well-defined stacks.[87] To assemble nanoparticles within a confined environment, 1D pores are fabricated in a polymer-coated gold substrate using top-down lithography, and the gold surface at the bottom of each pore is densely functionalized with DNA. DNA-functionalized Au nanoparticles of controlled size and shape are then assembled in a layer-by-layer manner by designing each layer of nanoparticles to have a terminal DNA sequence complementary to that of the previous layer. The porous template is removed to generate superlattices with 2D periodicity that are composed of oriented plasmonic nanoparticles.

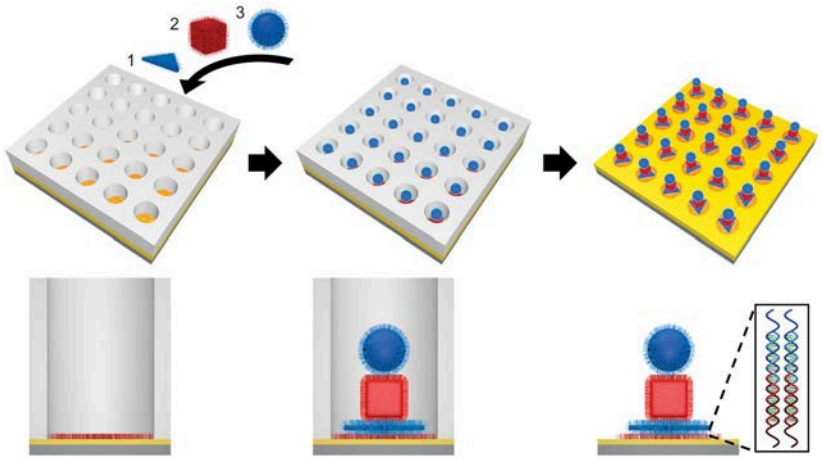

Figure 1.3 Programmable assembly of reconfigurable nanoparticle (NP) architectures. The bottom images depict cross-sectional views of a single pore. Figure is adapted from Ref. 87.

1.5 Scope of this dissertation

As discussed in the previous sections, precisely controlled synthesis and self-assembly of plasmonic nanoparticles are highly desirable for tuning their coupling and optical properties for various applications. Although top-down lithographic techniques are powerful for fabricating plasmonic ensembles, the cost can be prohibitive. In this dissertation, bottom-up techniques are explored for the fabrication of plasmonic nanoparticles and assemblies with high geometric complexity.

The objective of this dissertation is to develop wet-chemistry synthetic and self-assembly approaches for complex and defined plasmonic nanostructures. In Chapter 2, a facile synthetic method is developed for freestanding circular and triangular Au nanorings (AuNRs) with tunable sizes, thicknesses, and surface roughness. The in-plane LSPR peak of AuNRs is highly tunable through the NIR region. In Chapter 3, we combine the steric hindrance of polymeric ligand brushes and the anisotropy of

nanoparticles to create regioselective bonding between Au nanospheres and Ag nanoplates. The regioselectivity enables a self-assembly system with precise control over the relative orientation of Au nanospheres on Ag nanoplates, and the stoichiometry of reactive groups of copolymeric ligands dictates the number of nanoparticles in one cluster. Assemblies with different bonding types show different extinction spectra and electric field enhancements. In Chapter 4, regioselective self-assembly is applied to fabricate complex plasmonic nanoclusters, nanoflowers and nanobuds. The optical properties of nanobuds and nanoflowers with the same number of petals are compared in experiments and simulations. In Chapter 5, the completed work in this dissertation is summarized and future work is proposed.

Chapter 2: Controllable synthesis of Au nanorings with tunable optical response

Overview: Au nanorings have attracted intensive interests in various studies due to their unique physical properties. Synthesizing Au nanorings with controllable geometry is highly desirable for tailoring the plasmonic properties for many potential applications. This chapter describes a wet-chemistry method for synthesizing circular and triangular Au nanorings with tunable diameters, ring thicknesses, surface roughness, and hence the plasmonic response.

Part of this chapter is adapted from the article: Lin, X.; Liu, Y.; Lin, M.; Zhang, Q.; Nie, Z. Synthesis of Circular and Triangular Gold Nanorings with Tunable Optical Properties. *Chem Comm.* **2017,** *53,* 78, 10765-10767.
L. X. and N. Z. conceived and designed the experiments; L. X. performed most of experiments; L. Y. and L. M. optimized the synthetic approach; L. M. and Z. Q. helped on Raman spectroscopy and contributed in discussions. L. X. wrote the manuscript with revisions from N. Z.

2.1 Introduction

Nanorings are a unique class of nanostructures that have a solid toroidal shape. The surface of a nanoring comprises different regions with positive, zero, and negative surface curvatures, which are usually not present concurrently in other nanostructures. A nanoring also has a higher surface-to-volume ratio than a nanosphere and nanorod containing the same number of atoms, which promotes enhanced sensitivity to the surrounding medium. Gold nanorings (AuNRs) have diverse applications in biosensors, catalysis, bioimaging, and optical and electronic devices, due to their plasmonic nature and optical properties.[81,82,89,127-129] Compared with solid Au nanoparticles, AuNRs

exhibit tunable localized surface plasmon resonances (LSPRs) over a broader window of wavelengths.[81] To date, circular AuNRs have been largely fabricated on substrates by top-down lithographic approaches.[81,82] However, these methods require special equipment and are usually expensive, and cannot easily be used to create free-standing, 3D structures. Recently, a number of wet-chemical synthetic strategies have been developed for the fabrication of ring-like Au nanostructures.[130-132] Xue *et al.*[130] reported the synthesis of ultrathin triangular Au nanoframes with thicknesss of 1.8 nm to 6 nm using silver nanoplates (AgNPs) as templates. Jang *et al.*[132] synthesized nanorings with various shapes (*e.g.*, circular, triangular, and hexagonal) that featured a Pt core and Au shell by using Au nanoplates as templates. These approaches either involve complicated process (*i.e.*, multiple cycles of etching and metal deposition) or show limited control over the dimensions and optical properties of the AuNRs. Thus, there is still a great need for facile approaches to the synthesis of high-quality AuNRs with controlled geometry.

This chapter describes a wet-chemistry method using AgNPs as templates for circular and triangular AuNRs with tunable surface roughness and dimensions, and hence tunable optical properties. This method (**Figure 2.1**) involves epitaxial Au deposition on sacrificial templates of shaped Ag nanoplates, chemical etching to remove Ag, and further Au deposition to achieve the desired ring thickness.[130,133] By varying the size of the templates and amount of metal deposition, the diameter and ring thickness of AuNRs can be tuned from 50 to 400 nm and from 5 to 30 nm, respectively. The surface roughness of the AuNRs can be varied by manipulating the deposition rate/amount of Au. As a result, the in-plane LSPR peak of the AuNRs can be controlled

in the range of ~780-1350 nm. The AuNRs are further demonstrated as substrate for surface-enhanced Raman scattering (SERS) analysis of 4-mercaptobenzoic acid (4-MBA), with an enhancement factor up to 8.6×10^6, which is approximately 100-fold and 10-fold higher than that of Au nanoparticles[134] and Au polyhedral nanocrystals[135], respectively.

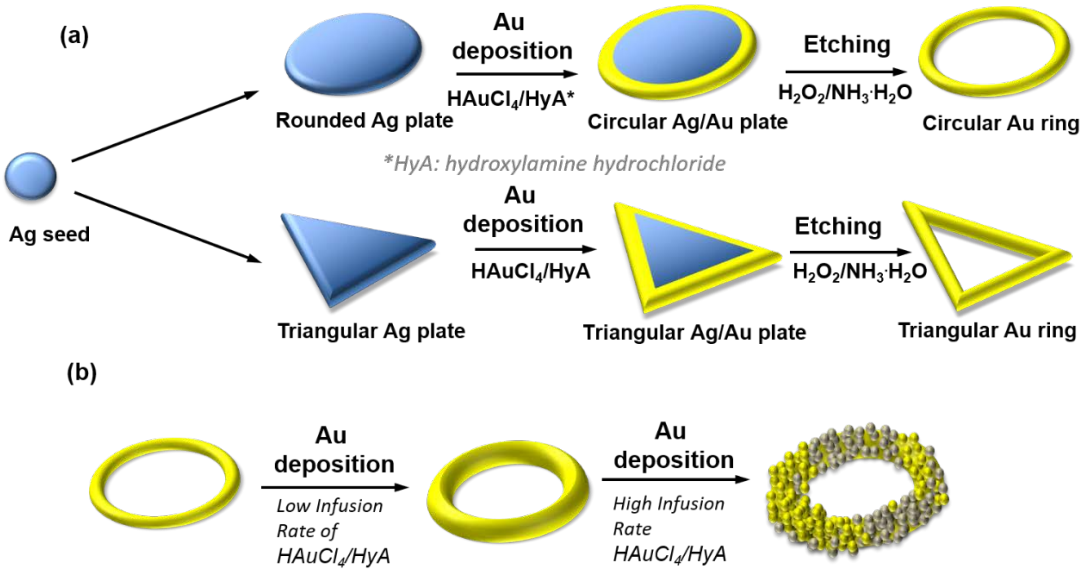

Figure 2.1 Schematic illustration for (a) the synthesis of circular and triangular gold nanorings (AuNRs) with four stages of fabrication: Ag seeds, Ag templates, Ag@Au nanostructures, and Au nanorings; and (b) the preparation of thick and rough AuNRs with different precursor infusion rates.

2.2 Experiments

2.2.1 Materials

Silver nitrate ($AgNO_3$, 99%), sodium citrate tribasic dihydrate ($C_6H_5Na_3O_7$, 99%), L-ascorbic acid ($C_6H_8O_6$, 99%), tetrachloroauric acid ($HAuCl_4$, 99.9%),

hydroxylamine hydrochloride (99%), sodium borohydride ($NaBH_4$, 99%), sodium hydroxide (99%), ammonium hydroxide solution (28.0-30.0% NH_3 basis), 4-mercaptobenzoic acid (4-MBA, 99%) were purchased from Sigma-Aldrich. Hydrogen peroxide (H_2O_2, 30%) was purchased from EMD Millipore Corporation. Acetonitrile (C_2H_3N, HPLC Grade) was purchased from Fisher Chemical. Ethyl alcohol (absolute, 200 proof) was received from Pharmco-Aaper. Deionized water (Millipore Milli-Q grade) with resistivity of 18.0 MΩ was used in all the experiments.

2.2.2 Synthesis of rounded and triangular Ag nanoplates

Ag seeds were prepared by one-shot injection of 1.2 ml $NaBH_4$ solution into a mixture of ultrapure water (200 ml), $AgNO_3$ (200 μL, 0.1 M), TSC (12 mL, 75 mM), and H_2O_2 (480 μL). The solution was gently stirred for 5 min before aging for at least 2 h. The seeds were collected by centrifugation and then dispersed in 6 mL water.

A growth solution was prepared by adding acetonitrile (20 mL), TSC (200 μL, 75 mM), ascorbic acid (300 μL, 0.1 M), and $AgNO_3$ (240 μL, 0.1 M) into water (44 mL). The shape of the Ag nanoplates was controlled by the stirring method and the stirring rate. Magnetic stirring with a moderate rate (~500 rpm) produced rounded Ag nanoplates, whereas mechanical stirring with high rate (~1000 rpm) produced triangular Ag nanoplates. The diameter/edge length of the Ag nanoplates was controlled by varying the ratio of Ag seeds to $AgNO_3$ in the growth solution. For better control over the growth kinetics, we varied the dose of Ag seeds while keeping the amount of $AgNO_3$ and volume of growth solution as constant. The addition of more seeds led to the formation of smaller Ag nanoplates. After 30 min of growth, products

were collected by centrifugation and then redispersed in 24 mL of 0.3 mM trisodium citrate aqueous solution.

2.2.3 Gold deposition of Ag@Au nanostructures

A mixture (volume ratio 50:1) of hydroxylamine hydrochloride solution (3 mM) to sodium hydroxide (0.2 M) and a $HAuCl_4$ solution (0.30 mM) were infused into a 75 ml Erlenmeyer flask containing 4 mL of Ag@Au solution via two syringes under vigorous stirring. The infusion rate was set as 2 mL/h. After 20 min of infusion, the solution was centrifuged, and the products were redispersed into 6 mL of 0.3 mM trisodium citrate.

2.2.4 Etching of Ag@Au nanoplates for Au nanorings (thin)

The wet etchant solutions (50 mM H_2O_2 and 50 mM $NH_3{\cdot}H_2O$) was introduced into 6 mL of an as-synthesized fresh Ag@Au nanostructure solution in a 50 mL Erlenmeyer flask under steady stirring by using a syringe pump (flow rate: 3 mL/h). After the solution became transparent, the thin AuNRs were collected by centrifugation and redispersed in 1 mL of a 0.3 mM trisodium citrate aqueous solution.

2.2.5 Multiple metal deposition for thick/rough AuNRs

Thick AuNRs with smooth surface were synthesized by another round of Au deposition onto the thin AuNRs at the same infusion rate (2 mL/h) of $HAuCl_4$ and basic HyA solution. After 1.5 h, the solution was centrifuged, and the products were redispersed in 1 mL of 0.3 mM trisodium citrate.

Rough AuNRs were synthesized by the same method, but at a faster infusion rate (5 mL/h) of Au precursor and reducing agent. The solution was then centrifuged after 1 h, and the products were redispersed into 1 mL of 0.3 mM trisodium citrate.

2.2.6 Calculation of enhancement factors (EFs)

We estimated the SERS enhancement factors (EFs) of 4-mercaptobenzoic acid (4-MBA) at 1590 cm^{-1} using:

$$EF = \frac{I_{SERS}}{I_{Bulk}} \times \frac{N_{Bulk}}{N_{SERS}}, \tag{2.1}$$

where I_{SERS} and I_{Bulk} are the Raman scattering intensities of 4-MBA obtained with Au NRs and bulk 4-MBA (without Au NRs), respectively, and N_{SERS} and N_{Bulk} are the numbers of 4-MBA molecules for SERS and bulk measurement, respectively.[133,136]

For bulk and SERS samples, 20 μL 10 mM 4-MBA ethanol solution is cast on substrates. We assume that 4-MBA molecules form a thin, even layer on the substrate and metal surface with a footprint of $A_{molecule} \approx 0.54$ nm^2. The surface occupation factor $f \approx 0.32$ for Au NRs. The detection spot area is $A_{focal} = 1 \times 1\ \mu m^2 = 10^{-12}\ m^2$.

$$N_{Bulk} = \frac{V \times C \times N_{Av} \times A_{focal}}{A_{Substrate}} = 3.01 \times 10^{10}, \tag{2.2}$$

$$N_{SERS} = \frac{f \times A_{focal}}{A_{molecule}} = 6 \times 10^{5}, \tag{2.3}$$

The Raman scattering intensities for bulk 4-MBA and rough triangular AuNRs were 50 and 8577, respectively.

$$EF = \frac{I_{SERS}}{I_{Bulk}} \times \frac{N_{Bulk}}{N_{SERS}} = \frac{8577}{50} \times \frac{3.01 \times 10^{10}}{6 \times 10^{5}} = 8.6 \times 10^{6}, \tag{2.4}$$

EFs for other AuNRs can be calculated in same approach.

2.27 Sample preparation for characterizations

Electron microscopy. The AuNRs were imaged using a Hitachi SU-70 Schottky field-emission gun scanning electron microscope (FEG-SEM) and a JEOL FEG transmission electron microscope (TEM). Samples for SEM were prepared by casting a 5 μL of aqueous solution on silicon wafers and dried at room temperature. TEM samples were prepared on 300 mesh copper grids.

UV-vis absorption spectroscopy. Extinction spectra of samples was measured in a range of 400-1350 nm using a PERKIN LAMBDA 35 UV/vis system.

SERS measurements. For the surface-enhanced Raman scattering (SERS) measurement, a silicon wafer was treated in an oxygen plasma cleaner for 60 s. 20 μL of an aqueous solution of the AuNR (3 mg/mL) was cast on a 0.2×0.2 cm^2 Si wafer and dried at room temperature. 4-MBA was dissolved in ethanol at concentration of 10 mM. Subsequently, a 20 μL of the 4-MBA solution was cast on the substrate. The samples were then rinsed with pure ethanol and dried. The Raman spectra were recorded using a Horiba LabRAM confocal Raman microscope equipped with a He-Ne laser (633 nm). The laser spot was focused with a spot of 1 μm^2. Raman scattering intensity was collected with an accumulation time of 5 s/cycle for 5 cycles. For each measurement, three points were selected to average to determine the final Raman intensity.

2.3 Results and discussion

2.3.1 Seed-mediated growth of Ag nanoplates

Silver nanoplates (AgNPs), also known as nanoprisms or nanodisks, are 2D plasmonic nanostructures with a shape-dependent optical response, which allows them to be used in many applications.[137-141] In this chapter, we developed a facile wet-chemistry approach to prepare both triangular and rounded AgNPs with tunable lateral dimensions, based on previously reported seed growth methods.[142,143] The diameter/edge length of AgNPs can be tuned by varying the amount of either the seed solution or the $AgNO_3$ precursor.[144] The AgNPs showed high tunability of their LSPR in the visible and NIR when the lateral dimension was tuned.[145] The citrate-stabilized AgNPs are ready to be used in templated synthesis for Au nanorings and surface modification with polymeric ligands.

The formation of anisotropic nanoplates is not thermodynamically favored, and extra efforts are needed to compete against the minimization of surface area. Preferential anisotropic growth is dependent not only upon the selective adhesion of capping ligands, but also on the crystal symmetry of the starting nuclei.[140,146] In our approach, trisodium citrate (TSC)-capped Ag nanoplates (~30 nm in size and ~5 nm in thickness) with parallel twin defects were prepared through chemical reduction,[145,147] and then used as the seeds. In the growth stage of nanocrystals, TSC also acts as a face-blocking agent that selectively binds the {111} facets of the seeds, thus slowing the growth rate of {111} and allowing extensive growth along other facets.[137,139]

In a direct chemical reduction process, Ag seeds were prepared by quickly adding $NaBH_4$ (reducing agent) to an aqueous solution of $AgNO_3$ in the presence of TSC and H_2O_2. Under magnetic stirring, the solution changed color from light yellow to dark blue in 5 min, indicating the formation of anisotropic Ag seeds, and was then incubated for 2h. In the following seed-mediated growth, a growth solution was prepared by incorporating acetonitrile, TSC, ascorbic acid, and $AgNO_3$ in water. The last four components acted, respectively, as a coordinating ligand, a face-blocking agent, a reducing agent, and a Ag(I) precursor. Acetonitrile coordinates with Ag(I), and so was added to suppress the self-nucleation of Ag.[144] Ag seeds were then added into the growth solution with predetermined seed/$AgNO_3$ ratios for different sizes of AgNPs. Rounded AgNPs were produced under magnetic stirring (~500 rpm), whereas triangular AgNPs were produced under vigorous mechanical stirring (~1000 rpm).

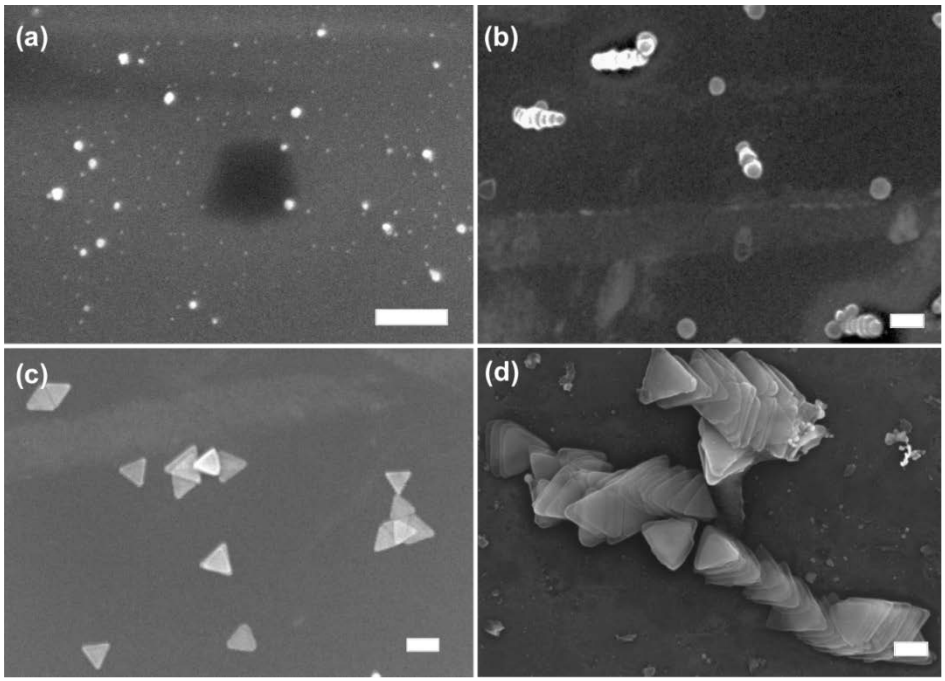

Figure 2.2 SEMs of (a) Ag seeds, (b) rounded Ag nanoplates, and triangular Ag nanoplates with edge length of (c) 100 nm and (d) 250 nm. Scale bars are 100 nm.

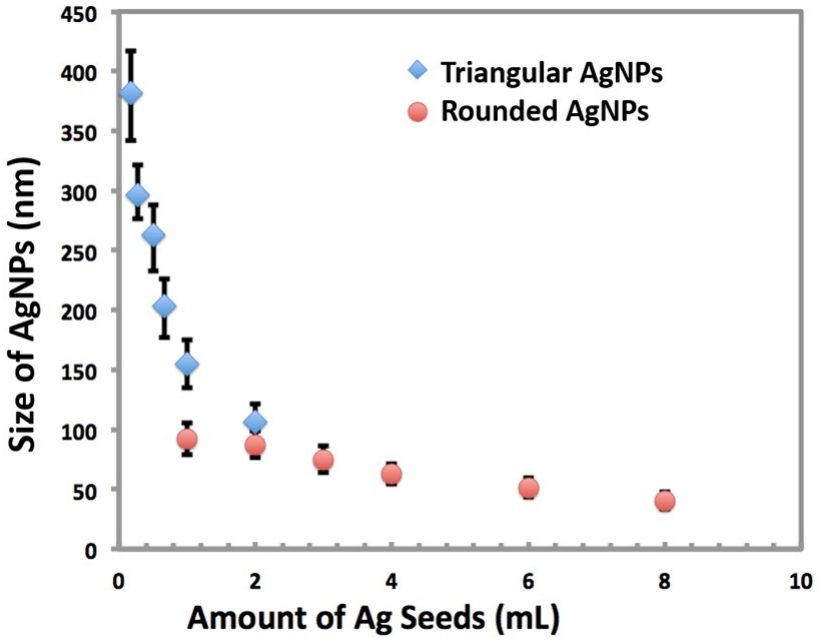

Figure 2.3 The average diameter/edge length of AgNPs as a function of the amount of Ag seed solution added in the seed-mediated growth step.

2.3.2 Templated synthesis of circular and triangular Au nanorings

The typical synthetic routes for the preparation of AuNRs are illustrated in **Figure 2.1**. First, monodisperse Ag nanoplates with rounded and triangular shapes were synthesized by the seed-mediated method (**Figure 2.2**). Two aqueous solutions, $HAuCl_4$ (Au precursor) and hydrochloride hydroxylamine (HyA, reducing agent), were then simultaneously injected into the solution of Ag nanoplates via two syringes under magnetic stirring.[148] In this process, Au atoms epitaxially deposited onto the edges of Ag templates, that is, the {110} facets, which have the highest surface energy ($\gamma_{\{111\}} < \gamma_{\{100\}} < \gamma_{\{110\}}$).[149] Subsequent removal of Ag by a mild etchant (a mixture of H_2O_2 and $NH_3{\cdot}H_2O$) produced uniform AuNRs with smooth surface.

Figure 2.4 shows representative scanning electron micrographs (SEMs) and transmission electron microscope micrographs (TEMs) of monodisperse, circular

AuNRs with diameters of 83 ± 12 nm. The AuNRs have a uniform shape and ring thickness. The thickness of the rings, which is roughly equal to the ridge thickness, can be measured from SEMs of tilted nanorings. The energy-dispersive X-ray (EDX) element mapping in **Figure 2.4** shows that the AuNRs are composed of elemental Au, although there is a trace amount of Ag background. When triangular Ag nanoplates were used as templates, the synthesis produced high-quality, equilateral triangular AuNRs with uniform ring thickness and sharp corners (**Figure 2.4b** and **Figures 2.5d-f**). The diameter/edge length of AuNRs can be tuned precisely in the range of 50 to 400 nm by controlling the amount of Ag seeds, and hence the size of Ag nanoplates. As shown in **Figure 2.4d**, the average diameter/edge length of AuNRs gradually decreased with the increase in the amount of Ag seeds added in the growth solution for the synthesis of Ag nanoplates. **Figure 2.5** shows more SEMs of circular AuNRs with different diameters (*i.e.*, 50 nm, 70 nm, and 90 nm) and triangular AuNRs with different edge lengths (*i.e.*, 90 nm, 150 nm, and 350 nm). Large-scale SEMs of AuNRs in different shapes are presented in **Figure 2.6** with size distribution.

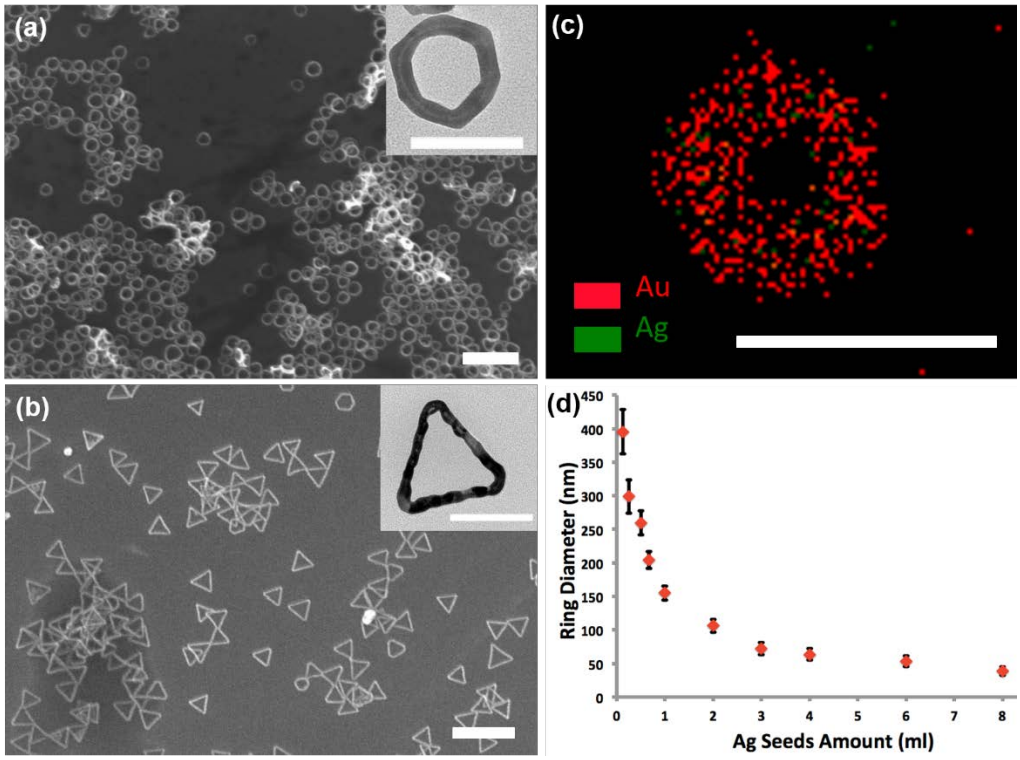

Figure 2.4 SEMs and TEMs (inset) of circular AuNRs with diameter of 83 ± 12 nm (a) and triangular AuNRs with edge length of 115 ± 22 nm (b). (c) EDX mapping of Au and Ag in a circular AuNR. (d) The average diameter of AuNRs as a function of the amount of Ag seeds added in the template synthesis step. Scale bars are 300 nm in (a) and (b), and 100 nm in (c) and all insets.

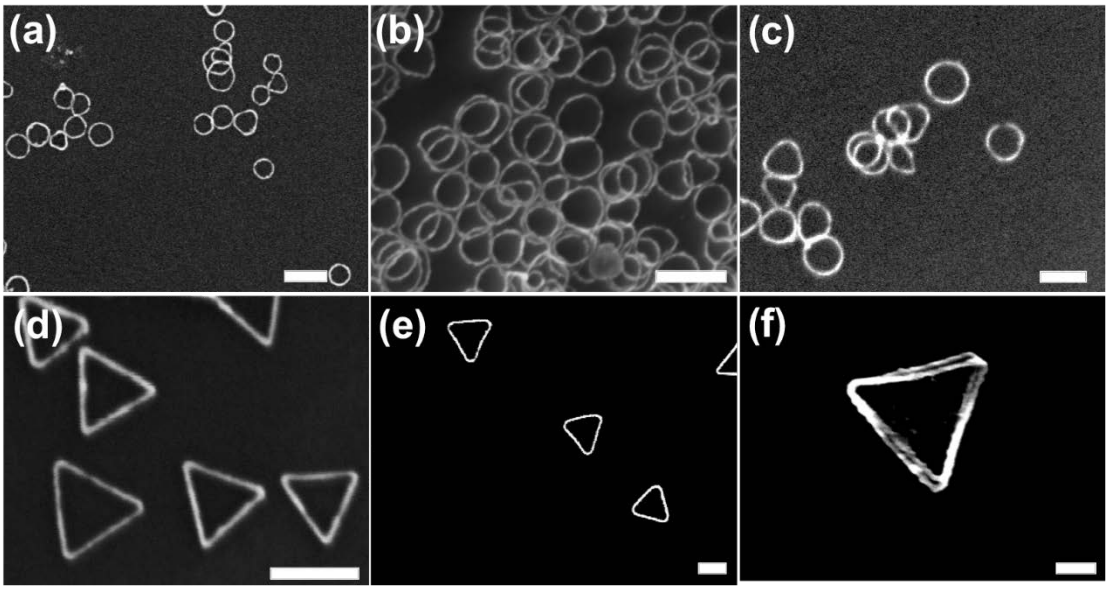

Figure 2.5 SEMs of circular and triangular AuNRs with different sizes. (a-c) Circular AuNRs with different diameters synthesized with the addition of (a) 4 mL, (b) 3 mL, and (c) 2 mL of Ag seed solution. (d-f) Triangular AuNRs with different edge lengths synthesized with the addition of (d) 2 mL, (e) 1 mL, and (f) 0.125 mL of Ag seed solution. Scale bars are 100 nm.

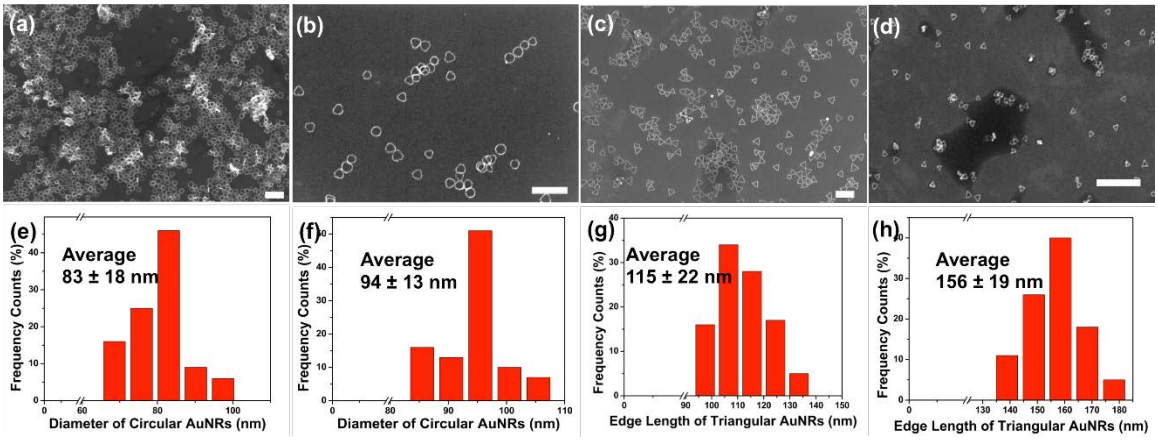

Figure 2.6 Large-scale SEMs of (a), (b) circular and (c), (d) triangular AuNRs with size distribution in (e-h), respectively. Scale bars are 300 nm in (a-c) and 1000 nm in (d).

2.3.3 Thickness and surface roughness of Au nanorings

It is known that the LSPR of AuNRs is strongly dependent on their ring thickness.[81] Our synthetic method allows for precise control over the ring thickness ranging from 5 to 30 nm by controlling the metal deposition before or/and after the removal of Ag templates. Increasing the deposition time from 20 to 45 min led to a slight increase in the ring eidth from 2 to 6 nm when Ag templates were not removed.[130] Further increase in the deposition time caused the deposition of Au onto not only the {110} facets, but also the {111} facets, and hence the complete coating of Ag nanoplates by Au[133]. This issue can be resolved by multiple Au post-deposition processes using thin AuNRs (with Ag nanoplates removed) as seeds. **Figure 2.7** shows SEMs of circular AuNRs with ring thicknesses in the range of 7 to 22 nm that were prepared by varying the amount of Au deposition. The ring thickness grows uniformly to form smooth, thick AuNRs. **Figure 2.8** shows SEMs of triangular AuNRs with ring thicknesses in the range of 10 to 30 nm. The Au deposition occurred on both inner and outer surfaces of the ring ridges, as indicated by a slight increase of outer diameter/edge length and a clear decrease of the inner diameter/edge length.

The surface roughness of AuNRs can be tuned by adjusting the infusion rate and time of $HAuCl_4$ and HyA solutions. A high infusion rate in combination with a low stirring rate facilitates the production of AuNRs with a high surface roughness **(Figure 2.9)**. We presume that the insufficient diffusive time of precursor towards the seed surface leads to the uneven nucleation and deposition of Au on surface of AuNRs.

2.3.4 Tunable optical properties of Au nanorings

We monitored the evolution of LSPR spectra over the course of metal deposition using UV-vis-NIR spectroscopy. Generally, AuNRs exhibit two distinct peaks: one in the visible region, corresponding to the out-of-plane resonance mode, and one in the NIR region originating from the in-plane resonance mode.[81] As shown in **Figure 2.7d**, the 1050 nm LSPR peak of circular AuNRs blue-shifts to 780 nm with progressive Au deposition, whereas the peak at 490 nm red-shifts slightly to 510 nm. This result is in good agreement with previous findings, as the decrease of void size and increase of ring thickness result in an enhancement of the out-of-plane resonance but a decrease in the in-plane resonance.[81]

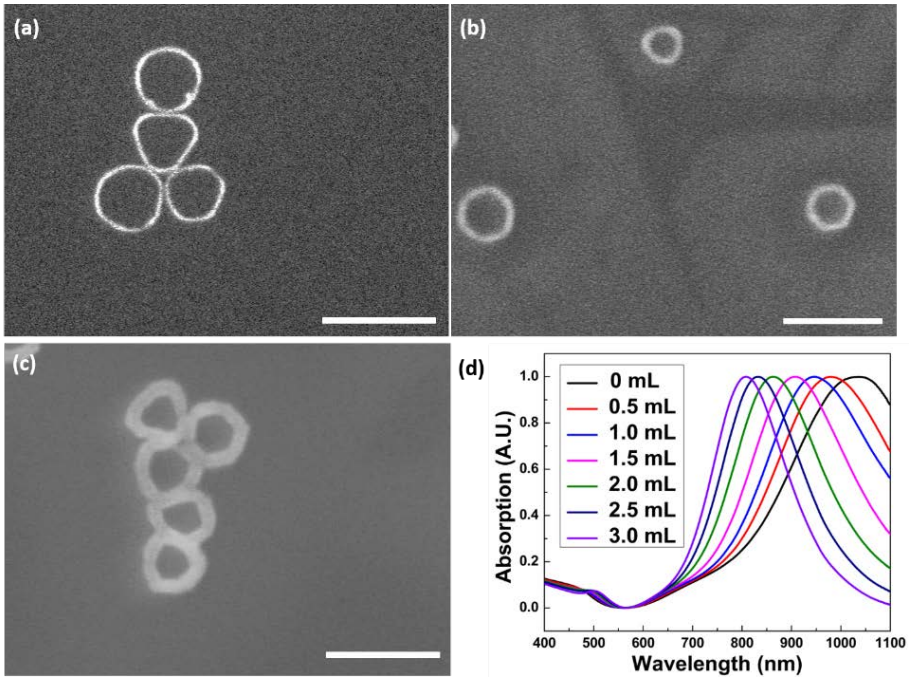

Figure 2.7 SEMs of circular AuNRs with an average ring thickness of (a) 7 nm, (b) 15 nm, (c) 22 nm. (d) Corresponding UV-vis-NIR spectra through the post-deposition growth of the samples in (a-c). The samples were obtained by adding different amounts of the Au precursor solution: (a) 0 mL, (b) 1.5 mL, and (c) 3.0 mL.

Triangular AuNRs with ~ 100 nm edge length exhibited an in-plane LSPR peak located within the second NIR window (1000 to 1350 nm, **Figure 2.8d**), which is highly desirable for optical theranostics, where light has deeper tissue penetration and higher signal-to-noise ratio comparing with light at shorter wavelengths.[150] The unnormalized peaks also showed decreasing intensity of the LSPR peak corresponding to the in-plane polariztion as the ring thickness increases, whereas the out-of-plane peak showed increasing intensity as the growth of ring thickness.

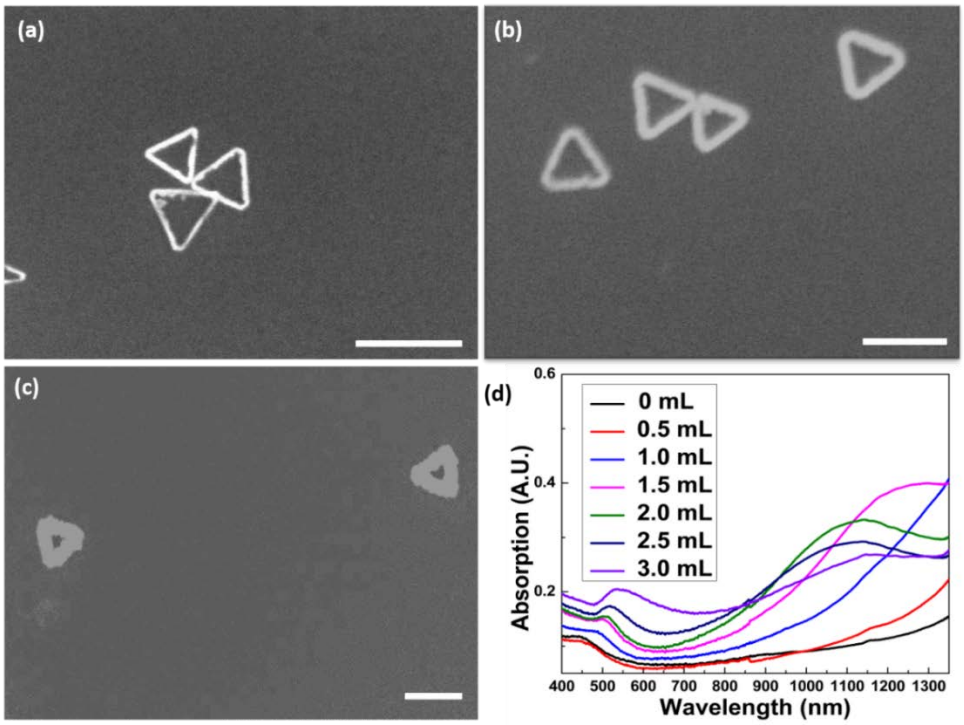

Figure 2.8 SEM images of triangular AuNRs with an average thickness of (a) 10 nm, (b) 21 nm, and (c) 30 nm. (d) Corresponding UV-vis-NIR spectra through the post-deposition growth of the samples in (a-c). The samples were obtained by adding different amounts of the Au precursor solution: (a) 0 mL, (b) 1.5 mL, and (c) 3.0 mL.

We also monitored growth process of ring surface roughness at high infusion rate (4 mL/h) of Au precursor and reducing agent solutions by SEM and UV-vis-NIR spectroscopy. The increase in the surface roughness of AuNRs is accompanied by an obvious broadening of the out-of-plane LSPR peak and increasing of absorption intensity (**Figure 2.9d**). The nonuniform growth of the irregular tips on the surface of the AuNRs results in the peak broadening. And the increased intensity of the out-of-plane mode is attributed to the decrease of void size and increase of nanoparticle volume during the growth process.[81]

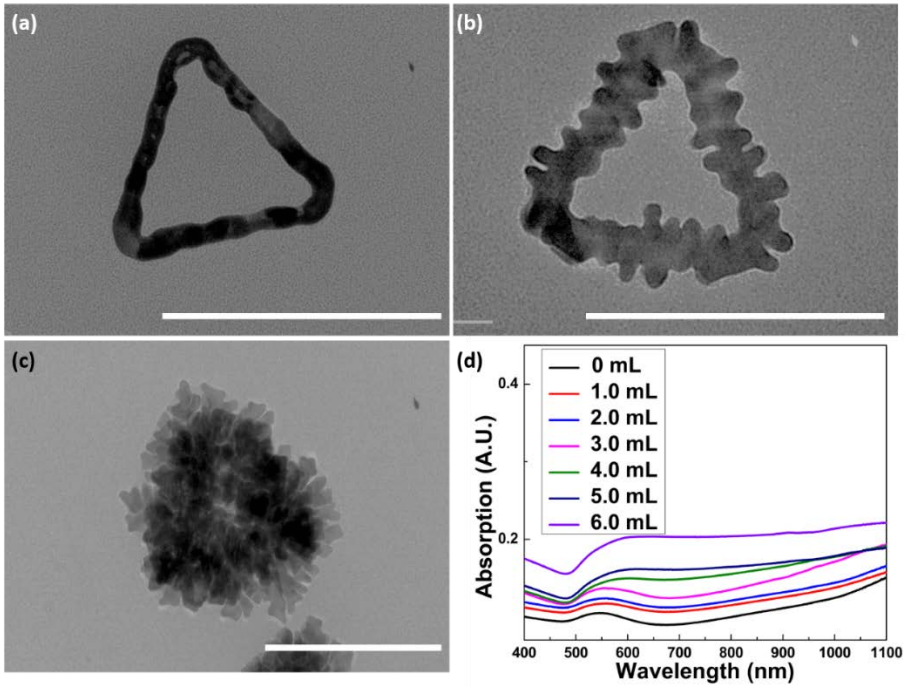

Figure 2.9 TEMs of triangular AuNRs with (a) smooth, (b) rough, and (c) super-rough surfaces. (d) Corresponding UV-vis-NIR spectra through the post-deposition growth of the samples in (a-c). The samples were obtained by adding different amounts of the Au precursor solution: (a) 0 mL, (b) 3.0 mL and (c) 6.0 mL. The scale bars are 150 nm.

2.3.5 Surface-enhanced Raman scattering with Au nanorings

Plasmonic nanostructures with rough surface and/or sharp corners are attractive for SERS detection, because such structures tend to have a large number of efficient electromagnetic enhancement spots.[151] As a demonstration, we explored the use of circular and triangular AuNRs as substrates for SERS detection (**Figure 2.10**). The SERS substrates were prepared by casting and drying a solution of AuNRs on Si wafer to form a thin film. A common Raman probe, 4-mercaptobenzoic acid (4-MBA), which has two characteristic bands at about 1590 and 1080 cm^{-1} associated with the ν_{8a} (a_1) and ν_{12} (a_1) aromatic ring vibrations,[133] was used as a probe molecule. As shown in **Figure 2.10**, our AuNRs exhibit SERS enhancement factors (EFs) that are significantly larger than those of Au nanoparticles[134] and Au polyhedral nanocrystals.[135] The EFs were dependent on the shape, ring thickness, and surface roughness of AuNRs. When the thickness of AuNRs increased from 10 to 20 nm, the EFs increased from 4.1×10^6 to 4.6×10^6 and from 4.2×10^6 to 5.1×10^6 for circular and triangular AuNRs, respectively (see 2.2.6 for detailed calculations). Compared with AuNRs with smooth surfaces, the EFs of circular and triangular AuNRs (20 nm in ring thickness) with rough surfaces increased to 6.5×10^6 and 8.6×10^6, respectively. This observation can be explained by the presence of more 'hot spots' of the irregular tips on the surface and stronger enhancement at sharper tips.[152] Overall, triangular AuNRs showed a ~32% higher EF than did circular AuNRs, due to a closer edge-to-edge distance and the presence of corner-to-edge coupling. For triangular AuNRs with rough surface, the close edge-to-edge distance further facilitated the coupling between sharp tips.

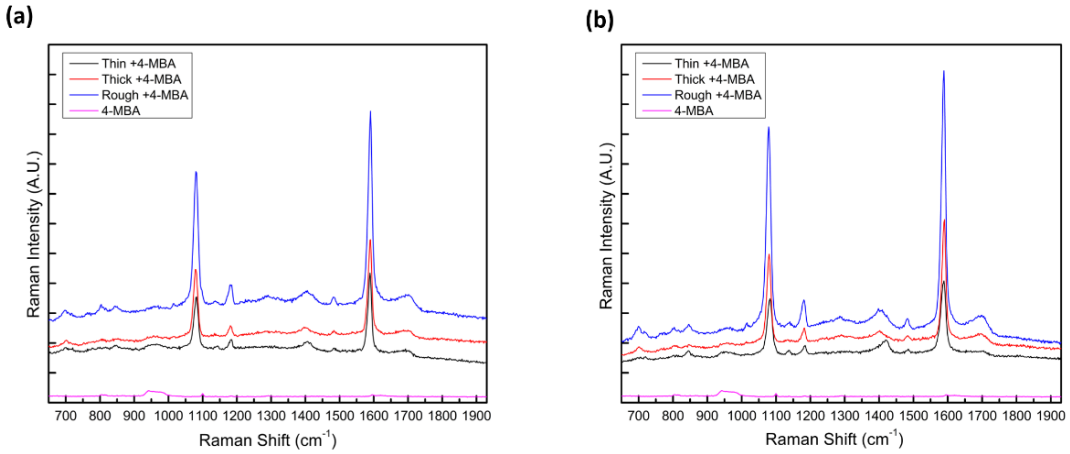

Figure 2.10 (a) Raman spectra of 4-MBA (pink) and surface enhanced Raman scattering with thin (black), thick (red), and rough (blue) circular AuNRs. (b) Raman spectra of 4-MBA (pink) and surface enhanced Raman scattering with thin (black), thick (red), and rough (blue) triangular AuNRs.

2.4 Conclusion

In summary, we demonstrated a facile wet-chemistry method using Ag nanoplates as sacrificial templates for the synthesis of uniform circular and triangular AuNRs with tunable size, ring thickness, and surface roughness. These AuNRs exhibit tunable LSPR peaks in the visible and NIR regions by tuning the geometric parameters, thus enabling potential applications in sensing, catalysis, and optical biomedicine within the NIR window. As a demonstration, we showed that triangular rings with rough surfaces exhibit an EF of up to 8.6×10^{6} for SERS analysis of 4-MBA.

Chapter 3: Polymeric ligand-mediated regioselective bonding of plasmonic nanospheres and nanoplates

Overview: In the design of nanoparticle assemblies, directional interactions play a crucial role in controlling the spatial arrangement and orientation of the building blocks. Sophisticated surface ligands facilitate the formation of directional bonding via specific interactions. Anisotropic building blocks have also attracted much attention, with their unique geometries and shape constraints. In this chapter, we combine the steric hindrance of polymeric ligand brushes and the anisotropy of nanoparticles to create regioselective bonding for a self-assembly system with precise control of the relative orientation of gold nanospheres on silver nanoplates. This simple, yet versatile, strategy produces assemblies with high regioselectivity and high yields of each assembly. Two representative types of assemblies with different bonding modes show different shifts in extinction spectra and electric field enhancement patterns. This chapter provides new tools for designing plasmonic nanoclusters with increased complexity and optical functionality.

This chapter is adapted from the manuscript published in the following article: Lin, X.; Ye, S.; Kong, C.; Webb, K.; Yi, C.; Zhang, S.; Zhang, Q.; Fourkas, J. T.; Nie, Z. Polymeric Ligand-Mediated Regioselective Bonding of Plasmonic Nanoplates and Nanospheres. *J. Am. Chem. Soc.* **2020,** 142, 41, 17282-17286.

L. X. and N. Z. conceived and designed the experiments; L. X. performed most of experiments; Y. S. performed the simulations of optical properties; W. K., Y. C., and Z. S. contributed in the synthesis of polymers and discussion of self-assembly; K. C. and Z. Q. helped on electron microscopy and contributed in discussions. L. X. wrote the manuscript with revisions from F. J. T., and N. Z.

3.1 Introduction

Inorganic nanoparticles (NPs) often exhibit intriguing optical, electronic and magnetic properties that are dependent on size, shape and composition.[8] Controllable organization of NPs into small clusters allows for modulation of collective physical properties that arise from interactions among surface plasmons, excitons, and magnetic moments of NPs.[153-156] These synergistic properties of assembled NPs have enabled the diverse applications of NP clusters in areas including photonics,[157] sensing,[158] catalysis,[159] energy harvesting,[160] and surface-enhanced spectroscopy.[161] The coupling modes and strengths of NPs are strongly dependent not only on the physical traits of constituent NPs, but also on the interparticle distance, and particularly on the spatial arrangements of NPs in the clusters.[7,48,162,163] Specific and directional bonding between individual plasmonic NPs are both highly desirable to achieve precise control over spatial arrangements and orientations, and hence the plasmonic coupling.

Several strategies can be used to introduce directional interactions to assemble NPs into defined clusters, including site-specific functionalization of NPs with surface patches,[117,118,166-168] positioning of NPs on DNA nanostructures with specific binding sites,[169-171] and confined assembly of NPs in droplets[172] or nano-grooves.[87,173] In particular, assembly of NPs tethered with complementary, single-stranded DNAs at specific surface regions has led to a range of small clusters with configurations resembling the structure and symmetry of molecules (so-called colloidal molecules). However, these assembly approaches either show low yield of desired products or require extensive molecular engineering or sophisticated NP functionalization to break

the symmetry on the surface of NPs.[117,118] Programmable assembly of NPs, and especially shaped NPs, into precisely controlled clusters remains challenging.

In this chapter, a polymer-shielding-mediated strategy is described for programming the regioselective bonding of non-patchy plasmonic nanoplates (NP-**A**) and nanospheres (NP-**B**) into discrete clusters with defined geometry and NP orientation. The surfaces of the binary NPs are uniformly grafted with block copolymer ligands in which the NP-adjacent reactive block carries complementary weak acid or base groups for bonding, and the non-reactive block acts as stabilizers for the NPs. The steric hindrance of polymeric ligands on anisotropic nanoparticles with different surface curvature creates physically distinct regimes, allowing the for the formation of two different types of bonding, edge-type and face-type, with precise control of the relative orientation of gold nanospheres on silver nanoplates. Two representative types of assemblies with different bonding modes are also investigated in extinction spectra and electric-field enhancement patterns by experiments and simulations.

3.2 Experiments

3.2.1 Materials

Gold (III) chloride trihydrate ($HAuCl_4 \cdot 3H_2O$, ≥ 99.9% trace metals basis), sodium citrate tribasic dihydrate (≥ 99%), silver nitrate ($AgNO_3$), L-ascorbic acid, tetrahydrofuran (THF), N, N-dimethylformamide (DMF), and dimethyl sulfoxide (DMSO) were purchased from Sigma-Aldrich and were used as received. Styrene (St) and N, N-dimethylaminoethyl methacrylate (DMAEMA) were passed through an Al_2O_3 column to remove inhibitors. Acrylic acid (AA) was distilled under vacuum

before use and stored in freezer at −20 ℃. Azobis(isobutyronitrile) (AIBN) was recrystallized twice from ethanol. PEO_{45}-CTA, was synthesized by coupling poly(ethylene oxide) methyl ether (PEG_{45}-OH, and PEG_{113}-OH, molecular weights 2 $Kg \cdot mol^{-1}$ and 5 $Kg \cdot mol^{-1}$, respectively) with 4-cyano-4-(phenylcarbonothioylthio) pentanoic acid (CPPA) through esterification.[174] Deionized water (Millipore Milli-Q grade) with resistivity of 18.0 MΩ was used in all of the experiments.

3.2.2 Synthesis of Au nanospheres and Ag nanoplates

AuNSs were synthesized using methods previously reported.[174] 10 mg of $HAuCl_4 \cdot 3H_2O$ solid was dissolved in 500 mL of water and heated to a boil under stirring. 10 mL of sodium citrate aqueous solution (1 wt %) was quickly added into the solution, and the solution was kept boiling for 30 min to produce Au nanoparticles (NPs) with a diameter of ~15 nm. The as-prepared AuNPs were used as seeds for further growth of larger AuNSs in the presence of sodium citrate at 90 ℃. The diameter of the AuNSs (in the range of ~18-40 nm) was tuned by varying the concentration of the $HAuCl_4$ precursor in the growth solution. The resulting AuNSs were collected by centrifugation.

AgNPs were synthesized by seed-mediated growth method described in Chapter 2.2.2.

3.2.3 Synthesis of thiol-terminated *di*-block copolymers

Thiol-terminated PEO-*b*-P(DMAEMA-*r*-St)-SH and PS-*b*-P(AA-*r*-St)-SH copolymers were synthesized using reversible addition fragmentation chain-transfer (RAFT) polymerization. The synthetic procedures are illustrated in **Figure 3.1**.

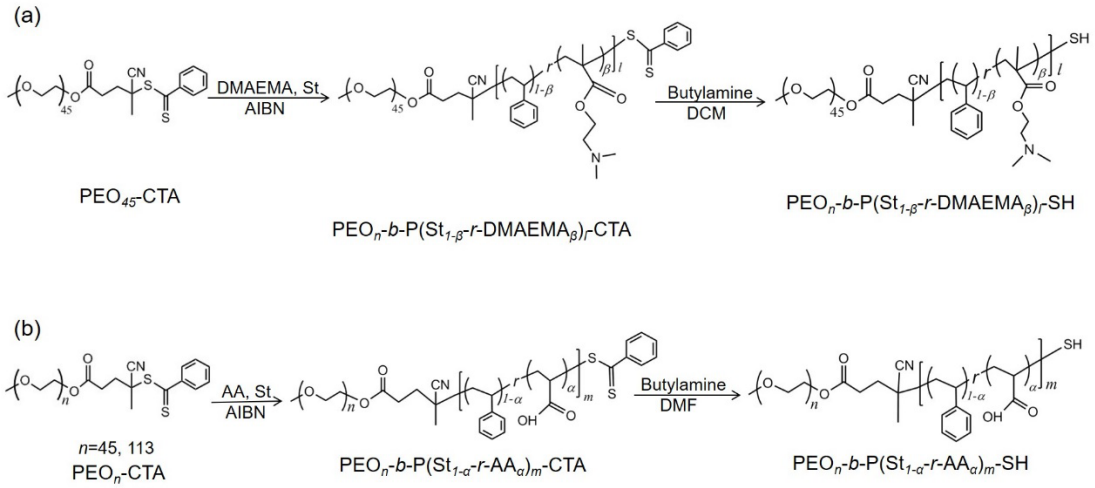

Figure 3.1 The synthetic routes of thiol-terminated copolymers: (a) PEO_n-*b*-$P(DMAEMA_{\beta}$-*r*-$St_{1-\beta})_l$-SH and (b) PEO_n-*b*-$P(AA_{\alpha}$-*r*-$St_{1-\alpha})_m$-SH. The non-reactive block PEO can also be replaced by PS if the macro-RAFT agent is replaced with PS-CTA.

3.2.3.1 Synthesis and characterization of PEO-b-P(DMAEMA-r-St)-SH.

Figure 3.1a shows the route for the synthesis of thiol-terminated PEO_{45}-*b*-$P(DMAEMA_{\beta}$-*r*-$St_{1-\beta})_l$ [where l and β are the number of repeat units and the content (molar fraction, %) of the DMAEMA monomer in the randomly copolymerized block, respectively]. PEO-*b*-P(DMAEMA-*r*-St)-CTA was synthesized using PEO-CTA as the macroinitiator. Using PEO_{45}-*b*-$P(DMAEMA_{0.40}$-*r*-$St_{0.60})_{419}$-SH as an example, 0.2 g of PEO-CTA, 7.29 g of styrene, 4.76 g of DMAEMA and 1.64 mg of AIBN were mixed and dissolved in 5 mL of anhydrous anisole in a 25 mL Schlenk flask. The reaction mixture underwent three freeze-pump-thaw cycles of 10 min each, and then was refilled with argon for 30 min. The flask was then placed in a 65 ℃ oil bath. Polymerization proceeded under magnetic stirring for 30 h. To terminate the polymerization, the reaction mixture was quickly cooled to room temperature by placing the flask in liquid

N_2. The polymer was purified by three precipitations in hexane and petroleum ether, and then was dried under vacuum for 24 h. To obtain thiol-terminated polymers, as-synthesized dithioester-terminated PEO-*b*-P(DMAEMA-*r*-St)-CTA was dissolved in DMF with excess *n*-butylamine (50 equivalents of the amount of the RAFT agent), and the mixture was stirred under nitrogen for 2 h. The dithioester end groups were reduced to thiols, as confirmed by the color change of the solution from red to light yellow. The product was purified to remove excess *n*-butylamine by three cycles of precipitation in cold hexane and re-dissolution in THF and was subsequently dried under vacuum at room temperature overnight.

Based on the ^{1}H NMR spectrum (in $CDCl_3$, see **Figure 3.2**), the molecular weight $M_{n(\mathrm{NMR})}$ is 54.5 Kg·mol^{-1}, as determined by comparing the integrals of the resonance peaks of the aromatic ring of PS block (6.4-7.3 ppm), the methylene groups of PEO-CTA (3.62-3.66 ppm), and methyl groups of DMAEMA block (0-1 ppm). By varying the amount of AIBN and the reaction time, PEO-*b*-P(DMAEMA-*r*-St)-SH copolymers with different lengths and charge ratios were synthesized, as summarized in **Table 3.1**.

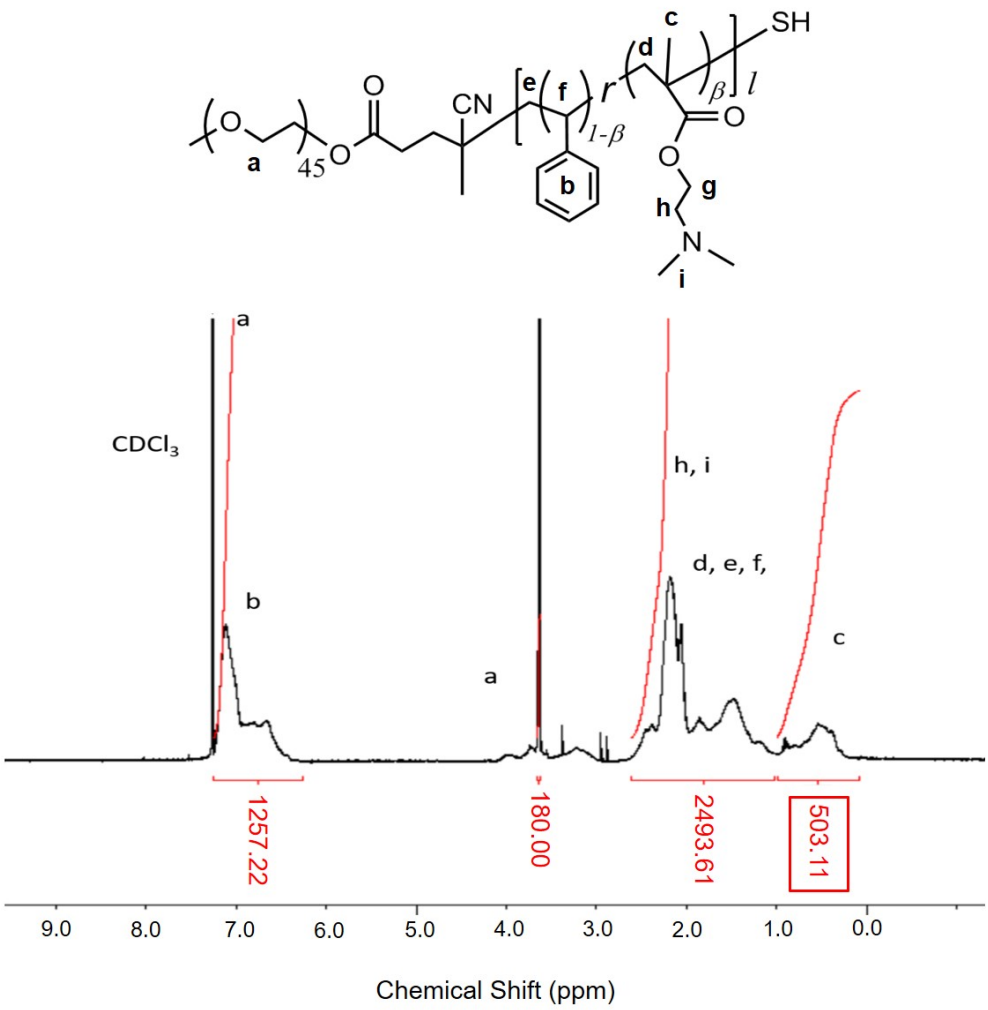

Figure 3.2 ^{1}H NMR spectrum of a representative copolymer ligand: PEO_{45}-*b*-$P(DMAEMA_{0.40}$-*r*-$St_{0.60})_{419}$-SH.

3.2.3.2 Synthesis of thiol-terminated PEO-b-P(AA-r-St)-SH

Figure 3.1b shows the synthetic route for the thiol-terminated block copolymer of PEO_{45}-*b*-$P(AA_{\alpha}$–*r*-$St_{1-\alpha})_{m}$, where *m* and α are the number of repeat units and content (mole fraction) of AA monomer in the randomly copolymerized block, respectively.

In the synthesis of PEO_{45}-*b*-$P(AA_{0.32}$-*r*-$St_{0.68})_{335}$, PEO_{45}-CTA (0.1 g, 0.05 mmol), AIBN (1.62 mg, 0.01 mmol), styrene (1.70 g, 16 mmol) and AA (0.50 g, 7 mmol) were

dissolved in 3 mL dioxane in a 25 mL Schlenk flask. The mixture was degassed by three freeze-pump-thaw cycles. The flask was then placed in a pre-heated oil bath at 75 °C for the desired time under magnetic stirring. Liquid N_2 was used to cool the solution quickly to room temperature to terminate the polymerization. The mixture was diluted with THF and then precipitated twice in hexane. The obtained pink precipitate was dried under vacuum at 40 °C overnight.

To release the thiol end-group, as-synthesized copolymers were treated with *n*-butylamine, with a minor modification of a literature procedure.[174] Briefly, 1.0 g of PEO-*b*-P(AA-*r*-St)-CTA was dissolved in 5 mL DMF. An excess amount of *n*-butylamine (~ 0.5 mL) was diluted with 10 mL of DMF, and the mixture was added dropwise to the polymer solution under stirring. The reaction proceeded under an argon atmosphere for 3 h. With the addition of the *n*-butylamine solution, the mixture became cloudy, due to the formation of insoluble copolymers by the neutralization of carboxyl groups of the copolymers with *n*-butylamine. To avoid gelation and to dissolve the copolymers, 10 mL of DI water was added dropwise to the mixture under stirring. After the reaction was complete, the solution was neutralized, and the polymer was precipitated in excess 0.5 M HCl aqueous solution in an ice-water bath. The precipitate was filtered and washed with excess deionized water to remove residual acids and salts. Finally, the copolymers were dissolved in 15 mL of THF and precipitated by adding 25 mL of petroleum ether. The white powder product was dried at 40 °C under vacuum for two days.

^{1}H NMR spectroscopy was used to determine the degree of polymerization and composition of the random P(AA_{α}-*r*-$St_{1-\alpha}$)$_m$ blocks. According to the ^{1}H NMR spectrum

of the copolymer in DMSO-*d*6 (**Figure 3.3**), the number-average molecular weight, $M_{n(NMR)}$ of the product was 33.4 Kg·mol^{-1} and the mole fraction of -COOH groups, α, was ~0.32, as calculated by using the integrals of the resonance peaks of -C<u>H</u>$_2$C<u>H</u>$_2$O– from the PEO block (3.62 ~ 3.66 ppm).

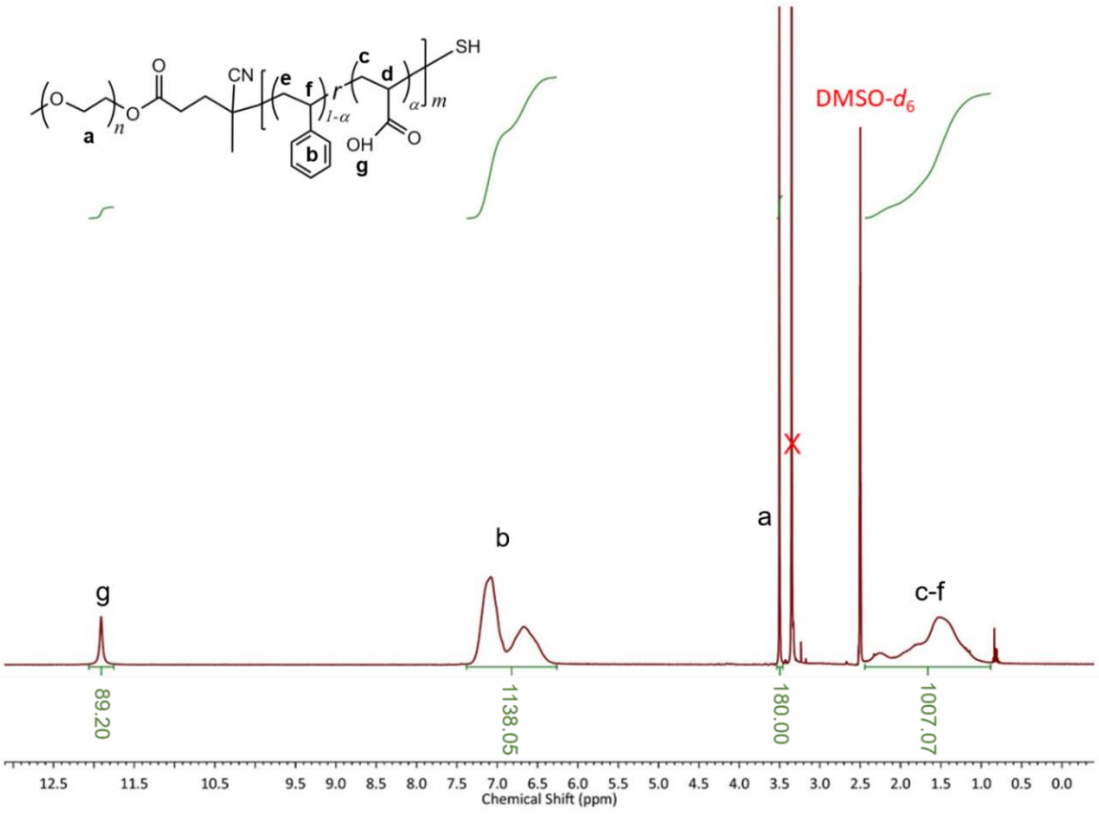

Figure 3.3 ^{1}H NMR spectrum of a representative copolymer ligand: PEO$_{45}$-*b*-P(AA$_{0.32}$-*r*-St$_{0.68}$)$_{335}$-SH.

3.2.3.3 Synthesis of thiol-terminated PS-b-P(AA-r-St)-SH

Synthesis of macro-RAFT chain transfer agent (PS-CTA): PS-*b*-P(AA-*r*-St)-CTA was synthesized using PS-CTA as the first block. For PS$_{111}$-CTA, CPDB (44.0mg, 0.2 mmol), AIBN (1.62 mg, 0.01 mmol), and styrene (15.6 g, 0.15 mol) were added to a

50 mL Schlenk flask. The mixture was degassed by three freeze-pump-thaw cycles, and then reacted at 85 ℃ for 11 hours under magnetic stirring. To terminate the polymerization reaction, liquid N_2 was used to cool the solution quickly to room temperature. The polymer was precipitated in hexane 3 times and dried under vacuum for 24 h.

For PS_{111}-*b*-P(AA-*r*-St)-CTA, the as-synthesized macro-RAFT agent PS_{111}-CTA (0.95 g, 0.10 mmol), AA (0.97 g, 13.5 mmol), styrene (3.28 g, 31.5 mmol), and AIBN (1.64 mg, 10 μmol) were dissolved in a 6 mL of dioxane in a 25 mL Schlenk flask. The mixture was degassed by three freeze-pump-thaw cycles, stirred under argon for 30 min, and then reacted at 75 ℃ for 24 h under magnetic stirring. After the polymerization reaction was complete, the solution was cooled down to room temperature by using liquid N_2. The polymer was precipitated three times in hexane and petroleum ether, and then dried under vacuum for 24 h.

To convert the terminal group from a dithioester to a thiol, PS-*b*-P(AA-*r*-St)-CTA was dissolved in DMF with excess *n*-butylamine (50 eq.), and the mixture was stirred under nitrogen for 2 h. The mixture was then transferred into an ice bath, with a dropwise addition of excess 37% HCl to neutralize and precipitate the product. The polymer was then washed several times with water, to remove residual acid and salt, was precipitated twice in petroleum ether, and then was dried under vacuum for 24 hours. The parameters of PS-*b*-P(AA-*r*-St)-SH and other copolymers used are given in **Table 3.1**.

Table 3.1 Characterization of Copolymers*

Copolymer compositions	α (β)	M_n, (Kg·mol^{-1})	R_0 (nm)
PEO_{45}-*b*-P($DMAEMA_{0.32}$-*r*-$St_{0.68}$)$_{98}$-SH	0.32	13.9	7.9
PEO_{45}-*b*-P($DMAEMA_{0.41}$-*r*-$St_{0.59}$)$_{158}$-SH	0.41	21.6	9.9
PEO_{45}-*b*-P($DMAEMA_{0.30}$-*r*-$St_{0.70}$)$_{244}$-SH	0.30	31.3	11.5
PEO_{45}-*b*-P($DMAEMA_{0.40}$-*r*-$St_{0.60}$)$_{419}$-SH	0.40	54.5	15.7
PEO_{113}-*b*-P($AA_{0.26}$-*r*-$St_{0.74}$)$_{249}$-SH	0.26	28.8	16.9
PS_{111}-*b*-P($AA_{0.31}$-*r*-$St_{0.69}$)$_{289}$-SH	0.31	38.8	13.2
PEO_{45}-*b*-P($AA_{0.30}$ -*r*-$St_{0.70}$)$_{185}$-SH	0.30	19.5	8.9
PEO_{45}-*b*-P($AA_{0.32}$ -*r*-$St_{0.68}$)$_{335}$-SH	0.32	33.4	11.8
PEO_{45}-*b*-P($AA_{0.36}$ -*r*-$St_{0.64}$)$_{467}$-SH	0.36	45.2	13.7
PEO_{45}-*b*-P($AA_{0.32}$ -*r*-$St_{0.68}$)$_{550}$-SH	0.32	53.6	15.2

* The molecular weight M_n, (Kg·mol^{-1}) was calculated from ^{1}H NMR measurements. The root-mean-square end-to-end distance, R_0 (nm), was calculated from $R_0 = N^{0.5}b$, where b is the Kuhn length (b = 1.8 nm for PS, b = 1.1 nm for PEO) and N is the number of Kuhn segments calculated from the molar mass of the Kuhn monomer M_0 (M_0 = 720 g/mol for PS and M_0 = *137* g/mol for PEO).

3.2.4 Surface modification of NPs and self-assembly

Ag and Au NPs were functionalized using a ligand-exchange method reported previously, with minor modifications.[174, 115] Taking functionalization of 26 nm Au nanospheres with PEO_{45}-*b*-P($DMAEMA_{0.32}$-*r*-$St_{0.68}$)$_{335}$-SH as an example, 15 mg of PEO_{45}-*b*-P($DMAEMA_{0.32}$-*r*-$St_{0.68}$)$_{335}$-SH was dissolved in 10 mL of DMF in a 20 mL vial. A 2 mL dispersion of Au nanospheres in DMF (~2 mg/mL) was added dropwise into the above solution under sonication. The mixture was sonicated for another 1 h and incubated overnight to allow for complete ligand exchange. The copolymer-grafted NPs were purified to remove untethered copolymers by 10 cycles of centrifugation (each for 11,000 rpm for 18 min at 20 °C, NPs were collected and redispersed in 2 mL DMF between cycles). The NPs were re-dispersed in 4 mL of THF at an estimated

concentration of ~ 3 nM for future use. For Ag nanoplates, the procedure for the surface modification was the same as that for Au nanospheres, except that the mixture of Ag nanoplates and copolymers was incubated for 1 h after vigorous shaking to allow for complete ligand exchange.

The assembly of NP clusters was triggered by mixing binary building blocks in THF, a good solvent for the copolymer ligands, at predetermined concentrations. Taking edge-type $\mathbf{AB_2}$ structures as an example, 50 μL of the stock solution of NP-**A**s in THF (~ 1.48 nM) was added to a 4 mL glass vial containing 1.0 mL THF, followed by the addition of different amounts of the stock solution of NP-**B**s under sonication for ~ 20 s. The mixture was then sonicated for 3 min and incubated for ~ 2 h.

The samples were imaged by scanning electron microscopy and transmission electron microscopy for statistical analysis of the positions of Au nanospheres and yields of assemblies.

3.2.5 Finite-difference time-domain (FDTD) simulations

Simulations of the optical properties of the Au nanospheres, Ag nanoplates, face-type $\mathbf{AB_2}$ trimers, and edge-type $\mathbf{AB_2}$ trimers were performed using FDTD solutions (Lumerical Solutions, Inc.). Perfectly matched layers were set as the boundary conditions. A 3D total-field scattered-field light source with wavelengths ranging from 400 nm to 1100 nm was introduced into a cuboid containing the target nanostructures. Because nanostructures in solvents are randomly oriented, different incident directions of the light source were considered in our calculations. Au nanospheres were treated as ideal spheres. Therefore, one incident direction and one polarization state were considered. For the Ag nanoplates and the face-type $\mathbf{AB_2}$ trimers, incident directions

parallel and perpendicular to the plane of the nanoplates were included in our calculations. Moreover, two orthogonal polarization states were considered in each incident direction to obtain unpolarized results. We then added up the extinction spectra from these two incident directions to produce the UV-vis extinction spectra of Ag nanoplates and the face-type **AB$_2$** trimers in solvents.

In the case of edge-type **AB$_2$** trimers, we modeled the systems with three incident directions, including the directions perpendicular to the nanoplate plane, and parallel and perpendicular to the major axis of the **AB$_2$** trimer, coplanar with the nanoplate. Two orthogonal polarization states were calculated in each incident direction as well. All of the extinction spectra from these three incident directions were added. In all cases, the background refractive index was set as 1.41. The Au nanosphere was 25 nm in diameter and the Ag nanoplate was 85 nm in diameter and 8 nm in thickness. Both the Au nanosphere and the Ag nanoplate were coated with 5-nm-thick solvated polymer shells whose refractive index was estimated to be 1.45. The gaps between the Ag nanoplate and the Au nanosphere were set as 8 nm for the face-type and the edge-type trimer. We imposed a uniform mesh grid on the target nanostructure. The maximum mesh step was set as 1 nm along all the directions. The permittivity of Au and Ag were adopted from the experimental data from Johnson and Christy,[175] and Palik,[176] respectively. All of the electric field profiles were calculated at the wavelength of the plasmon resonance.

3.2.6 Calculation and grafting-density

Thermogravimetric analysis (TGA) was performed to quantify the number of grafted polymers on NPs (**Figure 3.4**). Taking PS_{111}-*b*-$P(AA_{0.31}$-*r*-$St_{0.69})_{289}$ grafted Ag nanoplates as an example, a weight loss was observed at temperatures above 200 ℃,

due to the thermal degradation of copolymers into volatile products. Based on the measured weight loss *f*, the grafting density (σ, chains·nm^{-2}, listed in **Table 3.2**) of copolymers on Au nanospheres and Ag nanoplates was estimated by the respective equations:[123]

$$\sigma = \frac{f}{1-f} \cdot \frac{N_A \rho D}{6 M_n}, \tag{3.1}$$

and

$$\sigma = \frac{f}{1-f} \cdot \frac{N_A \rho D^2}{6 M_n h}, \tag{3.2}$$

where f is the weight fraction of the polymeric ligands determined by TGA, N_A is Avogadro's constant, ρ is the bulk density of NP's core material (19.32 g cm^{-3} for Au and 10.49 g cm^{-3} for Ag), D is the diameter of NPs, and M_n is the number-average molecular weight of the copolymer ligands. In the calculation, we assume that the density of the NPs is the same as that of the bulk material, and that no free polymer is present in the system. For example, the weight losses for PEO_{45}-*b*-$P(AA_{0.36}$-*r*-$St_{0.64})_{467}$-grafted Ag nanoplates (**Figure 3.4a**, red) and PEO_{45}-*b*-$P(DMAEMA_{0.41}$-*r*-$St_{0.59})_{158}$-grafted Au nanospheres (**Figure 3.4b**, black) were 8.4% and 4.3%, respectively. Following the equations, σ was calculated to be 0.45 chain/nm^2 and 0.11 chain/nm^2, respectively.

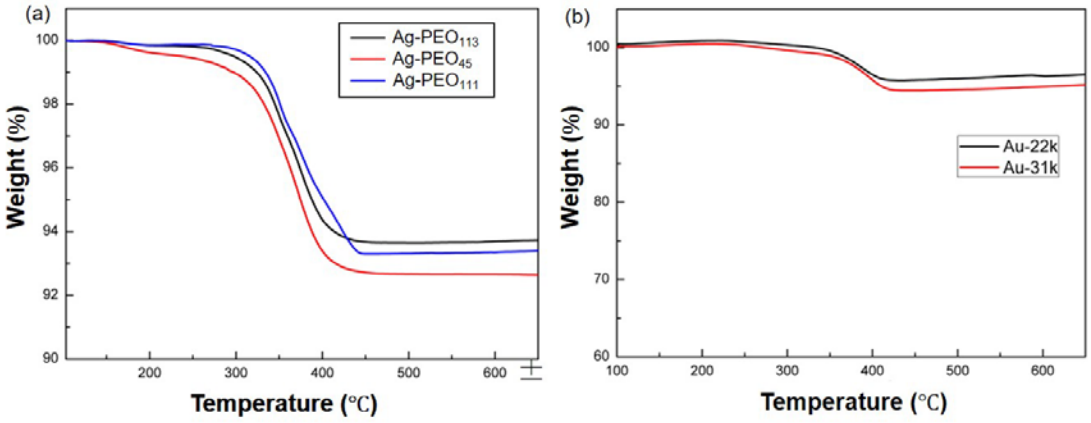

Figure 3.4 Representative TGA traces of (a) Ag nanoplates grafted with PEO_{113}-*b*-$P(AA_{0.26}$-*r*-$St_{0.74})_{249}$ (black), PEO_{45}-*b*-$P(AA_{0.36}$-*r*-$St_{0.64})_{467}$ (red), and PS_{111}-*b*-$P(AA_{0.31}$-*r*-$St_{0.69})_{289}$ (blue); (b) Au nanospheres grafted with PEO_{45}-*b*-$P(DMAEMA_{0.41}$-*r*-$St_{0.59})_{158}$ (black) and PEO_{45}-*b*-$P(DMAEMA_{0.30}$-*r*-$St_{0.70})_{244}$ (red).

From the calculated σ, the average distance (*d*) between anchoring points of adjacent ligands can be estimated by using equation:[123]

$$d = \frac{2}{\sqrt{\pi\sigma}} \cong \frac{1.1}{\sqrt{\sigma}}, \qquad (3.3)$$

where σ is estimated from TGA. The footprint of a single copolymer ligand on the NP surface is considered as a circular area with a diameter equal to *d*. The *d* values for Ag grafted with PEO_{45}-$P(A_{0.36}S_{0.64})_{467}$ and Au grafted with PEO_{45}-$P(D_{0.41}St_{0.59})_{158}$ were estimated to be 1.73 nm and 3.3 nm, respectively. The radius of gyration of the corresponding copolymer can be calculated from $R_g = (Nb^2/6)^{1/2}$ (see **Table 3.2**).[177] The ratio of R_g/d is estimated to be in the range of 1.6 to 2.0 for NP-**B**s and 4.0 to 5.0 for NP-**A**s, which suggests that the copolymer chains extended and stretched on both Au and Ag surfaces to adopt a polymer brush conformation.[178,179]

3.2.7 Sample preparation for characterizations

^{1}H NMR. ^{1}H NMR spectra were recorded using Bruker AV-400 MHz high resolution NMR spectrometer. All copolymers were dried under vacuum at 80 ℃ overnight to remove trace amounts of solvent. The NMR samples were prepared by dissolving polymers in deuterated reagents, either $CDCl_3$, THF-d_4 or DMSO-d_6.

Gel permeation chromatography (GPC). GPC measurements were performed on a Waters GPC-a (1515 HPLC pump and Waters 717 Plus autoinjector) equipped with a Varian 380-LC evaporative light-scattering detector and a Waters 2487 dual absorbance detector. PS standards were used for molecular weight and molecular weight distribution calibration, and THF was used as the elution solvent, with a flow rate of 2.0 mL·min^{-1}. The data were processed using Empower GPC software (Waters, Inc.).

Thermogravimetric Analysis (TGA). TGA was used to characterize the grafting density (σ) of copolymers on the surface of the Au and Ag NPs. A 5.0 mL stock solution of building blocks was centrifuged to remove the supernatant, hexane was subsequently added, and the sample was centrifuged until a pellet formed. The pellets were dried in vacuum oven for 24 h to remove the solvent residues before TGA measurement. The experiments were carried out under argon flow, with a scan rate of 25 ℃·min^{-1} from 25 ℃ to 600 ℃. Before the scan process, the temperature was maintained at 100 ℃ for 30 min to remove any residual moisture. The weight fraction of polymer ligands *f* was determined by using the TA Universal Analysis software package.

UV-vis absorption spectroscopy. Extinction spectra of samples was measured in a range of 400-1100 nm using a PERKIN LAMBDA 35 UV-vis system.

Electron microscopy. The morphologies of assemblies were obtained using a Hitachi SU-70 Schottky field-emission-gun scanning electron microscope (SEM) and a JEOL FEG transmission electron microscope (TEM). Samples for scanning and transmission electron microscopy analysis were prepared by depositing ~2 μL of solution on silicon wafer and 300 mesh copper grids covered with carbon film, respectively. The samples were dried at room temperature before imaging measurement.

3.3 Results and discussion

3.3.1 Self-assembly driven by reactive block copolymers

In this chapter, we demonstrate a polymer-shielding-mediated mechanism for programming the regioselective bonding of non-patchy plasmonic nanoplates (NP-**A**) and nanospheres (NP-**B**) into discrete clusters with defined geometry and NP orientation (**Figure 3.5**).

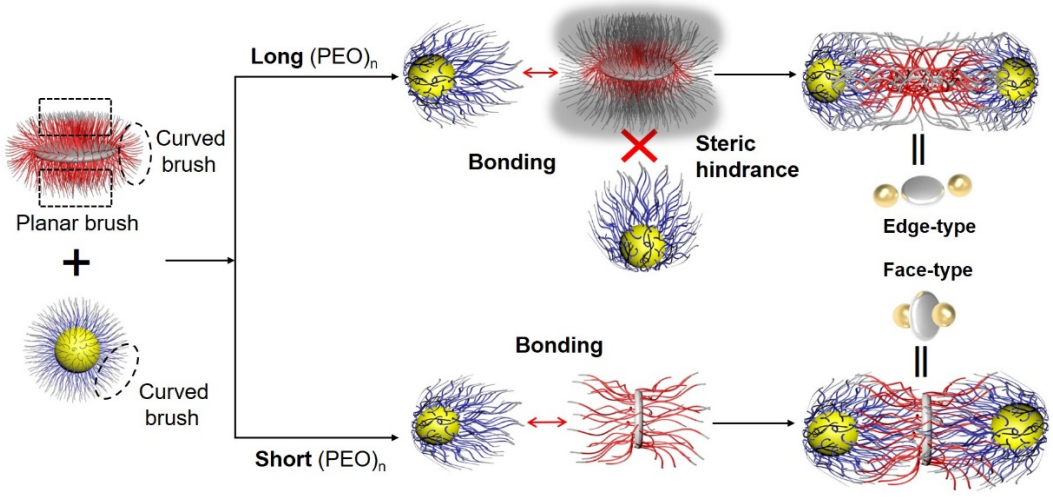

Figure 3.5 Schematic illustration of regioselective bonding of NP-**A**s and NP-**B**s into edge-type and face-type clusters mediated by the shielding effect of copolymer ligands.

We assumed that the surfaces of the binary NPs are uniformly grafted with block copolymer ligands in which the NP-adjacent reactive block carries complementary weak acid or base groups for bonding and the non-reactive block acts as stabilizers for the NPs (**Figure 3.6**). When NP-**A**s and NP-**B**s are mixed in solution, the neutralization reaction between end-tethered copolymer ligands triggers the directional bonding of dissimilar NPs to yield uniform clusters with $\mathbf{AB}_x$ structures (where x is the number of NP-**B**s in the cluster, $1 \leq x \leq 4$). The bonding number x of $\mathbf{AB}_x$ structures is dictated by the stoichiometry of acid/base groups on NP-**B**s and NP-**A** within a cluster. Depending on the length of the non-reactive block, the NP-**B**s preferentially attach to the edge or the face of a central NP-**A** to produce edge-type or face-type assemblies. The difference in bonding direction/position is ascribed to the different steric shielding effect between planar and curved polymer brushes on the disc-shaped NP-**A**.

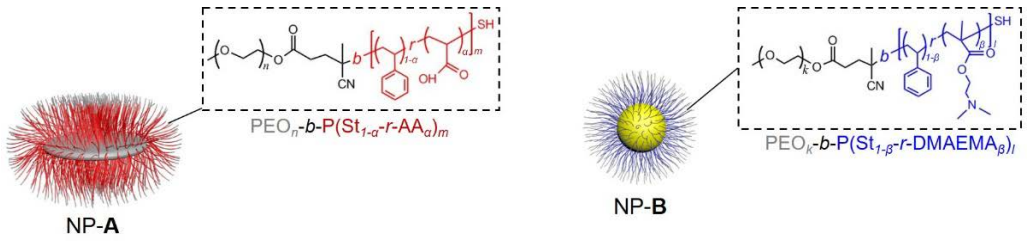

Figure 3.6 Schematic illustration of (a) a copolymer-grafted nanoplate (NP-**A**) and (b) a copolymer-grafted nanosphere (NP-**B**).

As a demonstration, we synthesized circular silver nanoplates[180] (diameter, D of 61 ± 9 nm) as NP-**A**s and Au nanospheres[174] (D = 28 ± 3 nm) as NP-**B**s using a seed-mediated growth method. The two types of NPs were modified with two distinct thiol-terminated block copolymers via ligand exchange method.[181, 182] Specifically, a copolymer of poly(ethylene oxide)$_n$-*b*-poly(acrylic acid$_\alpha$-*r*-styrene$_{1-\alpha}$)$_m$-SH [PEO$_n$-*b*-

P(AA_{α}-*r*-$St_{1-\alpha}$)$_m$] was used for the NP-**A**s, whereas a copolymer of poly(ethylene oxide)$_k$-*b*-poly(N,N-dimethylaminoethyl methacrylate$_{\beta}$-*r*-styrene$_{1-\beta}$)$_l$-SH [PEO_k-*b*-P($DMAEMA_{\beta}$-*r*-$St_{1-\beta}$)$_l$] was used for the NP-**B**s (**Figure 3.6** and **Table 3.1**). Here, *n*, *m*, *k*, and *l* denote the degree of polymerization of the corresponding blocks, whereas α and β represent the content (%) of each comonomer in the randomly-copolymerized blocks. In the copolymer ligands, the PEO block serves as a steric stabilizer for the NPs, whereas the random copolymerized block provides complementary reactive groups to trigger NP assembly. The copolymer-grafted NP-**A**s and NP-**B**s were dispersed in tetrahydrofuran (THF), a good solvent for the copolymer ligands.

3.3.2 Mechanism of regioselective bonding

The grafting density (σ) of copolymers on NPs was estimated to be ~0.4 chains·nm^{-2} for NP-**A**s and ~0.1 chains·nm^{-2} for NP-**B**s (**Table 3.2**). In THF, a good solvent of the copolymers, the ligands adopted a brush conformation on the surface of NPs, as indicated by $R_g/d \geq 4.0$ for nanoplates and $R_g/d \geq 1.6$ for nanospheres, where *d* is the average anchoring distance between adjacent polymer chains and R_g is the radius of gyration of an unperturbed copolymer chains.[178,179,183] The conformations of end-grafted copolymers on the disc-shaped NP-**A** exhibited two physically different states: (i) a planar brush on each flat face, and (ii) a convex curved brush at the edge of the disc. Based on the blob model of polymer chains, the blob size of a planar brush is constant from the chain end adjacent to the NP surface to the tip of the brush.[179] In contrast, the blob size of curved brushes increases as the distance from the convex surface increases, thus providing more space for the interpenetration of copolymer brushes from interacting NPs.[183,184]

Besides the grafting density of copolymer ligands, the conformation of polymer brushes may be affected by the quality of solvents, the chemical composition of polymers, and osmotic pressure (which is a negligible factor in this system). In our experiments, the copolymers were dissolved in good solvents (*i.e.,* THF and DMF) in surface-modification and self-assembly process to maintain the stretched chain conformation within the polymer brushes. The chemical composition of steric blocks may affect the conformation of polymer brushes by interactions like hydrogen bonds. In the model system, we used PEO (n=113) as steric blocks for shielding the face-type bonding and producing edge-type assemblies. To demonstrate that the regioselectivity of NP bonding originates from the steric shielding effect of the non-reactive polymer segments, rather than from the chemical composition of copolymer ligands, the PEO block was replaced by a steric polystyrene (PS) block of comparable length (n=111) in section **3.3.3**.

Table 3.2 Key parameters of NP-**A**(**B**) with copolymer ligands after surface modification*

NP-A/NP-B	f (%)	σ (chains·nm^{-2})	d (nm)	R_g (nm)	R_g/d
Ag-PEO$_{45}$-P(A$_{0.36}$S$_{0.64}$)$_{467}$	8.6	0.45	1.7	8.8	5.1
Ag-PEO$_{113}$-P(A$_{0.26}$S$_{0.74}$)$_{249}$	6.3	0.46	1.7	7.2	4.2
Ag-PS$_{111}$-P(A$_{0.31}$S$_{0.69}$)$_{289}$	6.4	0.39	1.9	8.0	4.2
Au-PEO$_{45}$-P(D$_{0.41}$St$_{0.59}$)$_{158}$	4.3	0.11	3.3	5.7	1.7
Au-PEO$_{45}$-P(D$_{0.30}$St$_{0.70}$)$_{244}$	5.6	0.10	3.5	7.0	2.0

* f (%) is the weight fraction of copolymer ligands measured by thermogravimetric analysis (TGA); Grafting density, σ (chains·nm^{-2}), and average anchoring distance between adjacent chains, d (nm), were calculated and estimated in SI; The radius of gyration, R_g (nm), was calculated from $R_g = N^{0.5}b/6^{0.5}$, where b is the Kuhn length (b = 1.8 nm for PS, b = 1.1 nm for PEO) and N is the number of Kuhn segments calculated the molar mass of Kuhn monomer M_0 (M_0 = 720 g/mol for PS and M_0 = *137* g/mol for PEO).

When NP-**A**s and NP-**B**s in THF were mixed with predetermined feeding-number ratios, $\psi_{B/A}$ of NP-**B**s to NP-**A**s, the neutralization reaction between acid/base groups of the end-grafted copolymers triggered the directional bonding of NP-**B**s to NP-**A**s to form stable clusters. In this process, NP-**A**s and NP-**B**s bonded in two distinctive modes, edge-type and face-type, depending on the length of PEO block of the copolymer ligands on the surface of disc-shaped NP-**A**s (**Figure 3.2**).

3.3.3 Edge-type bonding and nanoclusters

When n of PEO$_n$-*b*-P(AA$_\alpha$-*r*-St$_{1-\alpha}$)$_m$ ligands on NP-**A**s is large (n > 100, *e.g.*, n = 113), the steric effect of the long, non-reactive PEO blocks of the planar copolymer brushes on the flat top/bottom faces of the NP-**A**s shields the reactive block adjacent to the NP surface from reacting with the copolymers on the NP-**B**s. Spherical NP-**B**s, thus, prefer to attack the NP-**A**s from the edge, where the polymeric segments are less crowded, as indicated by larger blob size of curved brushes than that of planar brushes. As a result, the assembly process produces edge-type clusters with NP-**B**s arranged at the edge of a central NP-**A** (**Figure 3.7**).

The control over the coordination number x in **AB**$_x$ clusters was achieved by varying the number ratio, $Z_{A/B}$ of acid groups on a single NP-**A** to base groups on a single NP-**B**, and $\psi_{B/A}$. The $Z_{A/B}$ can be expressed as:

$$Z_{A/B} = \frac{\alpha \cdot m}{\beta \cdot l} \cdot \frac{\sigma_A}{\sigma_B} \cdot \frac{h \cdot D_A}{{D_B}^2}, \tag{3.4}$$

where the subscripts A and B represent NP-**A**s and NP-**B**s, respectively, and αm, βl and h are the number of acid groups of a PEO$_n$-*b*-P(AA$_\alpha$-*r*-St$_{1-\alpha}$)$_m$ chain, the number of base groups of a PEO$_k$-*b*-P(DMAEMA$_\beta$-*r*-St$_{1-\beta}$)$_l$ chain, and the thickness of disc-shaped NP-

As, respectively. In experiments, we tuned the values of $Z_{A/B}$ by varying βl of PEO-*b*-P(DMAEMA-*r*-St) copolymers on NP-**B**s, while keeping αm of PEO-*b*-P(AA-*r*-St) copolymers on NP-**A**s constant. As βl decreased from 168 to 31 ($Z_{A/B}$ increased from 1.05 to 4.76), the value of *x* increased from 1 to 4, because more NP-**B**s were needed to provide base groups for reacting with the acid groups on the central NP-**A** in a cluster. At βl = 168 ($Z_{A/B}$ = 1.05) and $\psi_{B/A}$ = ~1:1, the NPs assembled into **AB** clusters (**Figure 3.7a**). At a reduced βl of 73 ($Z_{A/B}$ = 2.42), a ~2:1 and ~3:1 of $\psi_{B/A}$ yielded $\mathbf{AB_2}$ and $\mathbf{AB_3}$ clusters as major products, respectively (**Figure 3.7b, c**). A high yield of $\mathbf{AB_4}$ clusters was obtained at βl =31 ($Z_{A/B}$ = 4.76) and $\psi_{B/A}$ = ~4:1 (**Figure 3.7d**). The heterogeneous structures of $\mathbf{AB_x}$ clusters were confirmed by element mapping under scanning transmission electron microscopy (STEM) mode (**Figure 3.8**).

The assembly strategy showed high-yield generation of edge-type $\mathbf{AB_x}$ clusters ($2 \leq x \leq 4$), which we ascribe to the reaction stoichiometry-driven bonding mechanism and the steric constrains of the inert PEO blocks. Without any further purification, the yields of edge-type $\mathbf{AB_2}$, $\mathbf{AB_3}$, and $\mathbf{AB_4}$ structures were 69%, 72% and 59%, respectively (**Figure 3.9**). The assembly strategy exhibited high regioselectivity in positioning the NP-**B**s at the edge rather than the faces of a central NP-**A**. Over 90% NP-**B**s in $\mathbf{AB_x}$ structures were bonded to the edge of a NP-**A** (**Figure 3.10**). The $\mathbf{AB_x}$ structures showed symmetric arrangements of NP-**B**s around the central NP-**A**. The average bond angles between NP-**A** and NP-**B**s in the clusters were 160 ± 20°, 121 ± 17°, and 91 ± 12° for $\mathbf{AB_2}$, $\mathbf{AB_3}$, and $\mathbf{AB_4}$, respectively (**Figure 3.11**). The regioselectivity of NP bonding originates from the steric shielding effect of the non-reactive polymer segments, rather than from the chemical composition of copolymer

ligands. When the PEO block was replaced by a non-reactive polystyrene block of comparable length, small clusters with 90% edge-type bonding were also generated.

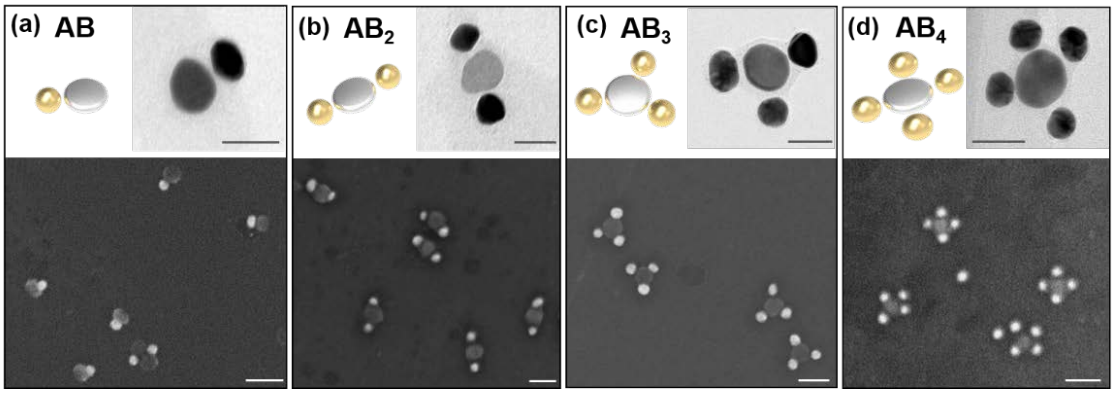

Figure 3.7 Schemes, TEMs and SEMs of edge-type NP clusters with different configurations: (a) **AB**, (b) **AB$_2$**, (c) **AB$_3$**, and (d) **AB$_4$**. **NP-A**s: PEO$_{113}$-*b*-P(AA$_{0.26}$-*r*-St$_{0.74}$)$_{249}$-grafted Ag nanoplates; **NP-B**s: Au nanospheres grafted with (a) PEO$_{45}$-*b*-P(DMAEMA$_{0.40}$-*r*-St$_{0.60}$)$_{419}$, (b, c) PEO$_{45}$-*b*-P(DMAEMA$_{0.30}$-*r*-St$_{0.70}$)$_{244}$, and (d) PEO$_{45}$-*b*-P(DMAEMA$_{0.32}$-*r*-St$_{0.68}$)$_{98}$ copolymers. $\psi_{B/A}$: 1:1 (a), 2:1 (b), 3:1 (c) and 4:1 (d). Au is brighter than Ag under SEM, while darker under TEM. Scale bars: 50 nm.

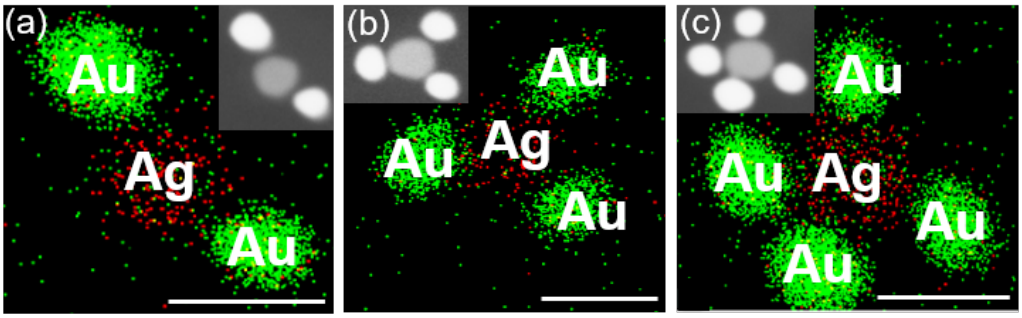

Figure 3.8 Energy-dispersive X-ray (EDX) elemental mapping and high-angle annular dark field (HAADF) transmission electron micrographs (TEMs, insets) of edge-type (a) **AB$_2$** and (b) **AB$_3$**.

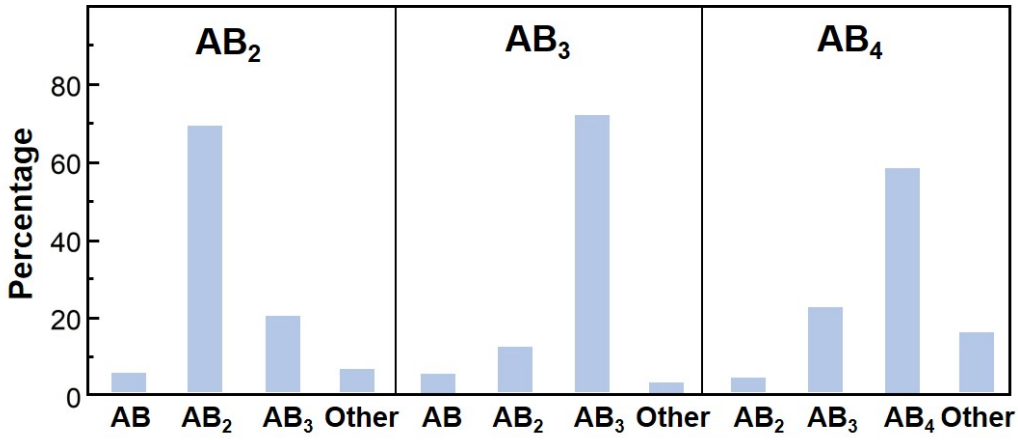

Figure 3.9 Distribution of edge-type $\mathbf{AB_x}$ clusters. Over 500 clusters were analyzed for each plot.

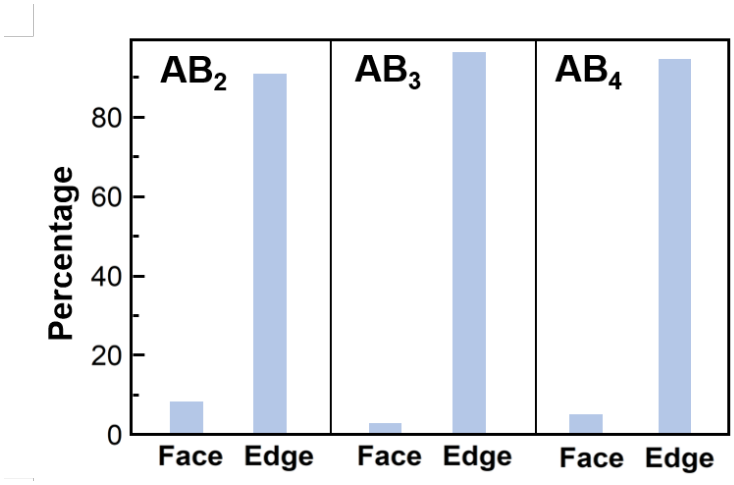

Figure 3.10 Distribution of bonding modes in edge-type $\mathbf{AB_x}$ clusters. Over 500 clusters were analyzed for each plot.

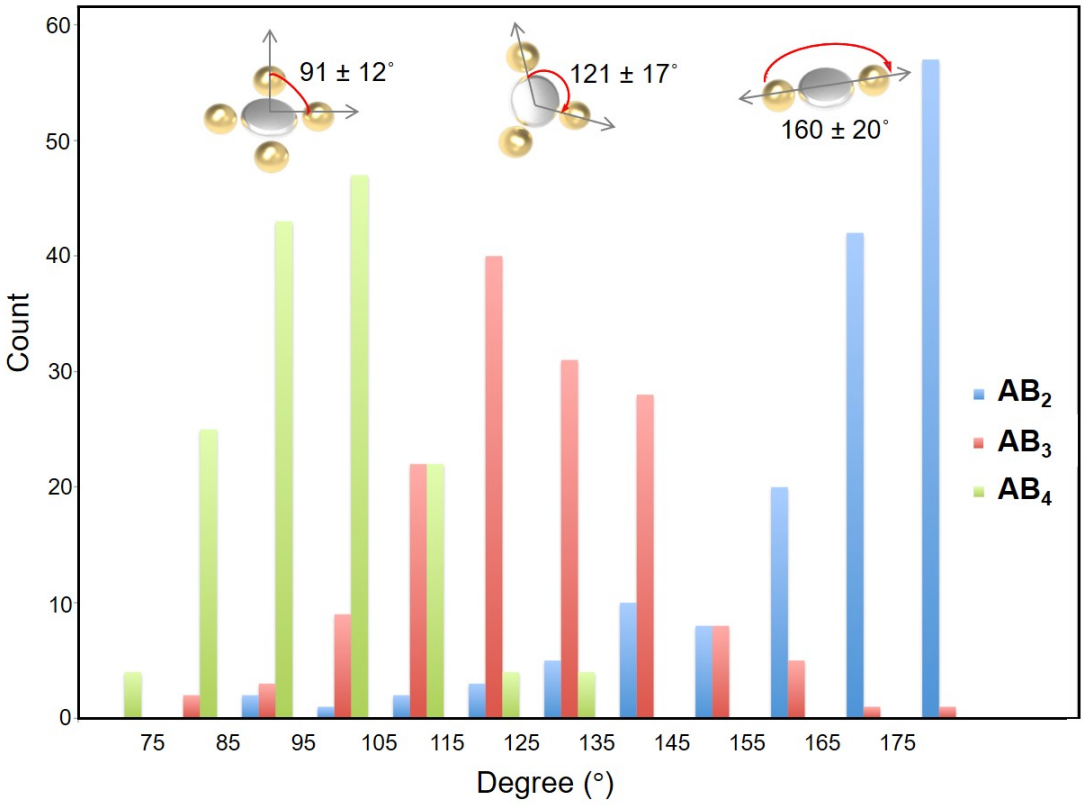

Figure 3.11 Distribution of the B-A-B angle in edge-type **AB2**, **AB3**, and **AB4** structures.

3.3.4 Face-type bonding and nanoclusters

At n = 45 for PEO_n-b-$P(AA_\alpha$-r-$St_{1-\alpha})_m$ ligands on NP-**A**s, the steric shielding of short PEO blocks is negligible. The carboxyl groups of NP-adjacent block of planar brushes on the faces of a NP-**A** can be readily accessed by the base groups of copolymer ligands on a NP-**B**. Thus, the acid-base neutralization reaction leads to the bonding of NP-**B**s onto the top and bottom faces of a central disc-shaped NP-**A** to form face-type **AB2** structures (**Figure 3.12a**). In this arrangement, the conformal contact and extent of reaction of copolymer ligands on both NP-**A** and NP-**B** can be maximized, thus minimizing the overall energy of the assembly system. When NP-**A**s and NP-**B**s are

grafted with PEO_{45}-*b*-$P(AA_{0.32}$-*r*-$St_{0.68})_{335}$ and PEO_{45}-*b*-$P(DMAEMA_{0.40}$-*r*-$St_{0.60})_{419}$ copolymers, their assembly produces face-type **AB_2** trimers with one NP-**A** sandwiched between two NP-**B**s. The yield of **AB_2** clusters was 75%, and over 80% of the NP-**B**s were bonded to the faces of NP-**A**s (**Figure 3.12d**). When αm of PEO-*b*-P(AA-*r*-St) copolymers on NP-**A**s decreased from 107 to 56 and $\psi_{B/A}$ decreased from ~2:1 to ~1:1, the assembly process produced linear chains with alternating sequence of NP-**A**s and NP-**B**s (**Figure 3.12b**). We attribute the formation of alternating chains, rather than discrete **AB** dimers, to the fact that short PEO-*b*-P(AA-*r*-St) copolymers on the flat faces of NP-**A**s can only react and consume base groups on one side of NP-**B**s, thus leaving base groups on the other side to further react with another NP-**A**s. The face-type **AB_2** structure was confirmed by element mapping under STEM mode (**Figure 3.12c**).

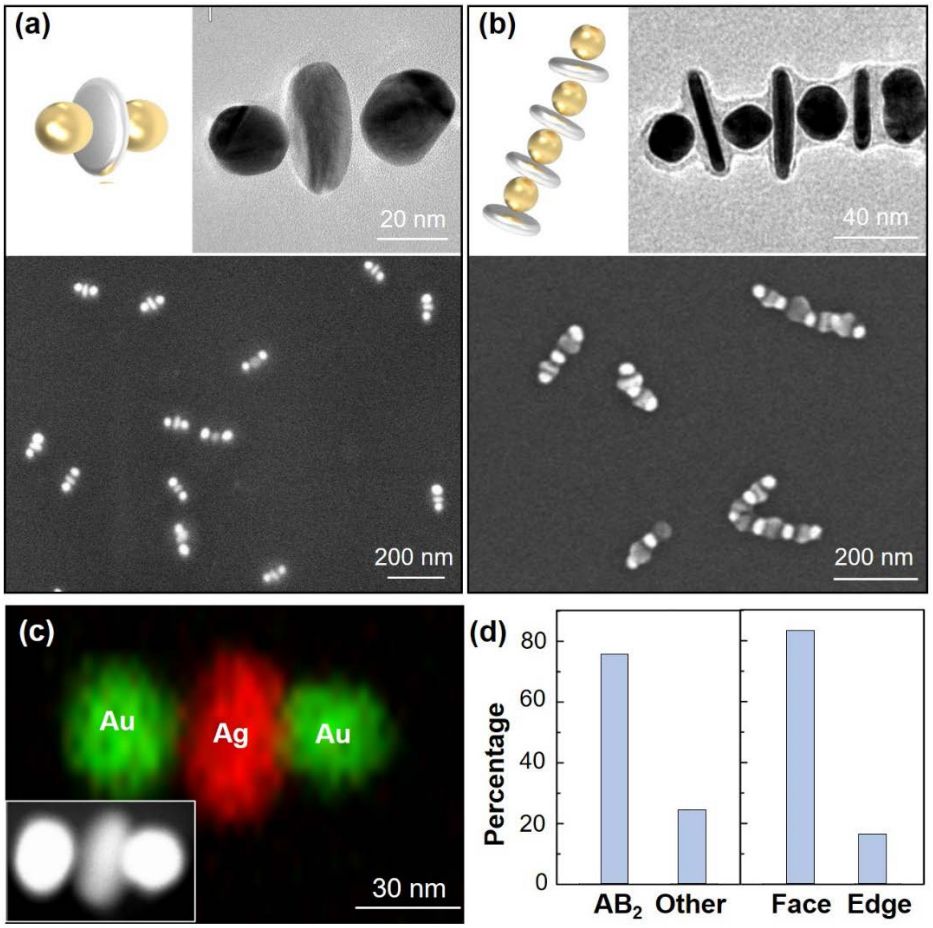

Figure 3.12 Schemes, TEMs and SEMs of (a) face-type **AB$_2$** structures and (b) alternating chains. NP-**B**s: PEO_{45}-*b*-$P(DMAEMA_{0.40}$-*r*-$St_{0.60})_{419}$-tethered Au nanospheres; NP-**A**s: Ag nanoplates grafted with (a) PEO_{45}-*b*-$P(AA_{0.32}$-*r*-$St_{0.68})_{335}$ and (b) PEO_{45}-*b*-$P(AA_{0.30}$-*r*-$St_{0.70})_{185}$ copolymers. (c) EDX elemental mapping and HAADF TEM image (inset) of a face-type **AB$_2$** structure. (d) Yield (left) and bonding mode (right) of clusters in (a). Over 500 clusters were analyzed for each plot in (d).

3.3.5 Regioselective self-assembly with triangular nanoplates

Regioselective assembly is applicable to the directional bonding of spherical NPs with other shaped nanoplates. Silver triangular nanoplates (edge length: 87 ± 10 nm)

were grafted with PEO_n-*b*-$P(AA_\alpha$-*r*-$St_{1-\alpha})_m$ copolymer ligands for use as NP-**A**s. Their assembly with NP-**B**s produced both edge-type and face-type $\mathbf{AB}_x$ clusters, following the same assembly principle as circular nanoplates. At n = 113, the long PEO blocks shielded the acid groups on the flat faces of the NP-**A**s from reacting with the base groups on the NP-**B**s, thus producing edge-type clusters, *e.g.*, $\mathbf{AB_2}$ structures (**Figure 3.13a**). The yield of edge-type bonding was ~90% (**Figure 3.14**). At n = 45, the assembly produced face-type $\mathbf{AB_2}$ clusters and alternating chains (**Figure 3.13b, c**), with 80% and 86% yield of face-type NP arrangements, respectively (**Figure 3.14**).

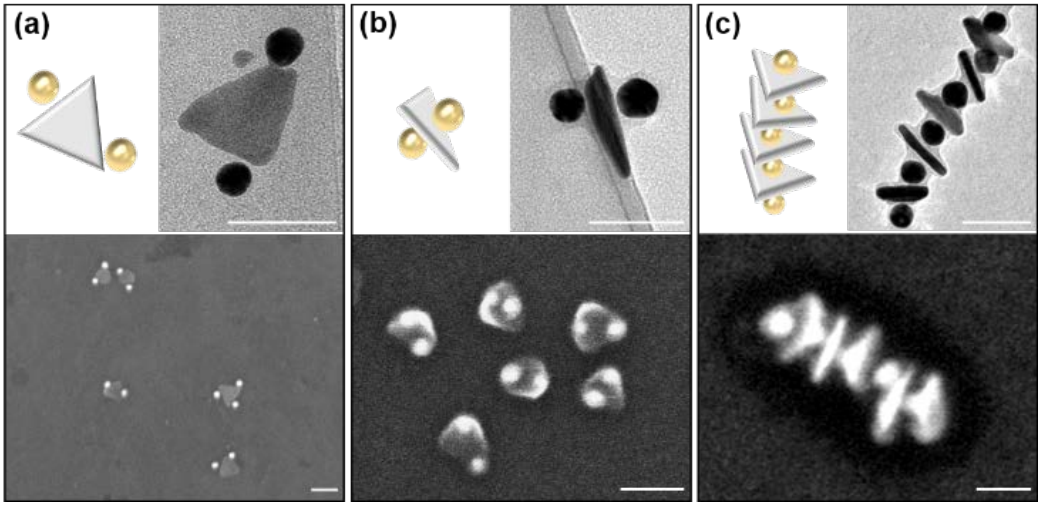

Figure 3.13 (a-c) Schemes, TEMs, and SEMs of (a) edge-type $\mathbf{AB_2}$ trimers, (b) face-type $\mathbf{AB_2}$ trimers, and (c) alternating chains. NP-**B**s: PEO_{45}-*b*-$P(DMAEMA_{0.40}$-*r*-$St_{0.60})_{419}$-grafted Au nanospheres; NP-**A**s: Ag nanoplates tethered with (a) PEO_{113}-*b*-$P(AA_{0.26}$-*r*-$St_{0.74})_{249}$, (b) PEO_{45}-*b*-$P(AA_{0.32}$-*r*-$St_{0.68})_{335}$, and (c) PEO_{45}-*b*-$P(AA_{0.30}$-*r*-$St_{0.70})_{185}$ copolymers. Scale bar: 100 nm.

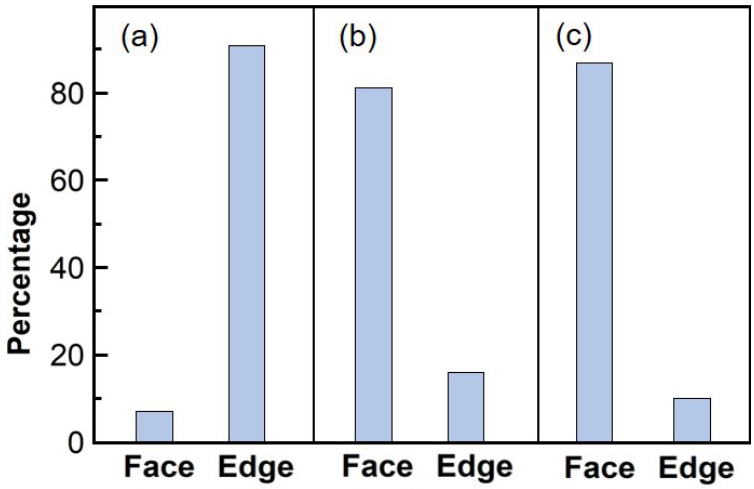

Figure 3.14 Distribution of bonding modes with central triangular NP-**A**s in (a) edge-type **AB**$_3$ clusters, (b) face-type **AB**$_2$ clusters, and (c) alternating chains.

3.3.6 Experimental and computational studies on optical properties

We investigated the optical properties of discrete edge-type and face-type **AB**$_2$ trimeric structures assembled from NP-**A**s (D = 83.8 ± 8.0 nm) and NP-**B**s (D = 27.5 ± 3.9 nm). In experiments, the bonding of two NP-**B**s with a NP-**A** in **AB**$_2$ clusters led to a redshift in the localized surface plasmonic resonance (LSPR) bands. The strength of redshift was dependent on the relative orientation of NPs. The longitudinal LSPR band of face-type **AB**$_2$ clusters was located at 847 nm, whereas the peak was at 842 nm for edge-type trimers (**Figure 3.15**). The NP orientation-dependent redshift in the longitudinal LSPR band was confirmed by finite-difference time-domain (FDTD) simulations. When the NP-**B**s were arranged at the face of a NP-A in **AB**$_2$ structures, the LSPR band shifted from 827 nm (the in-plane mode of pristine NP-**A**s) to 840 nm (**Figure 3.16**). In contrast, the edge-type **AB**$_2$ structures displayed a longitudinal LSPR peak at 836 nm.

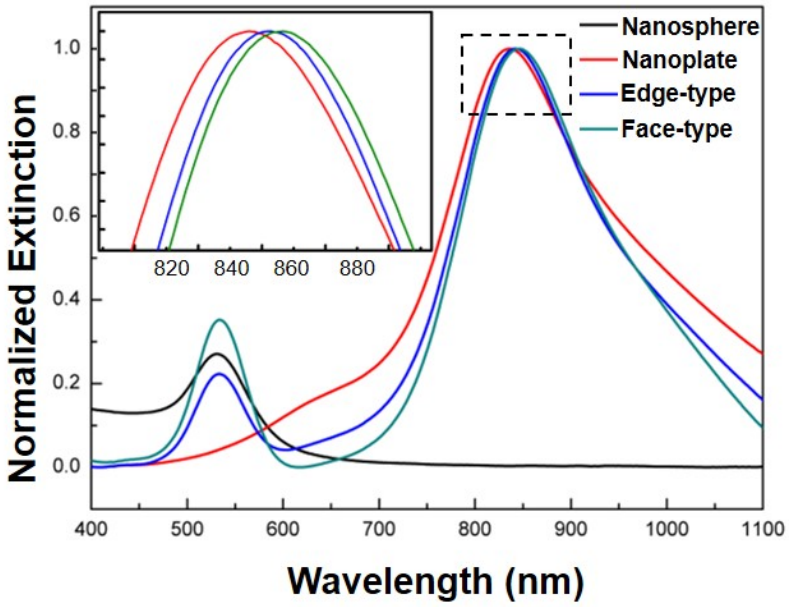

Figure 3.15 Experimental extinction spectra for polymer-grafted Au nanospheres (black), Ag nanoplates (red), edge-type (blue), and face-type trimers (olive).

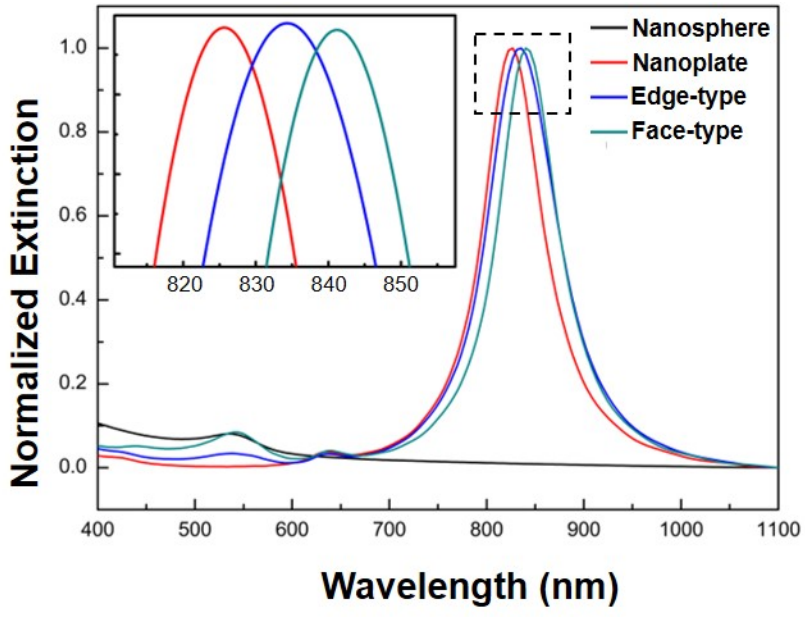

Figure 3.16 Simulated extinction spectra for polymer-grafted Au nanospheres (black), Ag nanoplates (red), edge-type (blue), and face-type trimers (olive).

To investigate the origin of the arrangement-dependent plasmonic coupling, we calculated the polarization spectra of Ag nanoplates (**Figure 3.17**), edge-type trimers (**Figure 3.18**), and face-type trimers (**Figure 3.19**) with different light incident directions: the *x*, *y*, and *z* axes. In all polarization spectra, the out-of-plane mode (polarizations along *z* axis) made a minimal contribution to the overall extinction spectra. The major difference in the optical response between the two types of $\mathbf{AB_2}$ trimers originated from different contributions of polarizations along the *x* and *y* axes (in-plane mode) of the trimers. For the face-type trimer, the peak for polarizations both along *x* and *y* axes was at 840 nm, and the overall extinction has a peak at the same wavelength (**Figure 3.19**). In contrast, the overall extinction spectrum of the edge-type trimer was the sum of spectra with polarizations along *x* and *y* axes that had maxima at different wavelengths (**Figure 3.18**).

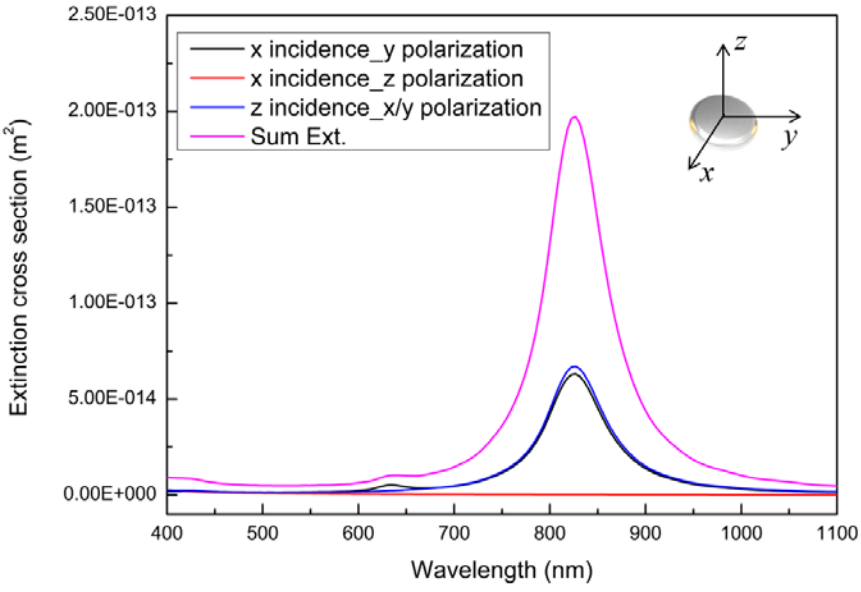

Figure 3.17 Calculated extinction spectra of polymer shell-coated Ag nanoplate in THF. The overall simulated extinction spectrum (magenta curve) was obtained by summing the spectra from all contributing incident directions and polarization states.

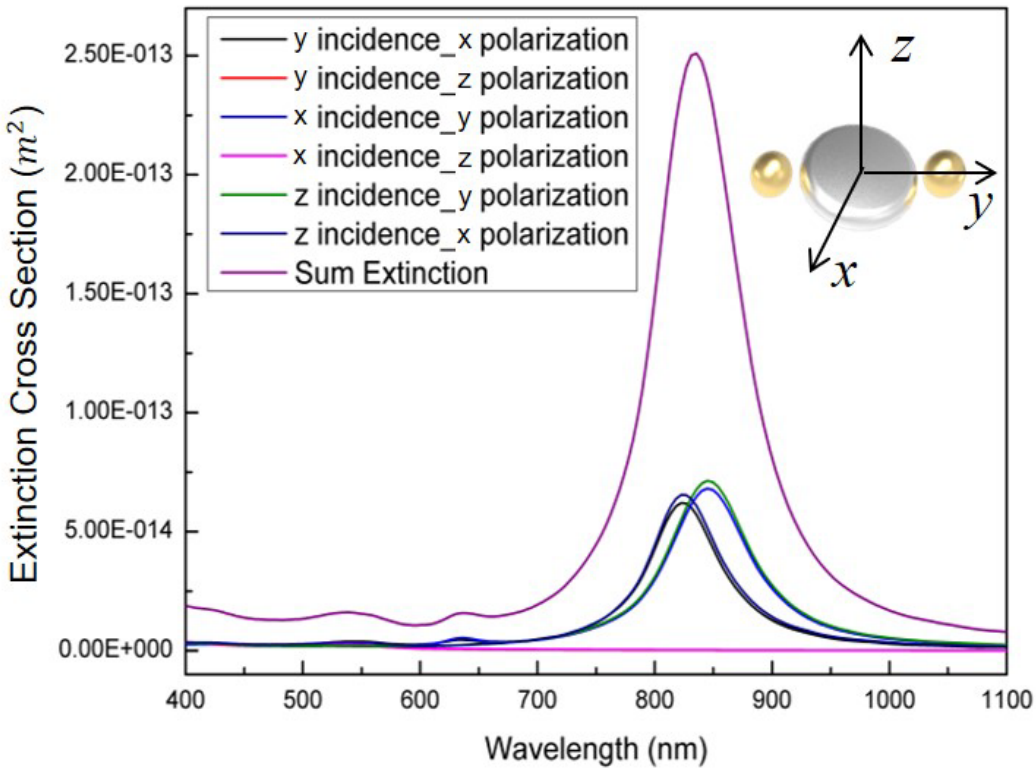

Figure 3.18 Calculated extinction spectra of edge-type **AB_2** trimers in different polarization and light incidence directions, and the overall simulated extinction spectrum obtained from the addition of the all spectra from all contributing incident directions and polarization states. For the edge-type trimer, the overall extinction spectrum was the sum of spectra at two polarizations, along *x* and *y* axes, with maxima at different wavelengths, 827 nm and 845 nm, respectively. The overall extinction shows a peak at 836 nm.

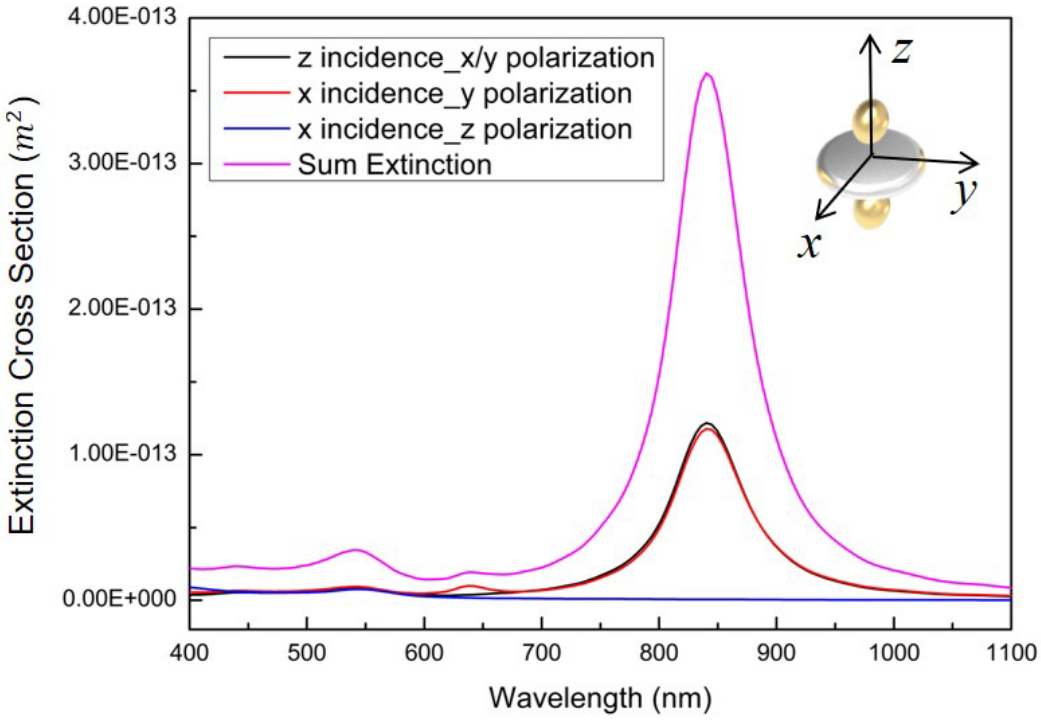

Figure 3.19 Calculated extinction spectra of face-type **AB_2** trimers in different polarization and light incidence directions, and the overall simulated extinction spectrum obtained from the addition of the all spectra from all contributing incident directions and polarization states. For the face-type trimer, the maxima for polarizations along both the *x* and *y* axes were at 840 nm, and the overall extinction therefore exhibits a peak at the same wavelength.

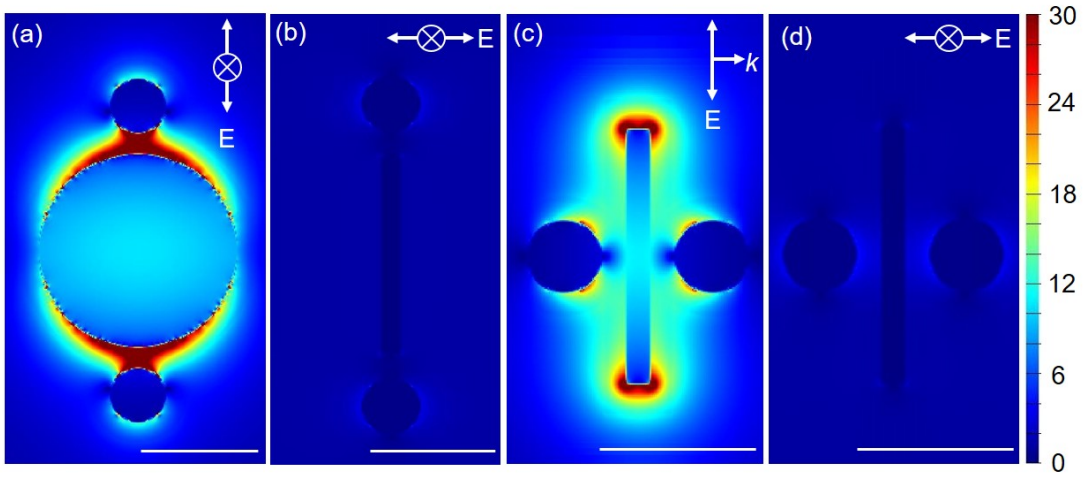

Figure 3.20 Electric-field intensity enhancement contours of (a, b) edge-type trimers and (c, d) face-type trimers with different electric field polarizations. The incident light is (c, e) perpendicular and (d, f) parallel to the plane of nanoplate. Scale bars: 50 nm.

Both edge-type and face-type trimers exhibit a more significant electric-field enhancement at the surface of Ag when the polarization direction is parallel to the plane of the nanoplate (**Figure 3.20a, c**), rather than perpendicular to the plane (**Figure 3.20b, d**). Notably, the edge-type **AB_2** shows stronger overall electric-field enhancement than does the face-type trimer under the same polarization mode.

3.4 Conclusion

In summary, we have developed a strategy to control the regioselective bonding of plasmonic NPs with distinct shapes to generate discrete nanoclusters. The self-assembly is driven the acid-base reaction of reactive groups of block copolymer ligands on Ag nanoplates and Au nanospheres. The arrangement of nanospheres around a nanoplate in the clusters can be modulated by tuning the steric shielding effect of copolymer ligands on the surface of nanoplates. The number of nanopsheres in one

nanoplate-centered cluster is governed by the stoichiometry of the acid-base reaction, which can be tuned by feeding ratios of NPs, grafting density of copolymer ligands, and the chemical composition of reactive blocks of copolymers.

This strategy does not require site-specific surface modification of NPs and allows assembly of NPs into clusters with high yield and regioselectivity. The different arrangements of NPs in clusters resulted in distinctive optical properties of assemblies due to different coupling modes of Au nanospheres and Ag nanoplates. This work offers great opportunities for designing functional complex nanostructures for different applications.

Chapter 4: Regioselective self-assembly of plasmonic nanoflowers and nanobuds

Overview: Controllable organization of plasmonic nanoparticles into uniform and well-defined nanoclusters is highly desirable for tailoring interparticle plasmonic coupling and electric field confinement. However, many previous reports were limited to top-down methods or random clustering of spherical nanoparticles. This chapter demonstrates the self-assembly of plasmonic nanoflowers and nanobuds via polymeric-ligand-mediated regioselective bonding. These assemblies feature a fixed number of particles in a controlled spatial arrangement of Au nanospheres and Ag nanoplates. Nanoflowers and nanobuds with the same number of petals exhibit localized surface plasmon resonance (LSPR) maxima at different wavelengths and have different electric-field enhancements. This study demonstrates the feasibility of constructing complex plasmonic nanostructures using polymeric ligand-mediated self-assembly and offers great opportunities for designing functional nanostructures with high structural complexity for diverse applications.

This chapter is adapted from a manuscript to be submitted: Lin, X.; Ye, S.; Kong, C.; Webb, K.; Zhang, Q.; Fourkas, J. T.; Nie, Z. Regioselective self-assembly of plasmonic nanoflowers and nanobuds.
L. X. and N. Z. conceived and designed the experiments; L. X. performed most of experiments; Y. S. performed the simulations of optical properties; W. K. contributed in the synthesis of polymers and discussion of self-assembly; K. C. and Z. Q. helped on electron microscopy and contributed in discussions. L. X. wrote the manuscript with revisions from F. J. T., and N. Z.

4.1 Introduction

Assembling plasmonic nanoparticles into well-defined clusters is important for tailoring plasmonic coupling and optical properties, allowing for applications in sensing, surface-enhanced spectroscopies, and nonlinear optics.[185-190] Considerable effort has been put into developing precise assembly techniques, as the coupling modes and strengths of NPs are dictated by the number, interparticle distance, and spatial arrangements of NPs in the clusters.[48,191-194] However, most approaches for the formation of nanoclusters are limited to single or homogeneous building blocks, with little control over spatial arrangements within the clusters.

In this chapter, we utilize the polymeric ligand-mediated regioselective bonding described in Chapter 3 to construct well-defined plasmonic nanoclusters, nanoflowers and nanobuds, composed of Ag nanoplates and Au nanospheres. The stoichiometry of reactive groups on the polymeric ligands governs the number of particles in one cluster, and the regioselective bonding enables precise control over the spatial orientations of building blocks. Nanoflowers and nanobuds with the same number of “petals” exhibit distinct plasmonic coupling modes and electric-field enhancements. This study demonstrates the feasibility of constructing complex plasmonic nanostructure by polymeric ligand-mediated self-assembly and offers great opportunities for designing functional nanostructures with high structural complexity for diverse applications.

4.2 Experiments

4.2.1 Materials

Gold (III) chloride trihydrate ($HAuCl_4 \cdot 3H_2O$, ≥ 99.9% trace metals basis), sodium citrate tribasic dihydrate (≥ 99%), silver nitrate ($AgNO_3$), L-ascorbic acid, tetrahydrofuran (THF), N, N-dimethylformamide (DMF), and dimethyl sulfoxide (DMSO) were purchased from Sigma-Aldrich and were used as received. Styrene (St) and N,N-dimethylaminoethyl methacrylate (DMAEMA) were passed through an Al_2O_3 column to remove inhibitors. Acrylic acid (AA) was distilled under vacuum before use and stored in freezer at -20 ℃. Azobis(isobutyronitrile) (AIBN) was recrystallized twice from ethanol. PEO_{45}-CTA, was synthesized by coupling poly(ethylene oxide) methyl ether (PEG_{45}-OH, and PEG_{113}-OH, with molecular weights of 2 $Kg \cdot mol^{-1}$ and 5 $Kg \cdot mol^{-1}$, respectively) with 4-cyano-4-(phenylcarbonothioylthio)pentanoic acid (CPPA) through esterification. Deionized water (Millipore Milli-Q grade) with a resistivity of 18.0 MΩ was used in all the experiments.

4.2.2 Preparation of building blocks

Au nanospheres and Ag nanoplates were synthesized by the seed-growth methods described in Chapter 3.2.2 and Chapter 2.2.2, respectively.

Thiol-terminated *di*-block copolymers were synthesized by reversible addition fragmentation chain-transfer (RAFT) polymerization, as described in Chapter 3.2.3. The synthetic routes are shown in Figure 3.2 and details of copolymers are listed in Table 3.1. Surface modification of nanoparticles followed the same method as described in Chapter 3.2.4.

4.2.3 Self-assembly of nanoflowers and nanobuds

The assembly of nanoclusters was triggered by mixing the binary building blocks in THF at predetermined concentrations, as described in Chapter 3.2.4. For edge-type **BA$_x$** clusters (nanoflowers), the feeding ratios of NP-**A** to NP-**B** ($\psi_{A/B}$) were set to be equal or very close to the target *x* values: $\psi_{A/B}$ was set to 1:1, 2:1, 3:1, and 4:1 for edge-type **BA**, **BA$_2$**, **BA$_3$**, and **BA$_4$** clusters. respectively.

For face-type **BA$_x$** clusters (nanobuds), $\psi_{A/B}$ was set to be larger than the target *x* values with excessive NP-**A**s: 1.2:1, 2.5:1, 3.5:1, and 4.2:1 for face-type **BA**, **BA$_2$**, **BA$_3$**, and **BA$_4$** clusters. respectively.

4.2.4 Finite-difference time-domain (FDTD) simulations

Simulations of the optical properties of the AgNPs, f-**BA**, f-**BA$_2$**, e-**BA**, and e-**BA$_2$** clusters were performed by FDTD solutions (Lumerical Solutions, Inc.). Perfectly matched layers were set as the boundary conditions. A 3D total-field scattered-field light source was introduced into a cuboid containing the target nanostructures with the wavelength ranging from 400 nm to 1100 nm. Different incident directions of the light source were considered in our calculations to account for the random orientations of nanostructures in solution. For AgNPs, f-**BA**, and f-**BA$_2$**, incident directions parallel and perpendicular to the plane of the nanoplates were included in the calculations, respectively. Moreover, two orthogonal polarization states were calculated in each incident direction to obtain unpolarized results. The extinction spectra from these two incident directions were summed to produce the UV-vis extinction spectra of AgNPs and the face-type nanoclusters in solvents.

For e-**BA** and e-**BA$_2$**, three incident directions were calculated, including the

directions perpendicular to the nanoplate plane, parallel and perpendicular to the major axis of the e-**BA$_2$** trimer, coplanar with the nanoplate. Two orthogonal polarization states were calculated in each incident direction as well. All of the extinction spectra from these three incident directions were summed.

In all cases, the background refractive index was set to 1.41. The Au nanosphere was 38 nm in diameter and the Ag nanoplate was 51 nm in diameter and 8 nm in thickness. Both the Au nanosphere and the Ag nanoplate were coated with 5-nm-thick solvated polymer shells whose refractive index was taken to be 1.45. The gaps between the Ag nanoplate and the Au nanosphere were set as 6 nm for both face-type and edge-type nanoclusters. A uniform mesh grid was imposed on the target nanostructure. The maximum mesh step was set as 1 nm along all the directions. The permittivity of Au and Ag were adopted from the experimental data from Johnson and Christy,[175] and Palik,[176] respectively. All the electric field profiles were calculated at the wavelengths of plasmon resonance.

4.2.5 Sample preparation for characterizations

Copolymers and NP building blocks were prepared and characterized using the same approaches as described in Chapter 3.2.7. For assemblies:

UV-vis absorption spectroscopy. Extinction spectra of samples was measured in a range of 400-1100 nm using a PERKIN LAMBDA 35 UV/vis system.

Electron microscopy. The morphologies of assemblies were obtained using a Hitachi SU-70 Schottky field-emission-gun scanning electron microscope and a JEOL FEG transmission electron microscope. Samples for scanning and transmission electron microscopy analysis were prepared by depositing ~2 μL of solution on silicon

wafer and 300 mesh copper grids covered with carbon film, respectively. The samples were dried at room temperature before imaging measurement.

4.3 Results and discussion

4.3.1 Polymeric ligand-mediated self-assembly

In this chapter, we use the polymeric ligand-mediated regioselective self-assembly described in Chapter 3 to fabricate plasmonic nanoclusters with different bonding modes (**Figure 4.1**). With edge-type bonding between the central Au nanosphere (NP-**B**) and the surrounding Ag nanoplates (NP-**A**s), the "nanoflowers" (e-**BA**$_x$) were formed with variable number of petals, *x*. Similarly, face-type bonding between the central NP-**B** and the surrounding NP-**A**s enables the formation of "nanobuds" (f-**BA**$_x$).

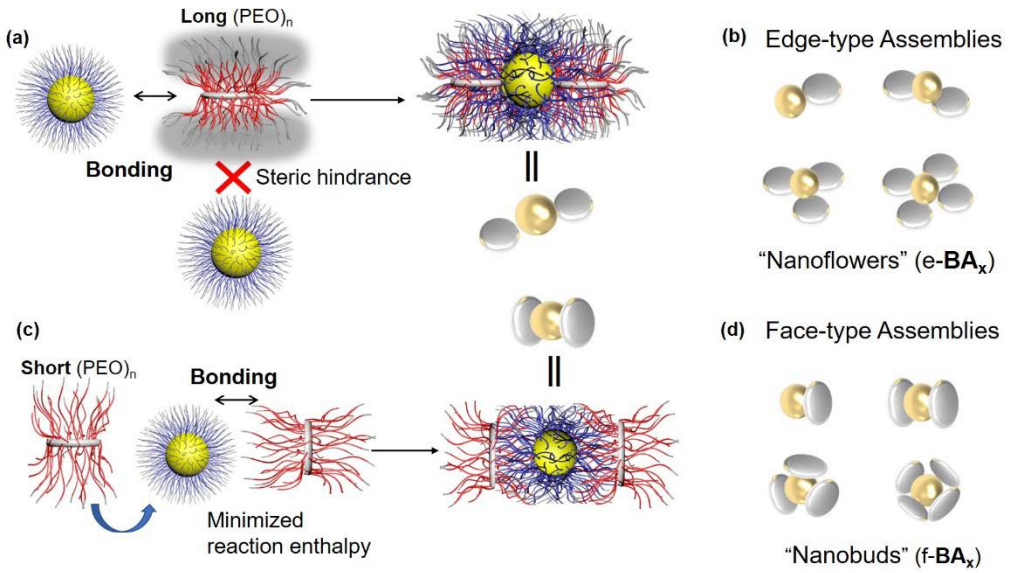

Figure 4.1 (a, c) Schematic illustration of polymeric ligand-mediated regioselective self-assembly of NP-**A**s and NP-**B**s into (b) edge-type and (d) face-type assemblies.

As described in Chapter 3.3.1 and 3.3.2, NP-**A**s and NP-**B**s are uniformly grafted with block copolymer ligands carrying complementary weak acid and base groups,

respectively, for bonding. The outer, non-reactive blocks act as stabilizers for the NPs (**Figure 4.2**). Specifically, NP-**A**s are grafted with a copolymer of poly(ethylene oxide)$_n$-*b*-poly(acrylic acid$_\alpha$-*r*-styrene$_{1-\alpha}$)$_m$-SH [PEO$_n$-*b*-P(AA$_\alpha$-*r*-St$_{1-\alpha}$)$_m$], whereas NP-**B**s are grafted with a copolymer of poly(ethylene oxide)$_k$-*b*-poly(N,N-dimethylaminoethyl methacrylate$_\beta$-*r*-styrene$_{1-\beta}$)$_l$-SH [PEO$_k$-*b*-P(DMAEMA$_\beta$-*r*-St$_{1-\beta}$)$_l$]. The number of petals, *x*, of **BA$_x$** structures is dictated by the stoichiometry of the acid/base groups on NP-**B**s and NP-**A** within a cluster, and the difference in bonding modes is ascribed to the different steric shielding effect between planar and curved polymer brushes on the disc-shaped NP-**A**s.

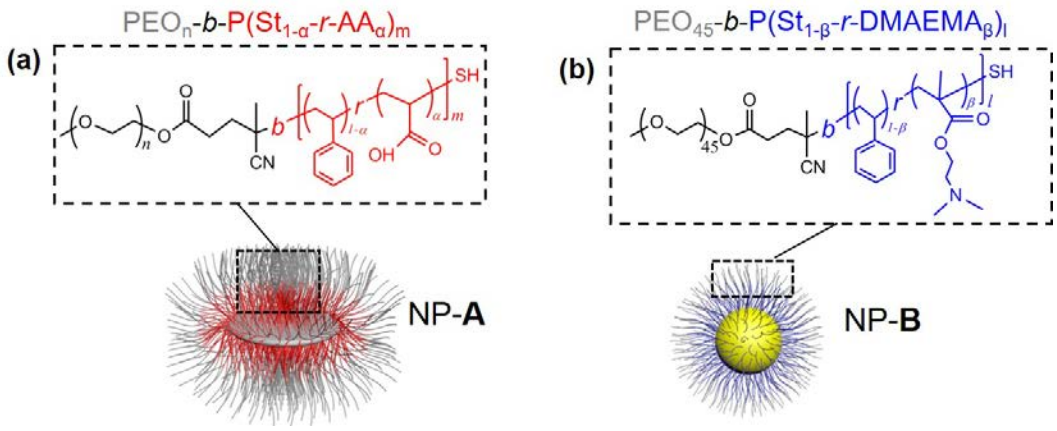

Figure 4.2 Schematic illustration of (a) a copolymer-grafted Ag nanoplate (NP-**A**) and (b) a copolymer-grafted Au nanosphere (NP-**B**).

4.3.2 Formation of the plasmonic nanoflowers

Nanoflowers (e-**BA$_x$**) are formed by edge-type bonding between the central NP-**B** and the surrounding NP-**A**s (petals), with a variable number of petals, *x*. When the *n* of PEO$_n$-*b*-P(AA$_\alpha$-*r*-St$_{1-\alpha}$)$_m$ ligands on NP-**A**s is large ($n > 100$, *e.g.*, $n = 113$), the steric effect of the long, non-reactive PEO blocks of the planar copolymer brushes on each

face of the NP-**A**s shields the reactive block adjacent to the NP surface from reacting with the copolymers on the NP-**B**s. Spherical NP-**B**s, thus, prefer to undergo edge-type bonding with NP-**A**s. The control over x is achieved by varying the number ratio, $Z_{B/A}$, of base groups on a single NP-**B** to acid groups on a single NP-**A**, and the feeding ratio, $\psi_{A/B}$. The $Z_{B/A}$ is the reciprocal of the $Z_{A/B}$ (defined in equation 3.4, for NP-**A** centered assemblies), and can be expressed as

$$Z_{B/A} = \frac{\beta \cdot l}{\alpha \cdot m} \cdot \frac{\sigma_{\boldsymbol{B}}}{\sigma_A} \cdot \frac{{D_B}^2}{h \cdot D_A}, \tag{4.1}$$

where the subscripts A and B represent NP-**A**s and NP-**B**s, respectively, and αm, βl and h are the number of acid groups of a PEO_n-*b*-$P(AA_{\alpha}$-*r*-$St_{1-\alpha})_m$ chain, the number of base groups of a PEO_k-*b*-$P(DMAEMA_{\beta}$-*r*-$St_{1-\beta})_l$ chain, and the thickness of disc-shaped NP-**A**s, respectively. In experiments, we tuned the values of $Z_{B/A}$ by varying βl of PEO-*b*-P(DMAEMA-*r*-St) copolymers on NP-**B**s, while keeping αm of PEO-*b*-P(AA-*r*-St) copolymers on NP-**A**s constant at 65. As shown in **Figure 4.3**, when βl increased from 65 to 168 ($Z_{B/A}$ increased from 1.36 to 3.79), the number of petals, x, increased from 1 to 3 for nanoflowers. Without further purification, the yields of e-**BA**, e-**BA$_2$**, and e-**BA$_3$** nanoflowers were 68%, 65% and 59%, respectively (**Figure 4.4**). This assembly strategy showed high regioselectivity, with over 90% edge-type bonding in the e-**BA$_x$** clusters (**Figure 4.5**).

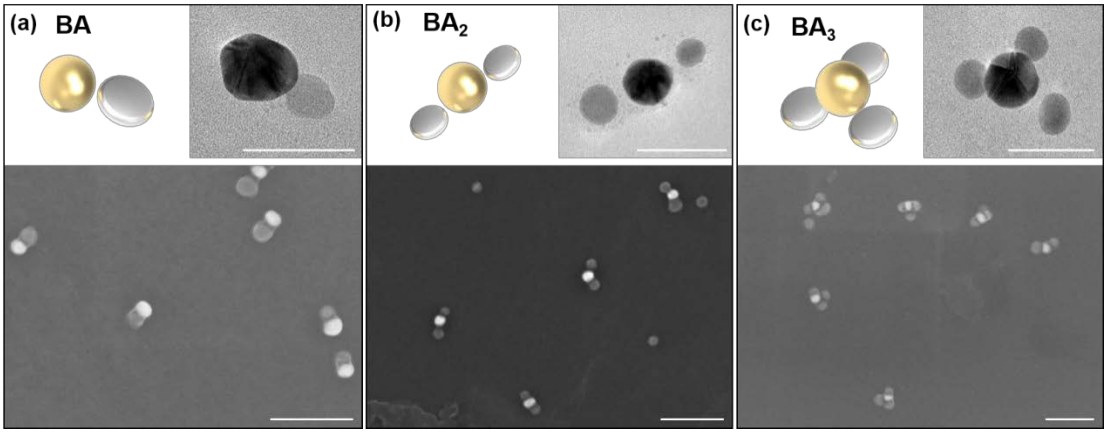

Figure 4.3 Schemes (top, left), transmission electron micrographs (TEMs, top, right), and scanning electron micrographs (SEMs, bottom) of edge-type NP clusters with different configurations: (a) **BA**, (b) **BA2**, and (c) **BA3**. **NP-A**s: PEO_{113}-*b*-P($AA_{0.26}$-*r*-$St_{0.74}$)$_{249}$-grafted Ag nanoplates; **NP-B**s: Au nanospheres grafted with (a) PEO_{45}-*b*-P($DMAEMA_{0.40}$-*r*-$St_{0.60}$)$_{419}$, (b) PEO_{45}-*b*-P($DMAEMA_{0.30}$-*r*-$St_{0.70}$)$_{244}$, and (c) PEO_{45}-*b*-P($DMAEMA_{0.41}$-*r*-$St_{0.59}$)$_{158}$ copolymers. $\psi_{A/B}$: (a) 1:1, (b) 2:1, and (c) 3:1. Au is brighter than Ag in SEMs but darker in TEMs. Scale bars: 50 nm in TEMs and 200 nm in SEMs.

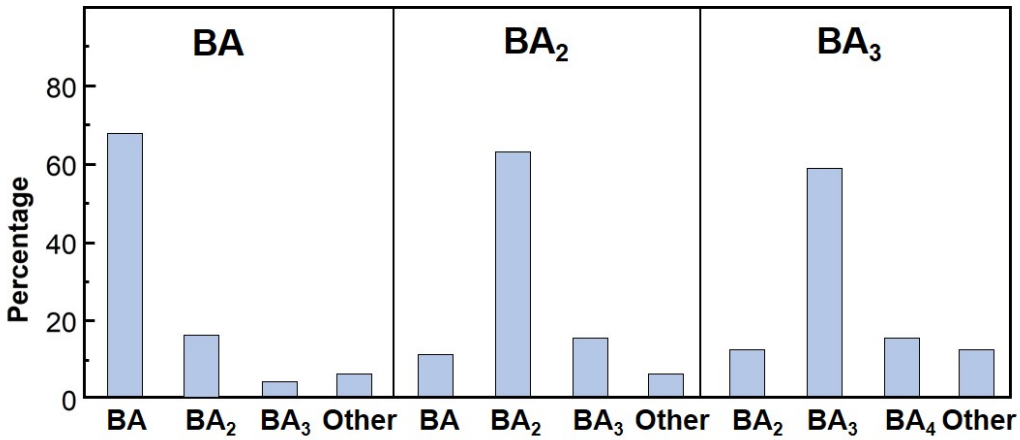

Figure 4.4 Distribution of e-**BA$_x$** clusters. Over 500 clusters were analyzed for each plot.

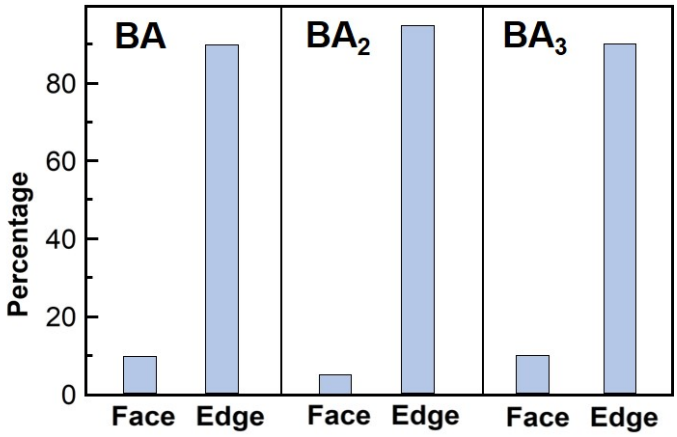

Figure 4.5 Distribution of bonding modes in e-**BA$_x$** clusters. Over 500 clusters were analyzed for each plot.

4.3.3 Formation of the plasmonic nanobuds

Nanobuds (f-**BA$_x$**) are formed by face-type bonding between the central NP-**B** and the surrounding NP-**A**s (petals), with variable number of petals, *x*. At n = 45 for PEO$_n$-*b*-P(AA$_\alpha$-*r*-St$_{1-\alpha}$)$_m$-grafted NP-**A**s, the steric shielding of short PEO blocks is negligible. NP-**A**s prefer to undergo face-type bonding with an NP-**B** with maximized conformal contact and extent of reaction between copolymer ligands to minimize the overall energy of the assembly system. Similar to nanoflowers, the control over *x* in nanobuds is also achieved by varying the number ratio, $Z_{B/A}$ of base groups on a single NP-**B** to acid groups on a single NP-**A**, and the feeding ratio, $\psi_{A/B}$. Notably, due to the disc-like shape of NP-**A**s, although the polymeric ligands on an NP-**A** are flexible, not all of the acid groups of the grafted polymers are accessible to the base groups of a single NP-**B** in the face-type bonding mode (as shown in **Figure 4.1c** by the red unreacted polymeric ligands on one side of Ag nanoplates). In our rough estimation, only ~60% of acid groups on one NP-**A** interact with base groups on a single NP-**B** in the face-type

bonding mode. Hence, for nanobuds, a modified number ratio, $Z^*_{B/A}$, of base groups on a single NP-**B** to accessible acid groups on a single NP-**A** in the face-type bonding mode, was defined as

$$Z^*_{B/A} \approx 0.6 \cdot Z_{B/A} = 0.6 \frac{\beta \cdot l}{\alpha \cdot m} \cdot \frac{\sigma_{\boldsymbol{B}}}{\sigma_A} \cdot \frac{{D_B}^2}{h \cdot D_A}, \quad (4.2)$$

where the subscripts are the same as in equation 4.1.

In experiments, we tuned the values of $Z^*_{B/A}$ by varying *αm* of the PEO-*b*-P(AA-*r*-St) copolymers on NP-**A**s, while keeping *βl* of the PEO-*b*-P(DMAEMA-*r*-St) copolymers on NP-**B**s constant at 168. As shown in **Figure 4.6**, when *αm* decreased from 229 to 107 ($Z_{B/A}$ increased from 1.31 to 3.88), the number of petals, *x*, increased from 1 to 4 for nanobuds. Considering that the unreacted of acid groups on NP-**A**s may lead to the formation of NP-**A**-centered clusters with the presence of extra NP-**B**s, we introduced excessive NP-**A**s during self-assembly process to ensure the formation of nanobuds with NP-**B**s in the center of assemblies. Hence, the feeding ratio $\psi_{A/B}$ is usually larger than the target *x* value in the formation of nanobuds. Without further purification, the yields of f-**BA**$_2$, f-**BA**$_3$, and f-**BA**$_4$ nanobuds were 62%, 65% and 58%, respectively (**Figure 4.7**). The regioselectivity of nanobuds is not as high as that of nanoflowers, with over 80% face-type bonding in the f-**BA**$_x$ (*x* = 1, 2, 3) clusters (**Figure 4.8**).

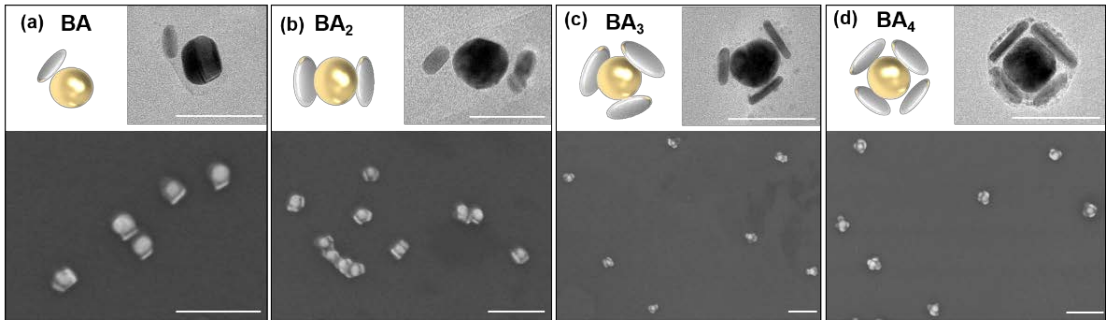

Figure 4.6 Scheme (top, left), TEMs (top, right), and SEMs (bottom) of face-type NP clusters with different configurations: (a) **BA**, (b) **BA**$_2$, (c) **BA**$_3$**,** and (d) **BA**$_4$. **NP-B**s: PEO$_{45}$-*b*-P(DMAEMA$_{0.40}$-*r*-St$_{0.60}$)$_{419}$-grafted Au nanospheres; **NP-A**s: Ag nanoplates grafted with (a) PEO$_{45}$-*b*-P(AA$_{0.30}$ -*r*-St$_{0.70}$)$_{756}$-SH, (b) PEO$_{45}$-*b*-P(AA$_{0.32}$ -*r*-St$_{0.68}$)$_{550}$-SH, (c) PEO$_{45}$-*b*-P(AA$_{0.36}$ -*r*-St$_{0.64}$)$_{467}$-SH, and (d) PEO$_{45}$-*b*-P(AA$_{0.32}$ -*r*-St$_{0.68}$)$_{335}$-SH copolymers. $\psi_{A/B}$: (a) 1.2:1, (b) 2.5:1, (c) 3.5:1, (d)4.2:1. Au is brighter than Ag in SEMs but darker in TEMs. Scale bars: 50 nm in TEMs and 200 nm in SEMs.

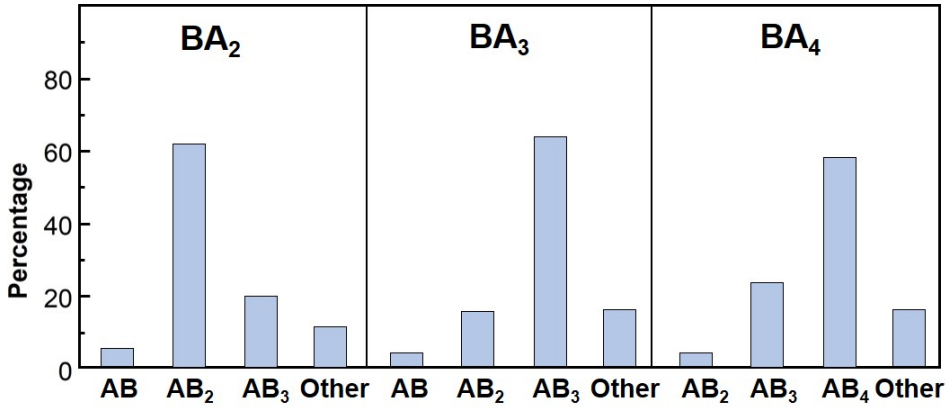

Figure 4.7 Distribution of f-**BA**$_x$ clusters. Over 500 clusters were analyzed for each plot.

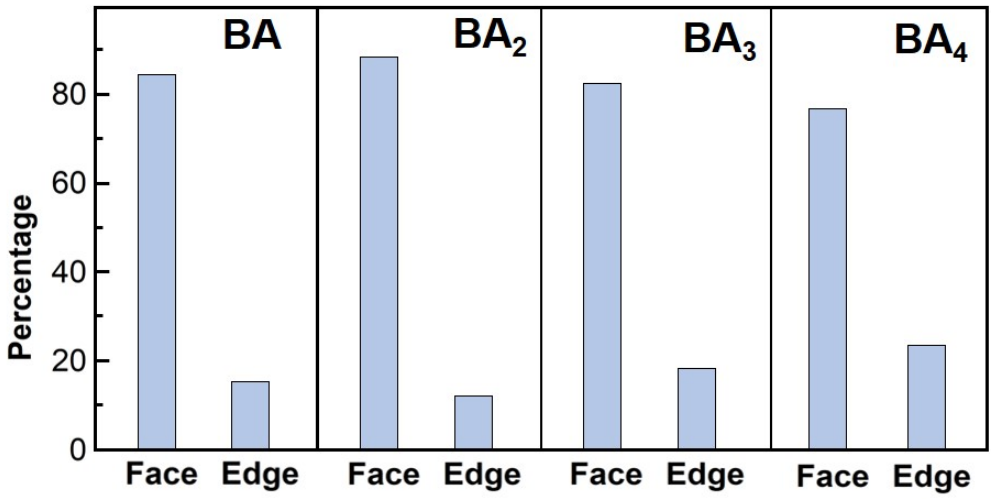

Figure 4.8 Distribution of bonding modes in f-**BA**$_x$ clusters. Over 500 clusters were analyzed for each plot.

4.3.4 Experiments and simulations on extinction spectra of nanoflowers and nanobuds

We investigated the optical properties of nanobuds (f-**BA** and f- **BA**$_2$) and nanoflowers (e-**BA** and e-**BA**$_2$) using experiments and finite-difference time-domain (FDTD) simulations (**Table 4.1**, **Figure 4.9** and **4.10**). In experiments, the bonding of NP-**B**s with NP-**A**s in both modes led to redshifts in the LSPR bands. The magnitude of the redshift is dependent on the bonding mode, which determines the relative orientations of NPs in nanoclusters. **Figure 4.9** shows the normalized extinction spectra of polymer-grafted Ag nanoplates (NP-**A**s), f-**BA**, f-**BA**$_2$, e-**BA**, and e-**BA**$_2$ nanoclusters in the range of 400-900 nm. The NP-**A**s showed a prominent peak at 688 nm originating from the in-plane dipolar resonance of Ag nanoplates. After the formation of face-type bonding with NP-**B**s, the peak redshifted to 700 nm and 707 nm for f-**BA** and f-**BA**$_2$ nanobuds, respectively. The nanoflowers showed further redshifts, with longitudinal LSPR bands located at 738 nm (e-**BA**) and 757 nm (e-**BA**$_2$). The NP

orientation-dependent redshift in the longitudinal LSPR band was confirmed by FDTD simulations, in which the calculated LSPR peaks of nanoflowers redshifted further than the nanobuds with the same number of petals (**Figure 4.10** and **Table 4.1**). In simulated spectra, notably, the e-**BA** and e-**BA$_2$** nanoflowers showed double peaks at the range of 700-770 nm, whereas the f-**BA$_2$** structures showed a peak with a shoulder at ~580 nm. These subtle spectral features were not present in the experimental spectra, which may be due to some degree inhomogeneity of the assemblies prepared by the colloidal assembly methods. In support of this hypothesis, we observe a single, broader, peak for nanoflowers at the same range of wavelengths.

Table 4.1 Peak wavelength (λ_{max}) of nanoclusters in experimental and simulated extinction spectra.

λ_{max} (nm)	AgNP	f-**BA**	f-**BA$_2$**	e-**BA**	e-**BA$_2$**
Experiments	688	700	707	738	757
Simulations	686	715	721	741	766

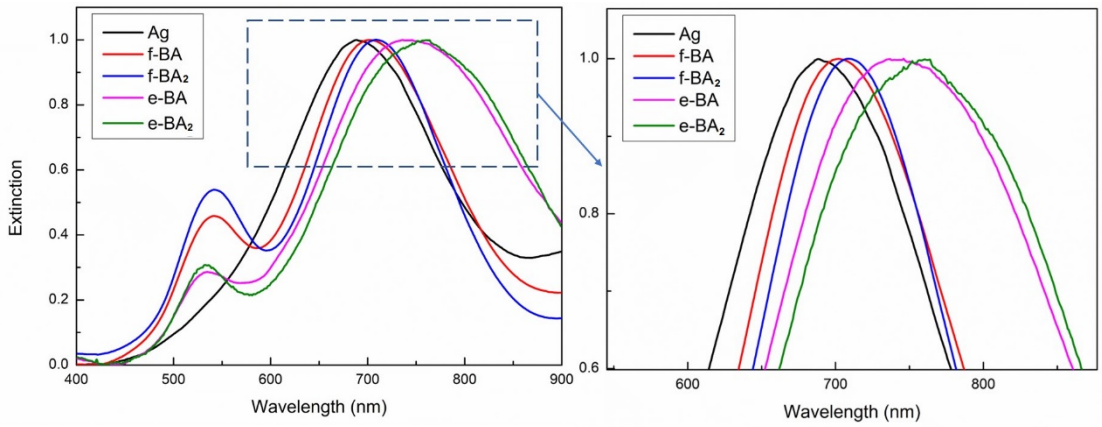

Figure 4.9 (left) Experimental extinction spectra (normalized) of polymer-grafted Ag nanoplates, f-**BA**, f-**BA$_2$**, e-**BA**, and e-**BA$_2$** nanoclusters and (right) a zoom-in of the region in the dashed box.

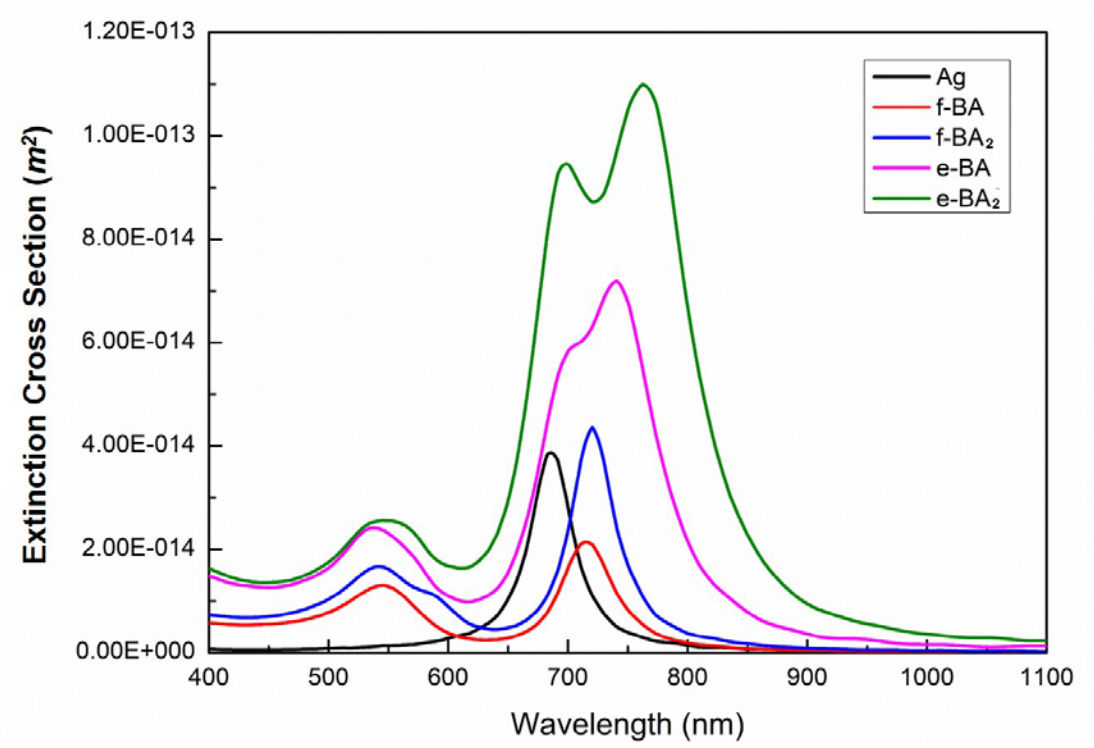

Figure 4.10 Simulated extinction spectra for polymer-grafted Ag nanoplates, f-**BA**, f-**BA**$_2$, e-**BA**, and e-**BA**$_2$ nanoclusters.

To investigate the origins of the shouldered peak for nanobuds and the double peaks for nanoflowers, the extinction spectra with different polarization and light incidence directions were calculated, and are presented for f-**BA**$_2$, e-**BA**, and e-**BA**$_2$ in **Figures 4.11**, **4.12**, and **4.13**, respectively. The polarization spectra of polymer-grafted Ag nanoplates were shown in **Figure 3.14**. The out-of-plane (*z* axis) polarization had a minimal contribution to the overall extinction spectra, whereas the in-plane polarizations along the *x* and *y* axes contributed equally at the same wavelength to the overall extinction. After the formation of nanobuds or nanoflowers, the pristine polarizations of Ag nanospheres were changed by the plasmon coupling with Au nanospheres along different axes. As shown in **Figure 4.11**, the shouldered peak of f-**BA**$_2$ nanobuds originates from the polarization along z direction, due to the coupling

of the out-of-plane polarization of Ag nanoplates with the Au nanospheres. In e-**BA** and e-**BA**$_2$ nanoflowers, the edge-type bonding between Au nanospheres and Ag nanoplates is along the *y* axis, which made the in-plane polarizations along the *y* axis (at 741 nm and 766 nm, respectively) different from those along the *x* axis (at 688 nm), and hence the nanoflowers show double peaks in those ranges.

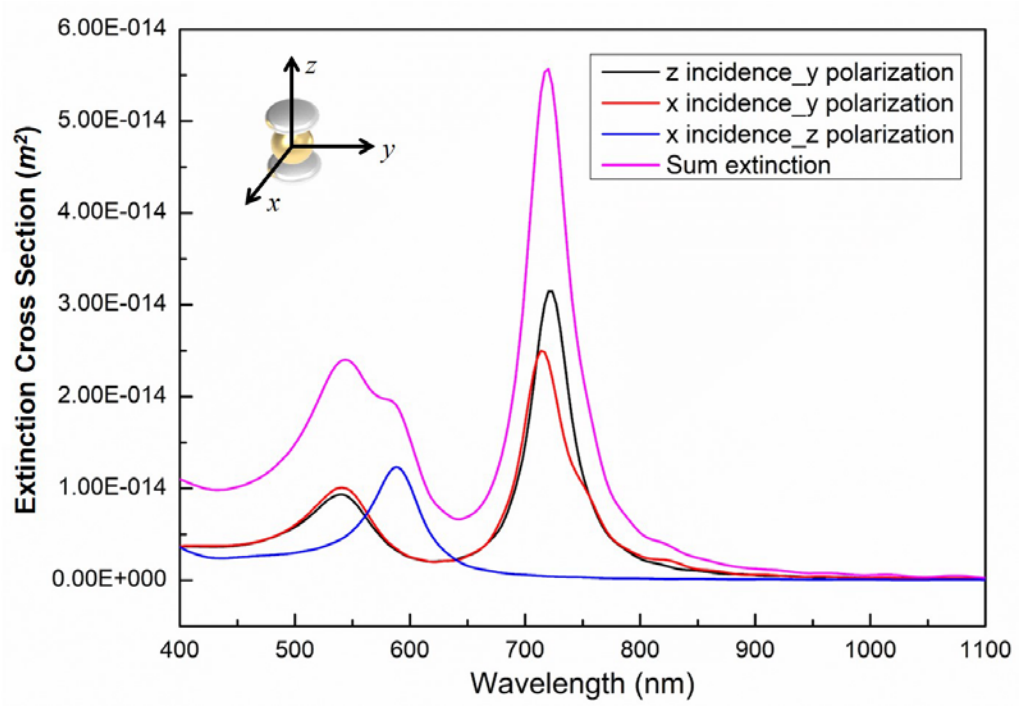

Figure 4.11 Calculated extinction spectrum of f-**BA**$_2$ nanobuds in different polarization and light incidence direction. The overall simulated extinction spectrum was obtained by summing the spectra from all contributing incident directions and polarization states.

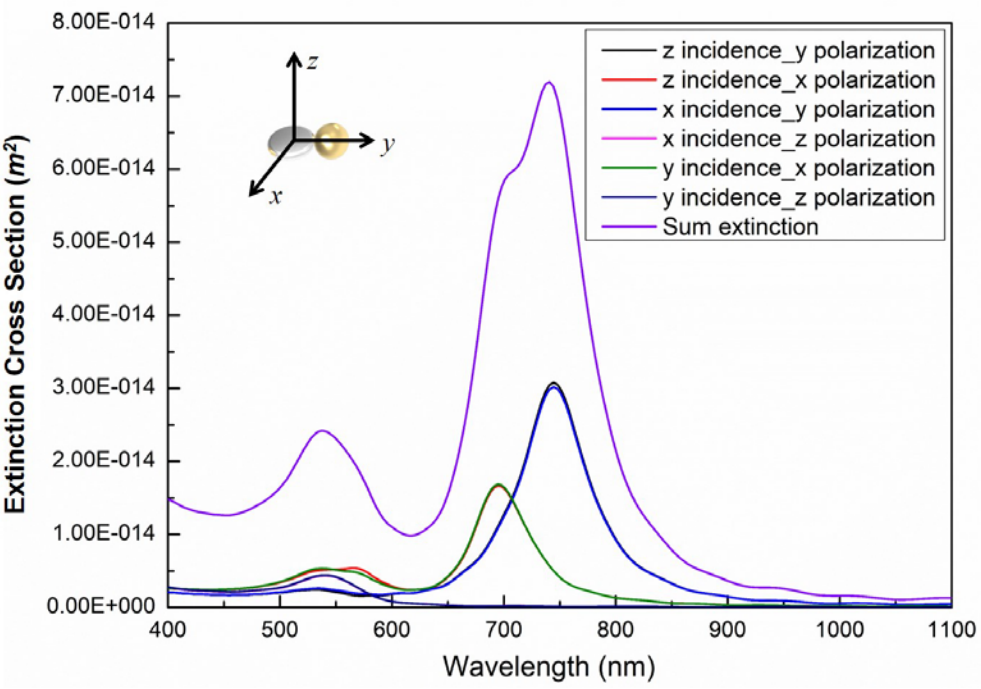

Figure 4.12 Calculated extinction spectrum of e-**BA** nanoflowers in different polarization and light incidence direction. The overall simulated extinction spectrum was obtained by summing the spectra from all contributing incident directions and polarization states.

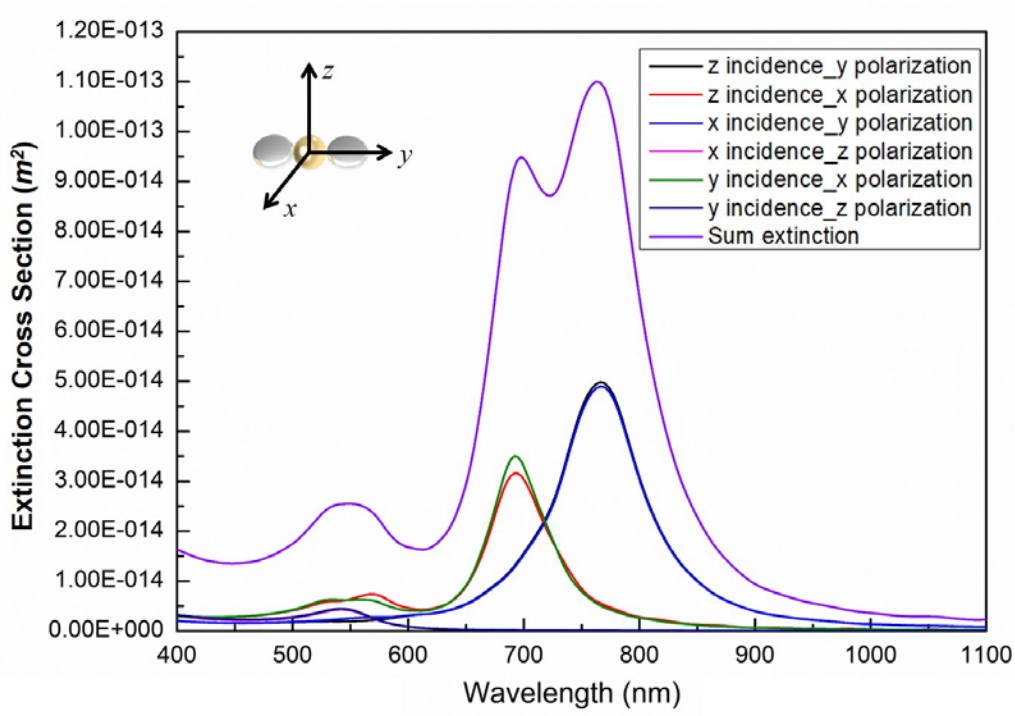

Figure 4.13 Calculated extinction spectrum of e-**BA**$_2$ nanoflowers in different polarization and light incidence direction. The overall simulated extinction spectrum was obtained by summing the spectra from all contributing incident directions and polarization states.

4.3.5 Electric-field enhancement of nanoflowers and nanobuds

We calculated the electric-field enhancement of f-**BA**$_2$ and e-**BA**$_2$ clusters at their LSPR peak wavelengths and with the most pronounced polarization directions, as shown in Figures **4.14** and **15**, respectively. When the electric field was polarized in the direction perpendicular to the nanoplates, the f-**BA**$_2$ structure (**Figure 4.14a**) showed stronger enhancement intensity in comparison with the e-**BA**$_2$ clusters (**Figure 4.15a, b**). When the electric field was polarized in the direction parallel to the nanoplates, the e-**BA**$_2$ structure (**Figure 4.15c, d**) showed stronger enhancement intensity in comparison with the f-**BA**$_2$ clusters (**Figure 4.14b**).

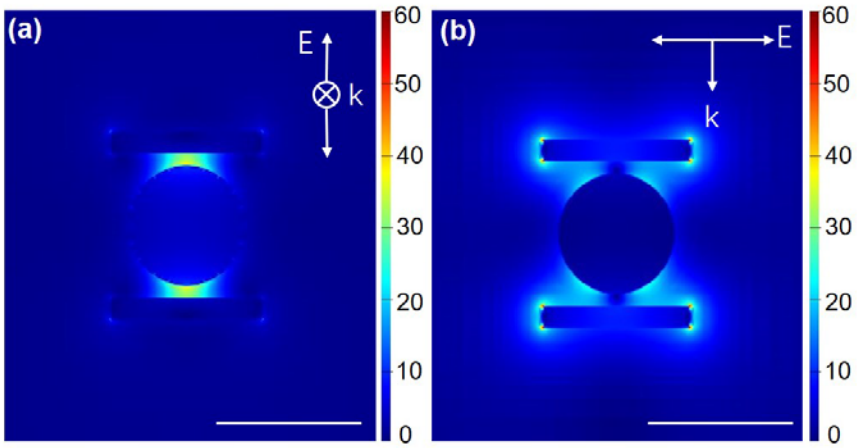

Figure 4.14 Electric-field intensity enhancement contours of the f-**BA**$_2$ nanobud at (a) 588 nm and (b) 721 nm. The directions of the electric-field polarizations (*E*) are (a) perpendicular and (b) parallel to the plane of nanoplates. The incident light (*k*) is (a) parallel and (b) perpendicular to the plane of nanoplates. Scale bars: 50 nm.

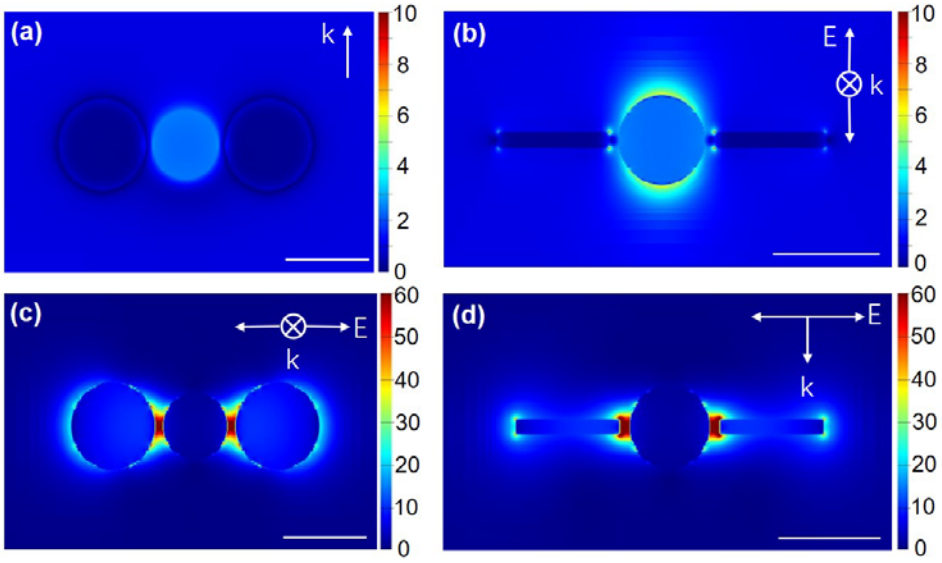

Figure 4.15 Electric-field intensity enhancement contours of the e-BA_2 nanoflower at (a, b) 541 nm and (c, d) 766 nm. The directions of electric field polarizations (*E*) are (a, b) perpendicular and (c, d) parallel to the plane of nanoplates. The incident light (*k*) is (a, b) parallel and (c, d) perpendicular to the plane of nanoplates. Scale bars: 50 nm.

4.4 Conclusion

In this chapter, we used the polymeric ligand-mediated regioselective bonding to construct various binary plasmonic nanoclusters, nanoflowers and nanobuds, with different spatial arrangements of Au nanospheres and Ag nanoplates. The number of petals was tuned by the stoichiometry of the acid-base reaction between the reactive blocks of copolymer ligands. The nanoflowers and nanobuds with the same number of petals showed different plasmon-coupling modes and electric-field enhancements due to the different bonding types between the Ag nanoplates and Au nanospheres. The nanoflowers with edge-type bonding better facilitates the coupling of Au nanospheres to the in-plane polarization of the Ag nanoplates. Thus, the nanoflowers showed further LSPR shift and stronger field enhancement. This study shows the feasibility of constructing complex plasmonic nanostructure by polymeric ligand-mediated self-assembly and offers great opportunities for designing functional nanostructures with high structural complexity for diverse applications.

Chapter 5: Conclusions and Future Works

5.1 Conclusions

The objective of this dissertation is to develop wet-chemistry synthesis and self-assembly approaches for complex and defined plasmonic nanostructures. In chapter 2, a facile synthetic method was developed for freestanding circular and triangular Au nanorings (AuNRs) with tunable sizes, thicknesses, and surface roughness. The in-plane LSPR peak of AuNRs is highly tunable through the NIR region by tuning the ring thickness through additional Au deposition with controlled infusion rates of presursors. In chapter 3, we combined the steric hindrance of polymeric ligand brushes and the anisotropy of nanoparticles to create regioselective bonding between gold nanospheres on silver nanoplates. The regioselectivity enables a self-assembly system with precise control over the relative orientation of Au nanospheres on Ag nanoplates, while the stoichiometry of reactive groups of copolymeric ligands dictates the number of nanoparticles in one cluster. The yield of each assembly was ~70% without further purification. Assemblies with different bonding types showed different LSPR peak shifts and electric field enhancements, originating from different bonding types. In chapter 4, the regioselective self-assembly was applied to fabricate various plasmonic nanocluster, nanoflowers and nanobuds. Edge-type and face-type bonding modes dictated the modes of plasmonic coupling between the Ag nanoplate and the Au nanospheres within one cluster. Nanoclusters with different bonding types showed substantial difference in optical response. Compared with nanobuds, nanoflowers with the same number of petals showed stronger electric field enhancement in simulations and further LSPR peak shifts in experiments and simulations.

As discussed in Chapter 3 and 4, the yields of various assemblies were relatively high (60 - 75%) without further purifications. However, systematic study is needed in the future for the stability of those assemblies as a function of time, temperature, and solvent quality, as those factors affect the conformation of polymeric ligands and hence the structure of nanoclusters.

Although there is still plenty of room to optimize the yields and stability of the above-mentioned products, the synthetic and self-assembly methods demonstrated in this dissertation showed great potentials and versatility in designing not only plasmonic nanoclusters, but also other inorganic nanoparticle-based functional structures with high complexity.

5.2 Future work: Self-assembly of Au nanorings

We have demonstrated a facile synthetic route for freestanding Au nanorings (AuNRs) with different dimensions and surface roughness in chapter 2. Similar to Ag nanoplates, the as-prepared AuNRs are stabilized by citrate in aqueous solutions and can be surface-modified with thiol-terminated polymeric ligands after ligand exchange. Grafting polymers onto AuNRs introduces new energetic contributions arising from interaction enthalpy and conformational entropy of polymeric ligands. These energetic contributions can be tailored by controlling the chemical moieties, persistence lengths, and surrounding solvents of polymeric ligands. As plasmonic nanostructures with unique morphologies, the AuNRs can be interesting building blocks for various explorations in colloidal self-assembly. Here, I propose 2 future works closely relevant to this dissertation using Au nanorings as building blocks in interfacial and

regioselective self-assembly. The plasmonic nature of AuNRs make those assemblies good platforms for many potential applications in optical devices and biosensors.

5.2.1 Self-assembled monolayers of Au nanorings

Au nanorings with their 2D geometries are perfect building blocks for fabricating self-assembled monolayers (**Figure 5.1**). Interfacial self-assembly, driven by the reduction of interfacial energy, is a facile and powerful method for the assembly of 2D periodical arrays. After ligand exchange with commercialized thiol-terminated polystyrene (PS-SH), the preformed Au nanorings were transferred into toluene, a good solvent for PS.

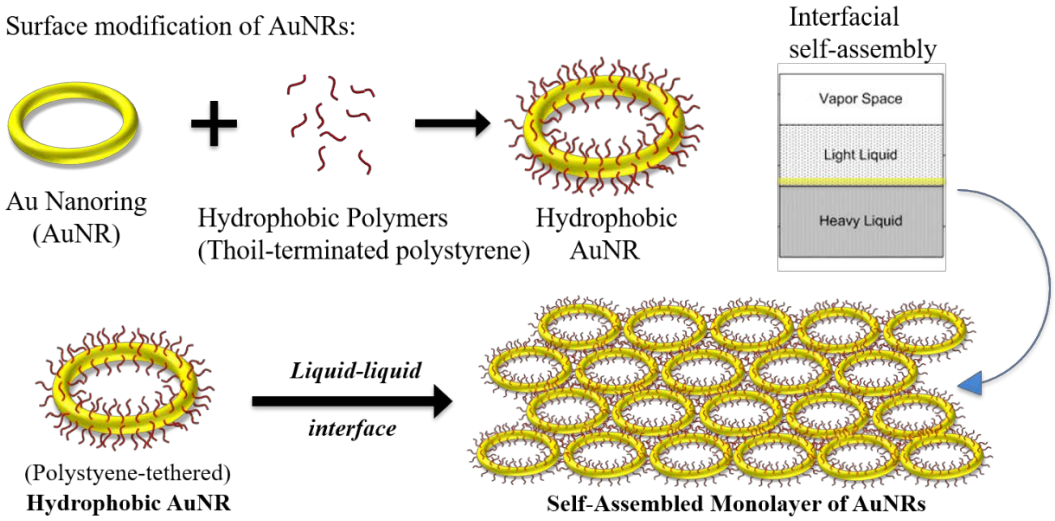

Figure 5.1 Schematic illustration of self-assembled monolayers of AuNRs.

As a demonstration, a self-assembled array of triangular AuNRs (110 nm in edge length, 18 nm in thickness) tethered with PS-SH (50K) was prepared by interfacial self-assembly (**Figure 5.2**). In a typical process, 0.2 ml toluene solution containing ~0.1 mg polystyrene-tethered AuNRs was drop-cast onto a surface of diethyene glycol (DEG) in a Teflon well (1.5×1.5×1.5 cm^3). The well is then covered with a glass slide to slow

down the evaporation rate of toluene. A monolayer of AuNRs formed at the toluene-DEG interface due to the reduction of interfacial energy. After 5 h, the film was transferred onto a piece of Si wafer (1×1 cm^2), dried under vacuum for 30 min to remove residual solvents, and imaged by SEM.

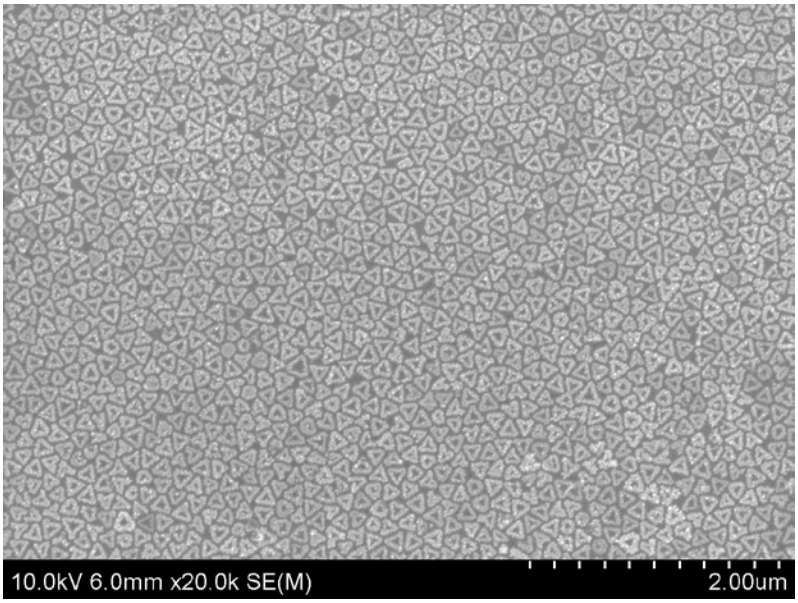

Figure 5.2 SEM image of self-assembled monolayer of triangular AuNRs (110 nm in edge length, 18 nm in thickness) tethered with PS-SH (50K).

The optical properties of the self-assembled monolayers can be tunabled by the geometric parameters of AuNRs and the interparticle distance of adjacent AuNRs. By changing the molecular weights of PS ligands (*e.g.*, from 12,000 to 65,000), the interparticle distance of AuNRs can be tailored. The self-assembled monolayers with tunable optical response have great potential in sensing applications and for fabricating optical devices.

5.2.2 Regioselective self-assembly of nanospheres and circular nanoring

AuNRs are unique nanostructures with enhanced electric field in their inner cavity and outer surface that are both accessible for other nanoparticles to interact with. As demonstrated in chapter 3 and 4, the bonding modes of nanoparticles significantly affect the optical properties of their assemblies. Regioselective self-assembly of AuNRs with other plasmonic nanoparticles is highly desirable for studying their plasmon-couplings behaviors. The regioselective bonding is based on the same mechanism described in chapter 3.3.1. AuNRs and Au nanospheres (AuNSs) are grafted with block copolymer ligands in which the NP-adjacent reactive block carries complementary weak acid or base groups for bonding and the non-reactive block acts as stabilizers for the NPs (**Figure 5.3**). The reactive blocks of complementary polymeric ligands drive the self-assembly and the nonreactive PEO blocks create different level of steric hindrance between the inner cavity and outer surface of the AuNRs. Long PEO (n>100) blocks will create a more compact steric brush layer at the inner cavity of AuNRs (50 nm in diameter) to block the bonding of AuNSs, and thus the AuNSs will prefer to bind to the outer surface of AuNRs to form the diamond ring structures. Short PEO (n<50) blocks will not create significant steric layers at the inner cavity of AuNRs, and thus the Saturn-like structures will be preferred due to the maximum contact area (minimum reaction enthalpy) between the building blocks. The diamond ring structure and the Saturn-like structure are expected to show very different LSPR peaks and electric field enhancement patterns. This study will enrich our understanding of plasmon-coupled system and facilitate the construction of advanced plasmonic nanomaterials.

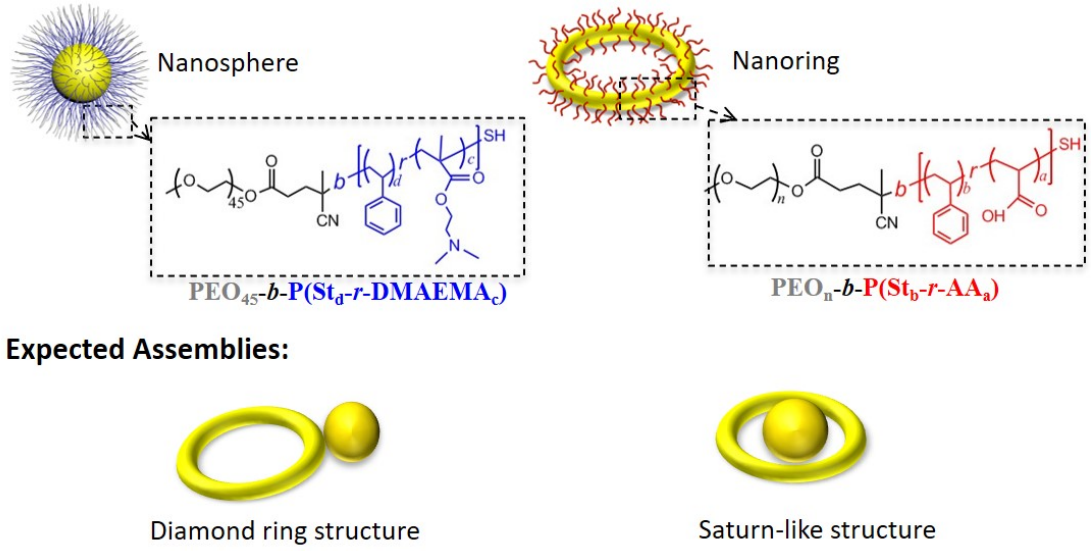

Figure 5.3 Schematic illustrations of a copolymer-grafted Ag nanoplate, a copolymer-grafted Au nanosphere, and expected assembled structures.

References

1. Maier, S. In Plasmonics: Fundamentals and Applications. *Springer: Berlin,* **2007.**
2. Jiang, N.; Zhuo, X.; Wang, J. Active Plasmonics: Principles, Structures, and Applications. *Chem. Rev.* **2018,** *118,* 3054.
3. Barnes, W. L.; Dereux, A.; Ebbesen, T. W. Surface Plasmon Subwavelength Optics. *Nature* **2003**, *424,* 6950, 824.
4. Foss, C. A.; Hornyak, G. L.; Stockert, J. A.; Martin, C. R. Template-Synthesized Nanoscopic Gold Particles: Optical Spectra and the Effects of Particle Size and Shape. *J. Phys. Chem.* **1994,** *98,* 11, 2963.
5. Wiley, B. J.; Im, S. H.; Li, Z.-Y.; Mclellan, J.; Siekkinen, A.; Xia, Y. Maneuvering the Surface Plasmon Resonance of Silver Nanostructures through Shape-Controlled Synthesis. *J. Phys. Chem. B* **2006,** *110,* 15666.
6. Link, S.; El-Sayed, M. A. Shape and Size Dependence of Radiative, Non-Radiative and Photothermal Properties of Gold Nanocrystals. *Int. Rev. Phys. Chem.* **2000,** *19,* 409.
7. Kelly, K. L.; Coronado, E.; Zhao, L. L.; Schatz, G. C. The Optical Properties of Metal Nanoparticles: The Influence of Size, Shape, and Dielectric Environment. *J. Phys. Chem. B* **2003,** *107,* 668.
8. Xia, Y.; Xiong, Y.; Lim, B.; Skrabalak, S. E. Shape-Controlled Synthesis of Metal Nanocrystals: Simple Chemistry Meets Complex Physics? *Angew Chem Int Ed Engl*, **2009**, *48*, 60.

9. Jain, P. K.; Huang, X.; El-Sayed, I. H.; El-Sayed, M. A. Noble Metals on the Nanoscale: Optical and Photothermal Properties and Some Applications in Imaging, Sensing, Biology, and Medicine. *Acc. Chem. Res.,* **2008,** *41,* 1578.
10. Luther, J. M.; Jain, P. K.; Ewers, T.; Alivisatos, A. P. Localized Surface Plasmon Resonances Arising from Free Carriers in Doped Quantum Dots. *Nat. Mater.* **2011,** *10,* 361.
11. Alvarez, M. M.; Khoury, J. T.; Schaaff, T. G.; Shafigullin, M. N.; Vezmar, I.; Whetten, R. L. Optical Absorption Spectra of Nanocrystal Gold Molecules. *J. Phys. Chem. B* **1997,** *110,* 3706.
12. Kanehara, M.; Koike, H.; Yoshinaga, T.; Teranishi, T.; Indium Tin Oxide Nanoparticles with Compositionally Tunable Surface Plasmon Resonance Frequencies in the Near-IR Region. *J. Am. Chem. Soc.* **2009,** *131,* 17736.
13. Kundu, J.; Le, F.; Nordlander, P.; Halas, N. J. Surface Enhanced Infrared Absorption (SEIRA) Spectroscopy on Nanoshell Aggregate Substrates. *Chem. Phys. Lett.* **2008,** *452,* 115.
14. Norris, D. J.; Efros, A. L.; Erwin, S. C. Doped Nanocrystals. *Science* **2008,** *319,* 1776.
15. Yu, H.; Peng, Y.; Yang, Y.; Li, Z.-Y. Plasmon-Enhanced Light–Matter Interactions and Applications. *npj Comput. Mater.* **2019,** *5,* 45.
16. El-Sayed, M. A.; Lee, K. S. Gold and Silver Nanoparticles in Sensing and Imaging Sensitivity of Plasmon Response to Size, Shape, and Metal Composition. *J. Phys. Chem. B* **2006,** *110,* 19220.
17. El-Sayed, M. A.; Link, S.; Wang, Z. L. Alloy Formation of Gold−Silver

Nanoparticles and the Dependence of the Plasmon Absorption on Their Composition. *J. Phys. Chem. B* **1999,** *103,* 3529.

18. Verbruggen, S. W.; Keulemans, M.; Martens, J. A.; Lenaerts, S. Predicting the Surface Plasmon Resonance Wavelength of Gold–Silver Alloy Nanoparticles. *J. Phys. Chem. C* **2013,** *117,* 19142.
19. van de Hulst, H. C. Light Scattering by Small Particles. *Dover: New York,* **1981**.
20. Wei, A. Plasmonic Nanomaterials. In Nanoparticles: Building Blocks for Nanotechnology. Rotello, V., Ed. *Springer US: Boston, MA,* **2004,** 173.
21. Kreibig, U.; Vollmer, M. Optical Properties of Metal Clusters, *Springer: New York,* **1995,** Chapter 2.
22. Fuchs, R. Theory of the Optical Properties of Ionic Crystal Cubes. *Phys. Rev. B* **1975,** *11,* 1732.
23. Haes, A. J.; Haynes, C. L.; McFarland, A. D.; Schatz, G. C.; Van Duyne, R. P.; Zou, S. Plasmonic Materials for Surface-Enhanced Sensing and Spectroscopy. *MRS Bull.* **2005,** *30,* 368.
24. Kottmann, J. P.; Martin, O. J. F.; Smith, D. R.; Schultz, S. Plasmon Resonances of Silver Nanowires with a Nonregular Cross Section. *Phys. Rev. B* **2001,** *64,* 235402.
25. Aizpurua, J.; Bryant, G. W.; Richter, L. J.; Garcia de Abajo, F. J.; Kelley, B. K.; Mallouk, T. Optical Properties of Coupled Metallic Nanorods for Field-Enhanced Spectroscopy. *Phys. Rev. B* **2005,** *71,* 235420.
26. Underwood, S.; Mulvaney, P. Effect of the Solution Refractive Index on the Color of Gold Colloids. *Langmuir* **1994,** *10,* 3427.
27. Mulvaney, P. Surface Plasmon Spectroscopy of Nanosized Metal Particles.

Langmuir **1996,** *12*, 788.

28. Rechberger. W.; Hohenau, A.; Leitner, A.; Krenn, L. B.; Aussenegg, F. R. Optical Properties of Two Interacting Gold Nanoparticles. *Opt. Commun.* **2003,** *220*, 137.
29. Jain, P. K.; Huang, X.; El-Sayed, I. H.; El-Sayed, M. A. Review of Some Interesting Surface Plasmon Resonance-enhanced Properties of Noble Metal Nanoparticles and Their Applications to Biosystems. *Plasmonics* **2007,** *2*, 107.
30. Nordlander, P.; Oubre, C.; Prodan, E.; Li, K.; Stockman, M. I. Plasmon Hybridization in Nanoparticle Dimers. *Nano Lett.* **2004,** *4*, 899.
31. Su, K. H.; Wei, Q.-H.; Zhang, X.; Mock, J. J.; Smith, D. R.; Schultz, S. Interparticle Coupling Effects on Plasmon Resonances of Nanogold Particles. *Nano Lett.* **2003,** *3*, 8, 1087.
32. Storhoff, J. J.; Lazarides, A. A.; Mucic, R. C.; Mirkin, C. A.; Letsinger, R. L.; Schatz, G. C. What Controls the Optical Properties of DNA-Linked Gold Nanoparticle Assemblies? *J. Am. Chem. Soc.* **2000,** *122*, 19, 4640.
33. Lazarides, A. A.; Schatz, G. C. DNA-Linked Metal Nanosphere Materials: Structural Basis for the Optical Properties. *J. Phys. Chem. B* **2000,** *104*, 3, 460.
34. Yoon, J. H.; Lim, J.; Yoon, S. Controlled Assembly and Plasmonic Properties of Asymmetric Core-Satellite Nanoassemblies. *ACS Nano* **2012,** *6*, 7199.
35. Jain P. K.; El-Sayed M. A. Plasmonic Coupling in Noble Metal Nanostructures. *Chem. Phys. Lett.* **2010,** *487*, 153.
36. Jung, H.; Cha, H.; Lee, D.; Yoon, S. Bridging the Nanogap with Light: Continuous Tuning of Plasmon Coupling between Gold Nanoparticles. *ACS Nano* **2015,** *9*, 12292.

37. Cha, H.; Yoon, J. H.; Yoon, S. Probing Quantum Plasmon Coupling Using Gold Nanoparticle Dimers with Tunable Interparticle Distances Down to the Subnanometer Range. *ACS Nano* **2014,** *8,* 8554.
38. Yang, L.; Wang, H.; Yan, B.; Reinhard, B. M. Calibration of Silver Plasmon Rulers in the 1-25 nm Separation Range: Experimental Indications of Distinct Plasmon Coupling Regimes. *J. Phys. Chem. C* **2010,** *114,* 4901.
39. Chen T, Pourmand M, Feizpour A, Cushman B, Reinhard BM. Tailoring Plasmon Coupling in Self-Assembled One-Dimensional Au Nanoparticle Chains through Simultaneous Control of Size and Gap Separation. *J Phys. Chem. Lett.* **2013,** *4,* 13, 2147.
40. Popp, P. S.; Herrmann, J. F.; Fritz, E. C.; Ravoo, B. J.; Hoppener, C. Impact of the Nanoscale Gap Morphology on the Plasmon Coupling in Asymmetric Nanoparticle Dimer Antennas. *Small* **2016,** *12,* 1667.
41. Grillet, N.; Manchon, D.; Bertorelle, F.; Bonnet, C.; Broyer, M.; Cottancin, E.; Lermé, J.; Hillenkamp, M.; Pellarin, M. Plasmon Coupling in Silver Nanocube Dimers: Resonance Splitting Induced by Edge Rounding. *ACS Nano* **2011,** *5,* 9450.
42. Huh, J. H.; Lee, J.; Lee, S. Comparative Study of Plasmonic Resonances between the Roundest and Randomly Faceted Au Nanoparticles-on-Mirror Cavities. *ACS Photonics* **2018,** *5,* 413.
43. Yoon, J. H.; Selbach, F.; Schumacher, L.; Jose, J.; Schlucker, S. Surface Plasmon Coupling in Dimers of Gold Nanoparticles: Experiment and Theory for Ideal (Spherical) and Nonideal (Faceted) Building Blocks. *ACS Photonics* **2019,** *6,* 642.
44. Esteban, R.; Aguirregabiria, G.; Borisov, A. G.; Wang, Y. M.; Nordlander, P.;

Bryant, G. W.; Aizpurua, J. The Morphology of Narrow Gaps Modifies the Plasmonic Response. *ACS Photonics* **2015,** *2,* 295.

45. Hooshmand, N.; Bordley, J. A.; El-Sayed, M. A. The Sensitivity of the Distance Dependent Plasmonic Coupling between Two Nanocubes to Their Orientation: Edge-to-Edge Versus Face-to-Face. *J. Phys. Chem. C* **2016,** *120,* 4564.
46. Tserkezis, C.; Esteban, R.; Sigle, D. O.; Mertens, J.; Herrmann, L. O.; Baumberg, J. J.; Aizpurua, J. Hybridization of Plasmonic Antenna and Cavity Modes: Extreme Optics of Nanoparticle-on-Mirror Nanogaps. *Phys. Rev. A: At., Mol., Opt. Phys.* **2015,** *92,* 053811.
47. Lee, D.; Yoon, S. Effect of Nanogap Curvature on SERS: A Finite-Difference Time-Domain Study. *J. Phys. Chem. C* **2016,** *120,* 20642.
48. Kim, M.; Kwon, H.; Lee, S.; Yoon, S. Effect of Nanogap Morphology on Plasmon Coupling. *ACS Nano* **2019,** *13,* 10, 12100.
49. Jain, P. K.; Eustis, S.; El-Sayed, M. A. Plasmon Coupling in Nanorod Assemblies: Optical Absorption, Discrete Dipole Approximation Simulation, and Exciton-Coupling Model. *J. Phys. Chem. B* **2006,** *110,* 37, 18243.
50. Gluodenis, M.; Foss, C. A. The Effect of Mutual Orientation on the Spectra of Metal Nanoparticle Rod−Rod and Rod−Sphere Pairs. *J. Phys. Chem. B* **2002,** *106,* 37, 9484.
51. Thomas, K. G.; Barazzouk, S.; Ipe, B. I.; Joseph, S. T. S.; Kamat, P. V. Uniaxial Plasmon Coupling through Longitudinal Self-Assembly of Gold Nanorods. *J. Phys. Chem. B* **2004,** *108,* 35, 13066.
52. Rosi, N. L.; Mirkin, C. A. Nanostructures in Biodiagnostics. *Chem. Rev.* **2005,** *105,*

4, 1547.

53. Alivisatos, P. The Use of Nanocrystals in Biological Detection. *Nat Biotechnol* **2004,** *22,* 47.
54. Haes, A. J.; Hall, W. P.; Chang, L.; Klein, W. L.; Van Duyne, R. P. A Localized Surface Plasmon Resonance Biosensor: First Steps toward an Assay for Alzheimer's Disease. *Nano Lett.* **2004,** *4,* 6, 1029.
55. Haes, A. J.; Zou, S.; Schatz, G. C.; Van Duyne, R. P. A Nanoscale Optical Biosensor: The Long Range Distance Dependence of the Localized Surface Plasmon Resonance of Noble Metal Nanoparticles. *J. Phys. Chem. B* **2004,** *108,* 1, 109.
56. McFarland, A. D.; Van Duyne, R. P. Single Silver Nanoparticles as Real-Time Optical Sensors with Zeptomole Sensitivity. *Nano Lett.* **2003,** *3,* 8, 1057.
57. Haes, A. J.; Van Duyne, R. P. A Nanoscale Optical Biosensor: Sensitivity and Selectivity of an Approach Based on the Localized Surface Plasmon Resonance Spectroscopy of Triangular Silver Nanoparticles. *J. Am. Chem. Soc.* **2002,** *124,* 35, 10596.
58. Storhoff, J. J.; Elghanian, R.; Mucic, R. C.; Mirkin, C. A.; Letsinger, R. L. One-Pot Colorimetric Differentiation of Polynucleotides with Single Base Imperfections Using Gold Nanoparticle Probes. *J. Am. Chem. Soc.* **1998,** *120,* 9, 1959.
59. El-Sayed IH, Huang X, El-Sayed MA. Surface Plasmon Resonance Scattering and Absorption of anti-EGFR Antibody Conjugated Gold Nanoparticles in Cancer Diagnostics: Applications in Oral Cancer. Nano Lett. 2005, 5, 5, 829–834.
60. Sokolov K, Follen M, Aaron J, Pavlova I, Malpica A, Lotan R, Richards-Kortum

R. Real-Time Vital Optical Imaging of Precancer Using Anti-Epidermal Growth Factor Receptor Antibodies Conjugated to Gold Nanoparticles. Cancer Res 2003, 63, 9, 1999.

61. Huang X, El-Sayed IH, Qian W, El-Sayed MA. Cancer Cell Imaging and Photothermal Therapy in the Near-Infrared Region by Using Gold Nanorods. J. Am. Chem. Soc. 2006, 128, 6, 2115–2120.
62. Loo C, Lowery A, Halas N, West J, Drezek R. Immunotargeted Nanoshells for Integrated Cancer Imaging and Therapy. *Nano Lett.* 2005, 5, 4, 709–711.
63. Hirsch LR, Stafford RJ, Bankson JA, Sershen SR, Rivera B, Price RE, Hazle JD, Halas NJ, West JL. Nanoshell-mediated near-infrared thermal therapy of tumors under magnetic resonance guidance. Proc Natl Acad Sci USA 2003, 100, 23, 13549.
64. Zharov VP, Kim J-W, Curiel DT, Everts M. Self-Assembling Nanoclusters in Living Systems: Application for Integrated Photothermal Nanodiagnostics and Nanotherapy. Nanomedicine, 2005, 1, 326.
65. El-Sayed, I. H.; Huang, X.; El-Sayed, M. A. Selective Laser Photo-Thermal Therapy of Epithelial Carcinoma Using Anti-EGFR Antibody Conjugated Gold Nanoparticles. *Cancer Lett*, **2005,** *239*, 129.
66. Chen, C. K.; Heinz, T. F.; Ricard, D.; Shen, Y. R. Surface-Enhanced Second-Harmonic Generation and Raman Scattering. *Phys. Rev. B* **1983**, *27*, 1965.
67. Nikoobakht, B.; Wang, J.; El-Sayed, M. A. Surface-Enhanced Raman Scattering of Molecules Adsorbed on Gold Nanorods: off-Surface Plasmon Resonance Condition. *Chem Phys Lett* **2002,** *366*, 17.
68. Hulteen, J. C.; Van Duyne, R. P. Nanosphere Lithography: A Materials General

Fabrication Process for Periodic Particle Array Surfaces. *J. Vac. Sci. Technol. A* **1995,** *13,* 1553.

69. Nie, S.; Emory, S. R. Probing Single Molecules and Single Nanoparticles by Surface-Enhanced Raman Scattering. *Science* **1997,** *275,* 1102.
70. Link, S.; El-Sayed, M. A. Spectral Properties and Relaxation Dynamics of Surface Plasmon Electronic Oscillations in Gold and Silver Nanodots and Nanorods. *J. Phys. Chem. B* **1999,** *103,* 8410.
71. Raeesi, V.; Chou, L. Y. T.; Chan, W. C. W. Tuning the Drug Loading and Release of DNA-Assembled Gold-Nanorod Superstructures. *Adv. Mater.* **2016**, *28*, 8511.
72. Huang, X. H.; Jain, P. K.; El-Sayed, I. H.; El-Sayed, M. A. Gold Nanoparticles: Interesting Optical Properties and Recent Applications in Cancer Diagnostic and Therapy. *Nanomedicine* **2007**, *2,* 681.
73. Fu, Q.; Li, Z.; Fu, F.; Chen, X.; Song, J.; Yang, H. Stimuli-Responsive Plasmonic Assemblies and Their Biomedical Applications, *Nano Today,* **2021,** *36*, 101014.
74. Zhu, R.; Su, L.; Dai, J.; Li, Z.-W.; Bai, S.; Li, Q.; Chen, X.; Song, J.; Yang, H. Biologically Responsive Plasmonic Assemblies for Second Near-Infrared Window Photoacoustic Imaging-Guided Concurrent Chemo-Immunotherapy. *ACS Nano* **2020,** *14,* 4, 3991.
75. Near-Infrared Plasmonic Assemblies of Gold Nanoparticles with Multimodal Function for Targeted Cancer Theragnosis. Kim, S.-E.; Lee, B.-R.; Lee, H.; Jo, S. D.; Kim, H.; Won, Y. Y.; Lee, J. *Scientific Reports* **2017,** *7,* 17327.
76. Cheng, X. J.; Sun, R.; Yin, L.; Chai, Z. F.; Shi, H. B.; Gao, M. Y. Light-Triggered Assembly of Gold Nanoparticles for Photothermal Therapy and Photoacoustic

Imaging of Tumors *in vivo*. *Adv. Mater.* **2017**, *29*, 1604894.

77. Reinhard, B. M.; Siu, M.; Agarwal, H.; Alivisatos, A. P.; Liphardt, J. Calibration of Dynamic Molecular Rulers Based on Plasmon Coupling between Gold Nanoparticles. *Nano Lett.* **2005,** *5*, 2246.
78. Sönnichsen, C.; Reinhard, B.; Liphardt, J. A Molecular Ruler Based on Plasmon Coupling of Single Gold and Silver Nanoparticles. *Nat Biotechnol* **2005,** *23,* 741.
79. Hill, R. T.; Mock, J. J.; Hucknall, A.; Wolter, S. D.; Jokerst, N. M.; Smith, D. R.; Chilkoti, A. Plasmon Ruler with Angstrom Length Resolution. *ACS Nano* **2012,** *6*, 9237.
80. Alegret, J.; Rindzevicius, T.; Pakizeh, T.; Alaverdyan, Y.; Gunnarsson, L.; Kall, M., Plasmonic Properties of Silver Trimers with Trigonal Symmetry Fabricated by Electron-Beam Lithography. *J Phys Chem C* **2008,** *112*, 37, 14313.
81. Aizpurua, J.; Hanarp, P.; Sutherland, D. S.; Käll, M.; Bryant, G. W.; García de Abajo, F. J. Optical Properties of Gold Nanorings. *Phys. Rev. Lett.,* **2003,** *90,* 05740, 1.
82. Aizpurua, J.; Blanco, L.; Hanarp, P.; Sutherland, D. S.; Käll, M.; Bryant, G. W.; García de Abajo, F. J. Light Scattering in Gold Nanorings. *J. Quant. Spectro. Rad. Trans.,* **2004,** *89,* 11.
83. Urban, A. S.; Shen, X.; Wang, Y.; Large, N.; Wang, H.; Knight, M. W.; Nordlander, P.; Chen, H.; Halas. N. J. Three-Dimensional Plasmonic Nanoclusters. *Nano Lett.* **2013,** *13,* 9, 4399.

84. Fan, J. A.; Bao, K.; Wu, C.; Bao, J.; Bardhan, R.; Halas, N. J.; Manoharan, V. N.; Shvets, J.; Nordlander, P.; Capasso, F. Fano-like Interference in Self-Assembled Plasmonic Quadrumer Clusters. *Nano Lett.* **2010,** *10*, 11, 4680.

85. Kuemin, C.; Nowack, L.; Bozano, L.; Spencer, N. D.; Wolf, H. Oriented Assembly of Gold Nanorods on the Single-Particle Level. *Adv Funct. Mater*. **2012,** *22*, 4, 702.

86. Hung, A. M.; Micheel, C. M.; Bozano, L. D.; Osterbur, L. W.; Wallraff, G. M.; Cha, J. N., Large-Area Spatially Ordered Arrays of Gold Nanoparticles Directed by Lithographically Confined DNA Origami. *Nat. Nanotechnol.* **2010,** *5*, 2, 121.

87. Lin, Q. Y.; Mason, J. A.; Li, Z.; Zhou, W.; O'Brien, M. N.; Brown, K. A.; Jones, M. R.; Butun, S.; Lee, B.; Dravid, V. P.; Aydin, K.; Mirkin, C. A. Building Superlattices from Individual Nanoparticles via Template-Confined DNA-Mediated Assembly. *Science* **2018,** *359*, 669.

88. Piner, R. D.; Zhu, J.; Xu, F.; Hong, S. H.; Mirkin, C. A., "Dip-pen" nanolithography. *Science* **1999,** *283*, 5402, 661.

89. Huang, C. J.; Ye, J.; Wang, S.; Stakenborg, T.; Lagae, L. Gold Nanoring as a Sensitive Plasmonic Biosensor for on-Chip DNA Detection. *Appl Phys Lett.* **2012,** *100*, 173114.

90. Flauraud, V.; Mastrangeli, M.; Bernasconi, G. D.; Butet, J.; Alexander, D. T. L.; Shahrabi, E.; Martin, O. J. F.; Brugger, J., Nanoscale topographical control of capillary assembly of nanoparticles. *Nat. Nanotechnol.* **2017,** *12*, 1, 73.

91. Manfrinato, V. R.; Wen , J.; Zhang, L.; Yang, Y.; Hobbs, R. G.; Baker, B.; Su, D.; Zakharov, D.; Zaluzec, N. J.; Miller, D. J.; Stach E. A.; Berggren, K. K.

Determining the Resolution Limits of Electron-Beam Lithography: Direct Measurement of the Point-Spread Function. *Nano Lett.* **2014,** *14*, 4406.

92. Bratton, D.; Yang, D.; Dai, J.; Ober, C. K. Recent Progress in High Resolution Lithography. *Polym. Adv. Technol.* **2006,** *17*, 94.
93. Fan, J. A.; Wu, C.; Bao, K.; Bao, J.; Bardhan, R.; Halas, N. J.; Manoharan, V. N.; Nordlander, P.; Shvets, G.; Capasso, F. Self-Assembled Plasmonic Nanoparticle Clusters. *Science* **2010,** *328*, 5982, 1135.
94. Hu, J. M.; Wu, T.; Zhang, G. Y.; Liu, S. Y., Efficient Synthesis of Single Gold Nanoparticle Hybrid Amphiphilic Triblock Copolymers and Their Controlled Self-Assembly. *J. Am. Chem. Soc.* **2012,** *134*, 18, 7624.
95. Nie, Z.; Fava, D.; Kumacheva, E.; Zou, S.; Walker, G. C.; Rubinstein, M., Self-assembly of metal–polymer analogues of amphiphilic triblock copolymers. *Nat. Mater*. **2007,** *6*, 8, 609.
96. Yi, C.; Liu, H.; Zhang, S.; Yang, Y.; Zhang, Y.; Lu, Z.; Kumacheva, E.; Nie, Z. Self-Limiting Directional Nanoparticle Bonding Governed by Reaction Stoichiometry. *Science* **2020,** *369*, 6509, 1369.
97. Pieranski, P. Two-Dimensional Interfacial Colloidal Crystals. *Phys. Rev. Lett.* **1980,** *45*, 7, 569.
98. Rizzo, A.; Nobile, C.; Mazzeo, M.; Giorgi, M. D.; Fiore, A.; Carbone, L.; Cingolani, R.; Manna, L.; Gigli, G., Polarized Light Emitting Diode by Long-Range Nanorod Self-Assembling on a Water surface. *Acs Nano* **2009,** *3*, 6, 1506.
99. Hamon, C.; Postic, M.; Mazari, E.; Bizien, T.; Dupuis, C.; Even-Hernandez, P.; Jimenez, A.; Courbin, L.; Gosse, C.; Artzner, F.; Marchi-Artzner, V. Three-

Dimensional Self-Assembling of Gold Nanorods with Controlled Macroscopic Shape and Local Smectic B Order. *Acs Nano* **2012,** *6*, 5, 4137.

100. Correa-Duarte, M. A.; Perez-Juste, J.; Sanchez-Iglesias, A.; Giersig, M.; Liz-Marzan, L. M., Aligning an Nanorods by Using Carbon Nanotubes as Templates. *Angew. Chem. Int. Ed*. **2005,** *44*, 28, 4375.

101. Hermanson, K. D.; Lumsdon, S. O.; Williams, J. P.; Kaler, E. W.; Velev, O. D. Dielectrophoretic Assembly of Electrically Functional Microwires from Nanoparticle Suspensions. *Science* **2001,** *294*, 5544, 1082.

102. Wang, Y.; DePrince III, A. E.; K. Gray, S.; Lin, X.-M.; Pelton, M. Solvent-Mediated End-to-End Assembly of Gold Nanorods. *J. Phys. Chem. Lett.* **2010,** *1*, 18, 2692.

103. Wessels, J. M.; Nothofer, H. G.; Ford, W. E.; von Wrochem, F.; Scholz, F.; Vossmeyer, T.; Schroedter, A.; Weller, H.; Yasuda, A. Optical and Electrical Properties of Three-Dimensional Interlinked Gold Nanoparticle Assemblies. *J. Am. Chem. Soc.* **2004,** *126*, 10, 3349.

104. Novak, J. P.; Feldheim, D. L. Assembly of Phenylacetylene-Bridged Silver and Gold Nanoparticle Arrays. *J. Am. Chem. Soc.* **2000,** *122,* 16, 3979.

105. Macfarlane, R. J.; Lee, B.; Jones, M. R.; Harris, N.; Schatz, G. C.; Mirkin, C. A. Nanoparticle superlattice engineering with DNA. *Science* **2011,** *334*, 6053, 204.

106. Zhang, Y.; Lu, F.; Yager, K. G.; van der Lelie, D.; Gang, O. A General Strategy for the DNA-Mediated Self-Assembly of Functional Nanoparticles into Heterogeneous Systems. *Nat. Nanotechnol.* **2013,** *8*, 11, 865.

107. Li, Z.; Zhu, Z.; Liu, W.; Zhou, Y.; Han, B.; Gao, Y.; Tang, Z. Reversible Plasmonic Circular Dichroism of Au Nanorod and DNA Assemblies. *J. Am. Chem. Soc.* **2012,** *134*, 7, 3322.

108. Zhuang, J. M.; Gordon, M. R.; Ventura, J.; Li, L. Y.; Thayumanavan, S. Multi-Stimuli Responsive Macromolecules and Their Assemblies. *Chem. Soc. Rev.* **2013,** *42*, 17, 7421.

109. She, W. C.; Luo, K.; Zhang, C. Y.; Wang, G.; Geng, Y. Y.; Li, L.; He, B.; Gu, Z. W. The Potential of Self-Assembled, pH-Responsive Nanoparticles of mPEGylated Peptide Dendron-Doxorubicin Conjugates for Cancer Therapy. *Biomaterials* **2013,** *34*, 5, 1613.

110. Marson, R. L.; Nguyen, T. D.; Glotzer, S. C. Rational Design of Nanomaterials from Assembly and Reconfigurability of Polymer-Tethered Nanoparticles. *MRS Comm.* **2015,** *5*, 03, 397.

111. Horsch, M. A.; Zhang, Z.; Glotzer, S. C. Self-Assembly of End-Tethered Nanorods in a Neat System and Role of Block Fractions and Aspect Ratio. *Soft Matter* **2010,** *6*, 5, 945.

112. Liu, K.; Zhao, N.; Kumacheva, E., Self-Assembly of Inorganic Nanorods. *Chem. Soc. Rev.* **2011,** *40*, 2, 656.

113. Iacovella, C. R.; Horsch, M. A.; Glotzer, S. C. Local Ordering of Polymer-Tethered Nanospheres and Nanorods and the Stabilization of the Double Gyroid Phase. *J. Chem. Phys.* **2008,** *129*, 4, 044902

114. Tung, C.; Cacciuto, A. Phase Separation of Mixed Polymer Brushes on Surfaces with Nonuniform Curvature. *J. Chem. Phys.* **2013,** *139*, 194902.

115. Choueiri, R. M.; Galati, E.; Theŕien-Aubin, H.; Klinkova, A.; Larin, E. M.; Querejeta-Fernańdez,A.; Han, L.; Xin, H. L.; Gang, O.; Zhulina, E. B.; Rubinstein, M.; Kumacheva, E. Surface Patterning of Nanoparticles with Polymer Patches., *Nature*, **2016,** *538*, 79.

116. Galati, E.; Tebbe, M.; Querejeta-Fernańdez, A.; Xin, H. L.; Gang, O.; Zhulina, E. B.; Kumacheva, E. Shape-Specific Patterning of Polymer-Functionalized Nanoparticles. *ACS Nano* **2017,** *11*, 4995.

117. Chen, T.; Yang, M.; Wang, X.; Tan, L. H.; Chen, H. Controlled Assembly of Eccentrically Encapsulated Gold Nanoparticles. *J. Am. Chem. Soc.* **2008,** *130*, 11858.

118. Chen, G.; Gibson, K. J.; Liu, D.; Rees, H. C.; Lee, J. H.; Xia, W.; Lin, R. Q.; Xin, H. L.; Gang, O.; Weizmann, Y. Regioselective Surface Encoding of Nanoparticles for Programmable Self-Assembly. *Nat. Mater.* **2019,** *18*, 169.

119. Pieranski, P. Two-Dimensional Interfacial Colloidal Crystals. *Phys. Rev. Lett.* **1980,** *45*, 7, 569.

120. Srivastava, S.; Nykypanchuk, D.; Fukuto, M.; Halverson, J. D.; Tkachenko, A. V.; Yager, K. G.; Gang, O. Two-Dimensional DNA-Programmable Assembly of Nanoparticles at Liquid Interfaces. *J. Am. Chem. Soc.* **2014,** *136*, 8323.

121. Cui, M.; Emrick, T.; Russell, T. P. Stabilizing Liquid Drops in Nonequilibrium Shapes by the Interfacial Jamming of Nanoparticles. *Science*, **2013,** *342*, 460.

122. Lin, Y.; Skaff, H.; Emrick, T.; Dinsmore, A. D.; Russell, T. P. Nanoparticle Assembly and Transport at Liquid-Liquid Interfaces. *Science* **2003,** *299*, 5604, 226.

123. Ye, X. C.; Zhu, C. H.; Ercius, P.; Raja, S. N.; He, B.; Jones, M. R.; Hauwiller,

M. R.; Liu, Y.; Xu, T.; Alivisatos, A. P. Structural Diversity in Binary Superlattices Self-Assembled from Polymer-Grafted Nanocrystals. *Nat. Comm.* **2015,** *6, 74.*

124. He, J.; Kanjanaboos, P.; Frazer, N. L.; Weis, A.; Lin, X.-M.; Jaeger, H. M. Fabrication and Mechanical Properties of Large-Scale Freestanding Nanoparticle Membranes. *Small* **2010,** *6,* 1449.

125. He, J. B.; Lin, X. M.; Chan, H.; Vukovic, L.; Kral, P.; Jaeger, H. M. Diffusion and Filtration Properties of Self-Assembled Gold Nanocrystal Membranes. *Nano Lett.* **2011,** *11,* 2430.

126. Ming, T.; Kou, X.; Chen, H.; Wang, T.; Tam, H. L.; Cheah, K. W.; Chen, J. Y.; Wang, J. Ordered Gold Nanostructure Assemblies Formed by Droplet Evaporation. *Angew. Chem.* **2008,** *120*, 50, 9831.

127. Christopher, P.; Xin, H.; Linic, S. Visible-Light-Enhanced Catalytic Oxidation Reactions on Plasmonic Silver Nanostructures. *Nat. Chem.* **2011,** *3,* 467.

128. Pyayt, A. L.; Wiley, B.; Xia, Y.; Chen, A.; Dalton, L. Integration of Photonic and Silver Nanowire Plasmonic Waveguides. *Nat. Nanotechnol*. **2008,** *3,* 660.

129. Chen, S.; Yang, Y. Magnetoelectrochemistry of Gold Nanoparticle Quantized Capacitance Charging. *J. Am. Chem. Soc.* **2002,** *124,* 5280.

130. Shahjamali, M. M.; Bosman, M.; Cao, S.; Huang, X.; Cao, X.; Zhang, H.; Pramana, S. S.; Xue, C. Surfactant-Free Sub-2 nm Ultrathin Triangular Gold Nanoframes. *Small* **2013,** *9,* 2880.

131. Hu, Y.; Chou, T.; Wang, H.; Du, H. Monodisperse Colloidal Gold Nanorings: Synthesis and Utility for Surface-Enhanced Raman Scattering. *J. Phys. Chem. C* **2014,** *118,* 16011.

132. Jang, H. J.; Ham, S.; Acapulco, J. A. I.; Song, Y.; Hong, S.; Shuford, K. L.; Park, S. H. Fabrication of 2D Au Nanorings with Pt Framework. *J. Am. Chem. Soc.* **2014,** *136,* 17674.

133. Michota, A.; Bukowska, J. Surface-Enhanced Raman Scattering (SERS) of 4-Mercaptobenzoic Acid on Silver and Gold Substrates. *J. Raman Spectrosc.* **2003,** *34,* 21.

134. Hsieh, C. W.; Lin, P. Y.; Hsieh, S. C. Improved Surface-Enhanced Raman Scattering of Insulin Fibril Templated Colloidal Gold Nanoparticles on Silicon. *J. Nanophoton* **2012,** *6,* 1, 063501.

135. Liu, Y.; Zhou, J.; Yuan, X.; Jiang, T.; Petti, L.; Zhou, L.; Mormile, P. Hydrothermal Synthesis of Gold Polyhedral Nanocrystals by Varying Surfactant Concentration and Their LSPR and SERS Properties. *RSC Adv.*, **2015,** *5,* 68668.

136. Le Ru, E.; Blackie, E.; Meyer, M.; Etchegoin, P. G. Surface Enhanced Raman Scattering Enhancement Factors: A Comprehensive Study. *J. Phys. Chem. C,* **2007,** *111,* 13794.

137. Millstone, J. E.; Georganopoulou, D. G.; Xu, X.; Wei, W.; Li, S.; Mirkin, C. A. DNA-Gold Triangular Nanoprism Conjugates. *Small* **2008,** *4,* 2176.

138. Pastoriza-Santos, I.; Alvarez-Puebla, R. A.; Liz- -Marzan, L. M. Synthetic Routes and Plasmonic Properties of Noble Metal Nanoplates Classes of

Nanomagnets Created from Alkanethiol-Coated Pt or Pd Nanoparticles and Their Alloys with Co One- and Two-Dimensional Inorganic Crystals inside Inorganic Nanotubes Covalent Attachment of Aromatic Diisocyanate to the Sidewalls of Single- and Double-Walled Carbon Nanotubes. *Eur. J. Inorg. Chem.* **2010,** 4288.

139. Pastoriza-Santos, I.; Liz-Marzan, L. M. Colloidal Silver Nanoplates. State of the Art and Future Challenges. *J. Mater. Chem.* **2008,** *18,* 1724.

140. Tao, A. R.; Habas, S.; Yang, P. Shape Control of Colloidal Metal Nanocrystals. *Small* **2008,** *4,* 310.

141. Rycenga, M.; Cobley, C. M.; Zeng, J.; Li, W.; Moran, C. H.; Zhang, Q.; Qin, D.; Xia, Y. Controlling the Synthesis and Assembly of Silver Nanostructures for Plasmonic Applications. *Chem Rev.* **2011,** *111,* 3669.

142. Shahjamali, M. M.; Bosman, M.; Cao, S.; Huang, X.; Saadat, S.; Martinsson, E.; Aili, D.; Tay, Y. Y.; Liedberg, B.; Loo, S. C. J.; Zhang, H.; Boey, F.; Xue, C. Gold Coating of Silver Nanoprisms. *Adv. Funct. Mater.* **2012,** *22,* 849.

143. Liu, H.; Liu, T.; Zhang, L.; Han, L.; Gao, C.; Yin, Y. Etching-Free Epitaxial Growth of Gold on Silver Nanostructures for High Chemical Stability and Plasmonic Activity. *Adv. Funct. Mater.* **2015,** *25,* 5435.

144. Liu, X.; Li, L.; Yang, Y.; Yin, Y.; Gao, C. One-Step Growth of Triangular Silver Nanoplates with Predictable Sizes on a Large Scale. *Nanoscale,* **2014,** *6,* 4513.

145. Zhang, Q.; Li, N.; Goebl, J.; Lu, Z.; Yin, Y. A Systematic Study of the Synthesis of Silver Nanoplates: Is Citrate a "Magic" Reagent? *J. Am. Chem. Soc.* **2011,** *133,* 18931.

146. Zhang, Q.; Hu, Y.; Guo, S.; Goebl, J.; Yin, Y. Seeded Growth of Uniform Ag Nanoplates with High Aspect Ratio and Widely Tunable Surface Plasmon Bands. *Nano Lett.* **2010,** *10,* 5037.

147. Metraux, G. S.; Mirkin, C. A.; Rapid Thermal Synthesis of Silver Nanoprisms with Chemically Tailorable Thickness. *Adv. Mater.* **2005,** *17,* 412.

148. Zou, X.; Ying, E.; Dong S. Preparation of Novel Silver-Gold Bimetallic Nanostructures by Seeding with Silver Nanoplates and Application in Surface-Enhanced Raman Scattering. *J. Coll. Interf. Sci.* **2007,** *306,* 2, 307.

149. Xiong, Y.; Xia, Y. Shape-Controlled Synthesis of Metal Nanostructures: The Case of Palladium. *Adv. Mater*. **2007,** *19,* 3385.

150. Smith, A. M.; Mancini, M. C.; Nie, S. Second Window for in vivo Imaging. *Nat Nanotechnol.* **2009,** *4,* 710.

151. Chen, T.; Du, C. L.; Tan, L. H.; Shen, Z. X.; Chen, H. Site-Selective Localization of Analytes on Gold Nanorod Surface for Investigating Field Enhancement Distribution in Surface-Enhanced Raman Scattering. *Nanoscale*, **2011,** *3,* 1575.

152. He, J.; Zhang, P.; Gong, J.; Nie, Z. Facile Synthesis of Functional Au Nanopatches and Nanocups. *Chem. Comm*. **2012,** *48,* 7344.

153. Nie, Z.; Petukhova, A.; Kumacheva, E. Properties and Emerging Applications of Self-Assembled Structures Made from Inorganic Nanoparticles. *Nat. Nanotechnol.* **2010,** *5,* 15.

154. Halas, N. J.; Lal, S.; Chang, W.-S.; Link, S.; Nordlander, P. Plasmons in Strongly Coupled Metallic Nanostructures. *Chem. Rev.* **2011,** *111,* 3913.

155. Nam, J. M.; Liz-Marzán, L.; Halas, N. Chemical Nanoplasmonics: Emerging Interdisciplinary Research Field at Crossroads between Nanoscale Chemistry and Plasmonics. *Acc. Chem. Res*. **2019**, *52*, 2995.

156. Yankovich, A. B.; Munkhbat, B.; Baranov, D. G.; Cuadra, J.; Olsén, E.; Lourenço-Martins, H.; Tizei, L. H. G.; Kociak, M.; Olsson, E.; Shegai, T. Visualizing Spatial Variations of Plasmon-Exciton Polaritons at the Nanoscale Using Electron Microscopy. *Nano Lett.* **2019** *19*, 8171.

157. Jiang, N.; Zhuo, X.; Wang, J. Active Plasmonics: Principles, Structures, and Applications. *Chem. Rev.* **2018,** *118,* 3054.

158. Wu, X.; Hao, C.; Kumar, J.; Kuang, H.; Kotov, N. A.; Liz-Marzán, L. M.; Xu, C. Plasmonic Nanoassemblies with Environment Responsiveness for Biosensing. *Chem. Soc. Rev. **2018,** 47, 4677.*

159. Christopher, P.; Xin, H.; Linic, S. Visible-Light-Enhanced Catalytic Oxidation Reactions on Plasmonic Silver Nanostructures. *Nat. Chem.* **2011,** *3,* 467.

160. Smith, J. G.; Faucheaux, J. A.; Jain, P. K. Plasmon Resonances for Solar Energy Harvesting: A Mechanistic Outlook. *Nano Today* **2015,** *10,* 67.

161. Langer, J. Langer, J.; Jimenez de Aberasturi, D.; Aizpurua, J.; Alvarez-Puebla, R. A.; Auguie, B.; Baumberg, J. J.; Bazan, G. C.; Bell, S. E. J.; Boisen, A.; Brolo,

A. G.; Choo, J.; Cialla-May, D.; Deckert, V.; Fabris, L.; Faulds, K.; García de Abajo, F. J.; Goodacre, R.; Graham, D.; Haes, A. J.; Haynes, C. L.; Huck, C.; Itoh, T.; Kall, M.; Kneipp, J.; Kotov, N. A.; Kuang, H.; Le Ru, E. C.; Lee, H. K.; Li, J.-F.; Ling, X. Y.; Maier, S. A.; Mayerhöfer, T.; Moskovits, M.; Murakoshi, K.; Nam, J.-M.; Nie, S.; Ozaki, Y.; Pastoriza-Santos, I.; Perez-Juste, J.; Popp, J.; Pucci, A.; Reich, S.; Ren, B.; Schatz, G. C.; Shegai, T.; Schlücker, S.; Tay, L.-L.; Thomas, K. G.; Tian, Z.-Q.; Van Duyne, R. P.; Vo-Dinh, T.; Wang, Y.; Willets, K. A.; Xu, C.; Xu, H.; Xu, Y.; Yamamoto, Y. S.; Zhao, B.; Liz-Marzan, L. M. Present and Future of Surface-Enhanced Raman Scattering. *ACS Nano* **2020,** *14,* 28.

162. Sheikholeslami, S.; Jun, Y.-W.; Jain, P. K.; Alivisatos, A. P. Coupling of Optical Resonances in a Compositionally Asymmetric Plasmonic Nanoparticle Dimer. *Nano Lett.* **2010,** *10,* 2655.

163. Chow, T. H.; Lai, Y. H.; Cui, X. M.; Lu, W. Z.; Zhuo, X. L.; Wang, J. F. Colloidal Gold Nanorings and Their Plasmon Coupling with Gold Nanospheres. *Small* **2019,** *15,* 1902608.

164. Grzelczak, M.; Liz-Marzán, L. M.; Klajn, R. Stimuli-Responsive Self-Assembly of Nanoparticles. *Chem. Soc. Rev.* **2019,** *48,* 1342.

165. Ye, W.; Krüger, K.; Sánchez-Iglesias, A.; García, I.; Jia, X.; Celiksoy, S.; Foerster, B.; Sutter, J.; Bonn, M.; Liz-Marzán, L. M.; Ahijado-Guzmán, R.; Sönnichsen, C. CTAB Stabilizes Silver on Gold Nanorods. *Chem. Mater.* **2020,** *32*, 1650.

166. Du, J.; O'Reilly, R. K. Anisotropic Particles with Patchy, Multicompartment and Janus Architectures: Preparation and Application. *Chem. Soc. Rev.* **2011,** *40*, 2402.

167. Lunn, D. J.; Finnegan, J. R.; Manners, I. Self-Assembly of "Patchy" Nanoparticles: A Versatile Approach to Functional Hierarchical Materials. *Chem. Sci.* **2015,** *6*, 3663.

168. Wang, Y.; Wang, Y.; Breed, D. R.; Manoharan, V. N.; Feng, L.; Hollingsworth, A. D.; Weck, M.; Pine, D. J. Colloids with Valence and Specific Directional Bonding. *Nature* **2012,** *491*, 51.

169. Xu, X.; Rosi, N. L.; Wang, Y.; Huo, F.; Mirkin, C. A. Asymmetric Functionalization of Gold Nanoparticles with Oligonucleotides. *J. Am. Chem. Soc.* **2006,** *128*, 29, 9286.

170. Shen, C.; Lan. X.; Lu, X.; Meyer, T. A.; Ni, W.; Ke, Y.; Wang, Q. Site-Specific Surface Functionalization of Gold Nanorods Using DNA Origami Clamps. *J. Am. Chem. Soc.* **2016,** *138*, 1764.

171. Lu, F.; Yager, K. G.; Zhang, Y.; Xin, H.; Gang, O. Superlattices Assembled through Shape-Induced Directional Binding. *Nat. Comm*. **2015,** *6*, 6912.

172. Sánchez-Iglesias, A.; Claes, N.; Solís, D. M.; Taboada, J. M.; Bals, S.; Liz-Marzán, L. M.; Grzelczak, M. Reversible Clustering of Gold Nanoparticles under Confinement. *Angew. Chem. Int. Ed.* **2018,** *57*, 3183.

173. Grzelczak, M.; Sańchez-Iglesias, A.; Mezerji, H. H.; Bals, A.; Peŕez-Juste, J.; Liz-Marzań, L. M. Steric Hindrance Induces crosslike Self-Assembly of Gold Nanodumbbells. *Nano Lett.* **2012,** *12*, 4380.

174. He, J.; Liu, Y.; Babu, T.; Wei, Z.; Nie, Z. Self-Assembly of Inorganic Nanoparticle Vesicles and Tubules Driven by Tethered Linear Block Copolymers. *J. Am. Chem. Soc.* **2012,** *134,* 11342.

175. Johnson, P. B.; Christy, R. W. Optical Constants of the Noble Metals. *Phys. Rev. B* **1972,** *6,* 4370.

176. Palik, E. Handbook of Optical Constants of Solids. *Academic Press*, **1998**, ISBN 9780125444224.

177. Rubinstein, M.; Colby, R. Polymer Physics. *Oxford University Press*, **2003**, ISBN 9780198520597.

178. Dukes, D.; Li, Y.; Lewis, S.; Benicewicz, B.; Schadler, L.; Kumar, S. K. Conformational Transitions of Spherical Polymer Brushes: Synthesis, Characterization, and Theory. *Macromolecules* **2010,** *43,* 3, 1564.

179. Ohno, K.; Morinaga, T.; Takeno, S.; Tsujii, Y.; Fukuda, T. Suspensions of Silica Particles Grafted with Concentrated Polymer Brush: Effects of Graft Chain Length on Brush Layer Thickness and Colloidal Crystallization. *Macromolecules* **2007,** *40*, 25, 9143.

180. Lin, X.; Liu, Y.; Lin, M.; Zhang, Q.; Nie, Z. Synthesis of Circular and Triangular Gold Nanorings with Tunable Optical Properties. *Chem Comm.* **2017,** *53,* 78, 10765.

181. Yi, C.; Yang, Y.; Nie, Z. Alternating Copolymerization of Inorganic Nanoparticles. *J. Am. Chem. Soc.* **2019,** *141,* 19, 7917.

182. Yang, K.; Liu, Y.; Liu, Y.; Zhang, Q.; Kong, C.; Yi, C.; Zhou, Z.; Wang, Z.; Zhang, G.; Zhang, Y.; Khachab, N. M.; Chen, X.; Nie, Z. Cooperative Assembly of

Magneto-Nanovesicles with Tunable Wall Thickness and Permeability for MRI-Guided Drug Delivery, *J. Am. Chem. Soc.* **2018,** *140,* 13, 4666.

183. Zhulina, E. B.; Birshtein, T. M.; Borisov, O. V. Curved Polymer and Polyelectrolyte Brushes beyond the Daoud-Cotton Model. *Eur. Phys. J. E* **2006,** *20*, 243.

184. Daoud, M.; Cotton J.P. Star Shaped Polymers: A Model for the Conformation and Its Concentration Dependence. *J. Physique* **1982,** *43*, 3, 531.

185. Willets, K. A.; Van Duyne, R. P. Localized Surface Plasmon Resonance Spectroscopy and Sensing. Annu. *Rev. Phys. Chem.* **2007,** *58*, 267.

186. Schuller, J. A.; Barnard, E. S.; Cai, W.; Jun, Y. C.; White, J. S.; Brongersma, M. L. Plasmonics for Extreme Light Concentration and Manipulation. *Nat. Mater.* **2010,** *9*, 193.

187. Giannini, V.; Fernández-Domínguez, A. I.; Heck, S. C.; Maier, S. A. Plasmonic Nanoantennas: Fundamentals and Their Use in Controlling the Radiative Properties of Nanoemitters. *Chem. Rev.* **2011,** *111*, 3888.

188. Kuzyk, A.; Schreiber R.; Fan, Z.; Pardatscher, G.; Roller, E. M.; Hogele, A.; Simmel, F. C.; Govorov, A. O.; Liedl, T. DNA-Based Self-Assembly of Chiral Plasmonic Nanostructures with Tailored Optical Response. *Nature* **2012**, *483,* 311.

189. Nykypanchuk, D.; Maye, M. M.; van der Lelie, D.; Gang, O. DNA-Guided Crystallization of Colloidal Nanoparticles. *Nature* **2008**, *451,* 549.

190. Xiong, H. M.; van der Lelie, D.; Gang, O. Phase Behavior of Nanoparticles Assembled by DNA Linkers. *Phys. Rev. Lett.*, **2009**, *102*, 1, 015504.

191. Shevchenko, E. V.; Talapin, D. V.; Kotov, N. A.; O'Brien, S.; Murray, C. B.

Structural Diversity in Binary Nanoparticle Superlattices. *Nature* **2006,** 439, 55.

192. Chen, Q.; Whitmer, J. K.; Jiang, S.; Bae, S. C.; Luijten, E.; Granick, S. Supracolloidal Reaction Kinetics of Janus Spheres. *Science* **2011,** *331*, 199.

193. Chen, Q.; Bae, S. C.; Granick, S. Directed Self-Assembly of a Colloidal Kagome Lattice. *Nature* **2011,** *469*, 381.

194. Hu, H.; Ji, F.; Xu, Y.; Yu, J.; Liu, Q.; Chen, L.; Chen, Q.; Wen, P.; Lifshitz, Y.; Wang, Y.; Zhang, Q.; Lee, S.T. Reversible and Precise Self-Assembly of Janus Metal-Organosilica Nanoparticles through a Linker-Free Approach. *ACS Nano* **2016,** *10*, 7323.